POLITECNICO
MILANO 1863

SCUOLA DI INGEGNERIA INDUSTRIALE
E DELL'INFORMAZIONE

Pipe-in-pipe solutions for hydrogen transport employing fibre-reinforced polymers: material assessment and application evaluation

TESI DI LAUREA MAGISTRALE IN
MATERIALS ENGINEERING AND NANOTECHNOLOGY
INGEGNERIA DEI MATERIALI E DELLE NANOTECNOLOGIE

Author: **Pietro Vianello**

Student ID: 990063
Advisor: Giulio Guandalini
Co-advisors: Paolo Colbertaldo
Niels Grigat
Federico Parolin
Academic Year: 2022-23

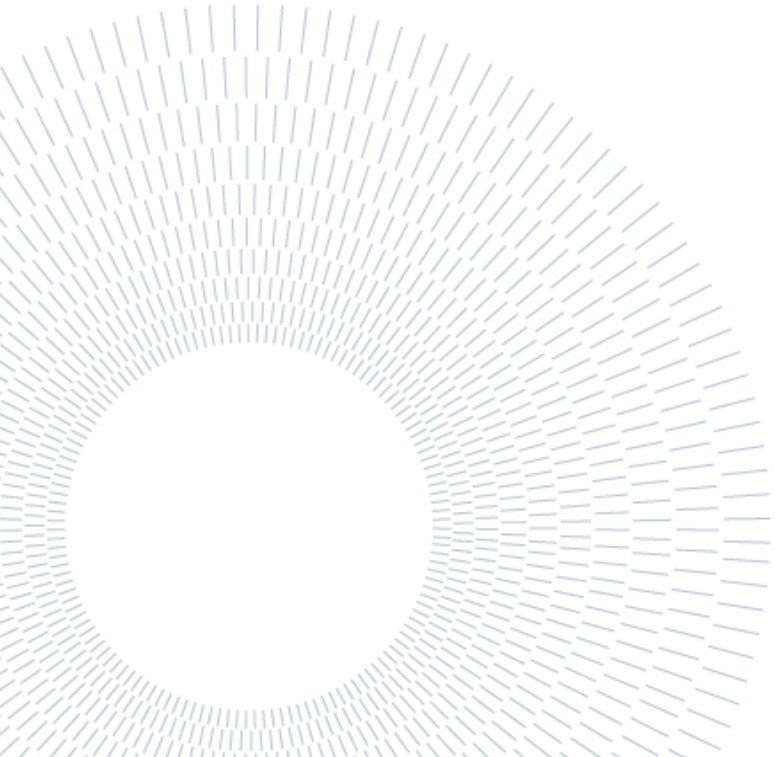

Abstract

To tackle climate change and the need for greater energy security, hydrogen is expected to play a key role in the decades to come, and the possibility of harnessing the existing natural gas grid for hydrogen transport can provide a boost to the development of a more robust hydrogen economy. This work aims to investigate the pipe-in-pipe system as an alternative to the blending of hydrogen and natural gas, to which numerous studies and projects are dedicated, specifically at the transmission level, which is most critical due to mechanical stresses and hydrogen embrittlement of metal pipes. It allows hydrogen to be transported in a pipe inserted inside a natural gas duct, while continuing to supply gas in the annulus, which is expected to remain relevant in the transition towards net-zero CO_2 emissions. A fluid-dynamic study is performed, developing a steady state, 1D, finite-volume model, exploited to determine the optimal diameter of the internal pipe, identified as the one that yields equal gas pressures on both sides of the wall, minimizing the mechanical demand. The analysis considers the use of fibre-reinforced polymer composites, specifically glass or carbon fibre-reinforced epoxy resin and glass fibre-reinforced polypropylene, which are experimentally evaluated in terms of roughness and hydrogen permeability at RWTH Aachen University, in Germany.

The results show that the quality of natural gas in the annulus is not affected by H_2 contamination, of the order of ppm, and that the difference between the roughness values of the three materials does not have a significant impact on fluid dynamics, values which are in any case approximately 0.5-1 μm and thus two orders of magnitude lower than those of steel pipes. The pipe-in-pipe system also requires about five times the number of recompression stations than those for transporting the blend, at equal flow rates, with a consequent increase in CAPEX, in contrast to OPEX, which is not greatly affected by the comparison between blend and pipe-in-pipe. Indeed, although the compression power for the latter is 10-20% higher, in both cases this consumption is marginal compared to the energy flow rate.

Key-words: hydrogen, pipe-in-pipe, fibre-reinforced polymers, transmission grid

Abstract in italiano

Per far fronte al cambiamento climatico e alla necessità di una maggiore sicurezza energetica, si prevede che l'idrogeno giocherà un ruolo chiave nei decenni a venire e la possibilità di sfruttare la rete esistente del gas naturale per trasportare idrogeno può fornire una spinta allo sviluppo di una economia dell'idrogeno più solida. Questo lavoro si propone di investigare il sistema pipe-in-pipe come alternativa al blending di idrogeno e gas naturale, cui numerosi studi e progetti sono dedicati, in particolare a livello della rete di trasporto, maggiormente critica per stress meccanici e infragilimento da idrogeno delle tubazioni metalliche. Esso consente il trasporto di idrogeno in una tubazione inserita all'interno di un condotto del gas naturale, continuando a fornire gas nella sezione anulare, che ci si aspetta rimanere rilevante nella transizione verso le zero emissioni nette di CO_2. Viene svolto uno studio fluidodinamico, sviluppando un modello stazionario, 1D, a volumi finiti, impiegato per determinare il diametro ottimale del tubo interno, identificato come quello che determina uguali pressioni dei gas sui due lati della parete, minimizzando le sollecitazioni meccaniche. L'analisi considera l'utilizzo di materiali compositi polimerici rinforzati con fibre, in particolare resina epossidica rinforzata con fibre di vetro o carbonio e polipropilene rinforzato con fibra di vetro, che sono caratterizzati sperimentalmente in termini di rugosità e permeabilità a idrogeno presso la RWTH Aachen University, in Germania.

I risultati mostrano che la qualità del gas naturale nella sezione anulare non è influenzata dalla contaminazione di H_2, dell'ordine dei ppm, e la differenza tra le rugosità dei tre materiali non incide significativamente sulla fluidodinamica, valori che sono comunque nell'intorno di 0,5-1 μm e quindi due ordini di grandezza inferiori a quelli dei tubi in acciaio. Inoltre le stazioni di compressione richieste dal sistema pipe-in-pipe sono circa cinque volte quelle richieste per il trasporto del blend a parità di portata, con un conseguente aumento di CAPEX, al contrario dell'OPEX, che non subisce grandi variazioni tra blend e sistema pipe-in-pipe. Infatti, nonostante la potenza di compressione per quest'ultimo sia più alta del 10-20%, in entrambi i casi essa è marginale rispetto all'energia trasportata.

Parole chiave: idrogeno, pipe-in-pipe, polimeri rinforzati con fibre, rete di trasporto

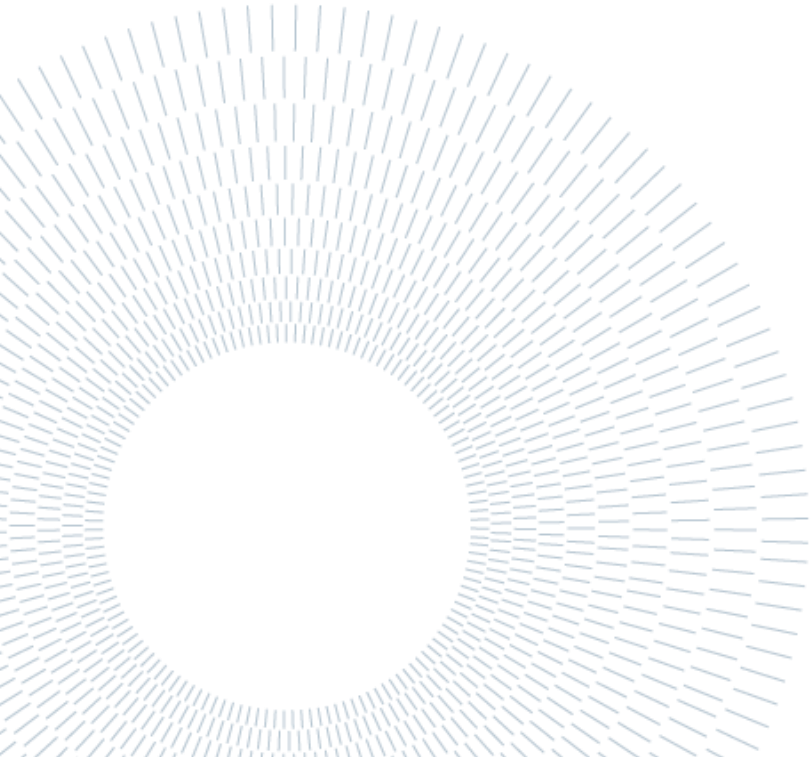

Contents

1 Introduction

The transition to an energy market consisting of an increasing share of sustainable solutions is one of the greatest challenges of our time.

At the heart of the research and development of alternatives to fossil fuels are climate change and the recent energy crisis. The latter is a particularly hot topic in the last year since, after the invasion of Ukraine by Russia in February 2022, natural gas and, consequently, electricity prices, which had already risen following the end of the COVID-19 lockdowns, skyrocketed to record levels, especially in Europe. These dynamics have made clear the need to make changes to the now disrupted geopolitical balances and to seek greater energy security.

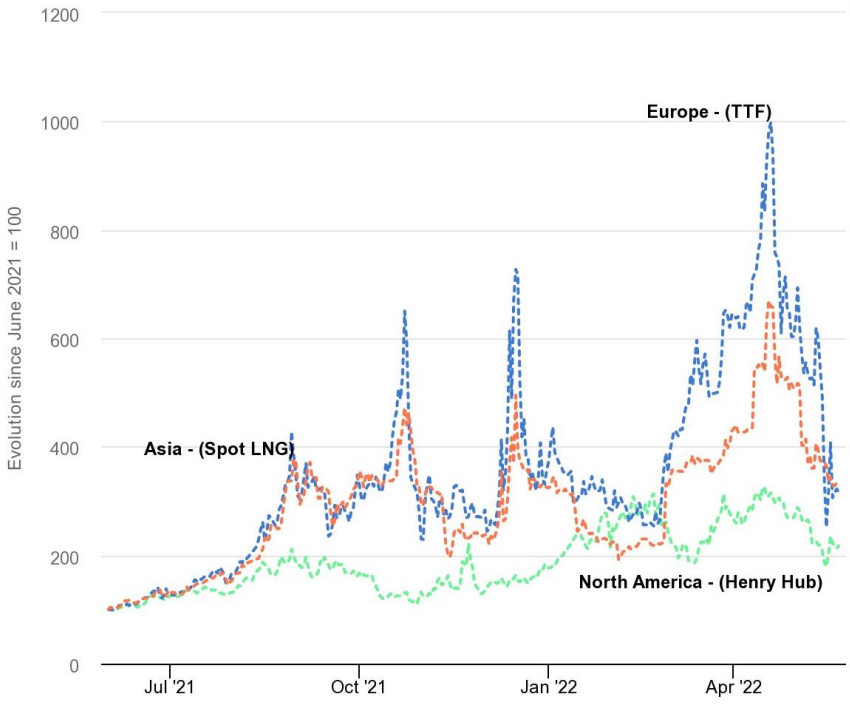

Figure 1.1 - Trend of key regional natural gas prices (2021) [1]

All this has only fuelled the race for renewable energy and the achievement of net-zero CO_2 emissions.

The EU is committed to its goal of becoming climate-neutral through the European

Green Deal that will reduce net greenhouse gas emissions by at least 55% by 2030, compared to 1990 levels, and "transform the EU into a modern, resource-efficient and competitive economy, ensuring no net greenhouse gas emissions by 2050", in accordance with the Paris Agreement [2].

A relevant role within this framework is expected to be played by clean hydrogen, produced from renewables, nuclear or fossil fuels with carbon capture, utilisation and storage (CCUS), to which a large section and substantial investments are also dedicated within the Italian PNRR [3].

The fact that its use is not linked with any CO_2 release and almost no air pollution makes it a solution for decarbonising the so-called "hard-to-abate" sectors where emission reduction is hard to be achieved, such as iron and steel industry, as well as other energy-intensive industrial processes (e.g. cement production), transport (e.g. heavy-duty vehicles and rail), power generation and buildings.

In particular, priority must be given to renewable hydrogen, namely hydrogen obtained starting from water electrolysis using renewable electricity, keeping in mind that, in the short to medium term, low-carbon hydrogen production is required, obtained from fossil fuels with CCUS.

A strong growth in the demand for hydrogen and the adoption of cleaner technologies for its production is expected in the next years. According to IEA's Net Zero Emissions Scenario, the adoption of hydrogen and hydrogen-based fuels will avoid the emission of up to 60 Gt of CO_2 between 2021 and 2050 , representing 6.5% of total cumulative emission reduction [4].

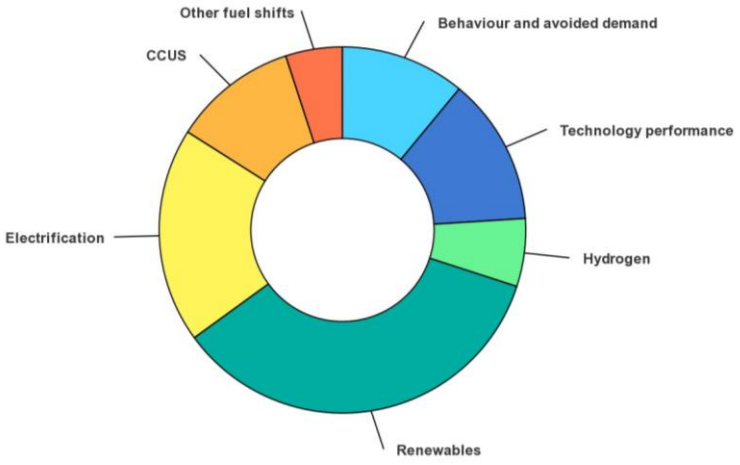

Figure 1.2 - Emission reduction by mitigating measure in Net Zero Scenario [5]

A further factor in favour of an increasingly dominant role for hydrogen is the possibility of addressing some of the problems associated with the inherent intermittency of renewable power generation such as wind and photovoltaic, both of which are weather-dependent and cause fluctuations in the electricity balance. The hydrogen storage potential can be a trump card for storing excess energy produced from renewable sources, so as to have a better match with demand and increase the flexibility of the electric grid.

In 2022, hydrogen accounted for less than 2% of Europe's energy consumption, 96% of which was produced with natural gas, resulting in significant amounts of CO_2 emissions [6]. However, the European Commission's strategic vision for a climate-neutral Union, published in November 2018, envisages the growth of the share of hydrogen in the European energy mix to 13-14 % by 2050 [7].

If all the planned projects were to succeed, an international hydrogen market could be realised, which would not only allow diversification of possible energy suppliers in view of greater energy security but would also be based on an annual production of 16-24 Mt of low-carbon hydrogen, of which 9-14 Mt would come from electrolysis and 7-10 Mt from fossil fuels with CCUS. As for the first case, it would correspond to an installed electrolyser capacity of 134-240 GW by 2030, that coincide respectively to total installed renewable capacity in Germany and in all Latin America [8].

1.1. Hydrogen supply chain

In this section, an overview of the hydrogen supply chain is given, as depicted in Figure 1.3, taking into account the current state of the art and integrating possible developing solutions that may play a leading role in the future hydrogen economy. Particular focus is dedicated to production, which is the most critical stage for costs and emissions, and transport, whose role is to efficiently connect the points of production and consumption.

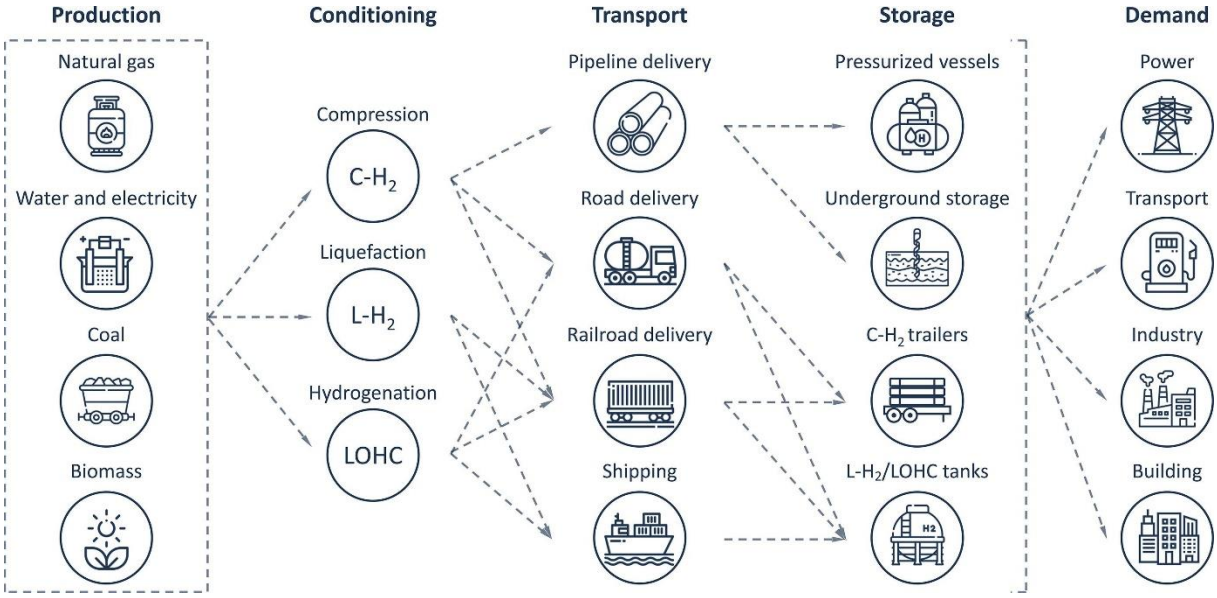

Figure 1.3 - Overview of the hydrogen supply chain options [9]

1.1.1. Hydrogen production

There are several processes by which hydrogen can be obtained and they differ from each other already on the basis of the source from which they start, which can be fossil fuels, water or biomass, since hydrogen is available on Earth only in compounds with other elements.

At present, the overwhelming majority of hydrogen produced on a global scale comes from steam methane reforming (SMR) of natural gas, which is the most exploited resource for this purpose, amounting to about three quarters of annual production. This path is likely to remain relevant in the short term, considering that world gas production is expected to grow to double its 2000 levels in 2030 [10], [11].

In this process, the natural gas is first catalytically treated with hydrogen to remove sulphur compounds. Then, the desulfurized gas is reformed by mixing it with steam and passing it over a nickel-alumina catalyst to produce CO and hydrogen. This step is followed by a catalytic water-gas shift reaction, as written in equation (1.2), to convert CO into hydrogen and CO_2. As a final step, the hydrogen gas is purified. If the by-product CO_2 is to be sequestered, a separation process must be added to capture it. The reforming reactions are as follows:

$$CH_4 + H_2O \rightarrow CO + 3H_2 \tag{1.1}$$

$$CO + H_2O \rightarrow CO_2 + H_2 \tag{1.2}$$

The overall reaction is:

$$CH_4 + 2H_2O \rightarrow CO_2 + 4H_2 \quad (1.3)$$

Natural gas in the SMR process is involved both as a fuel and as a raw material (along with water). Typically, 30-40% of it is burnt to fuel the process, resulting in a "diluted" CO_2 stream, while the rest is broken down by the process into hydrogen and more "concentrated" CO_2 [11].

The energy efficiency of the SMR process ranges from 85% (at HHV) to 90% when part of the input heat is recovered, but is roughly halved for small-scale reforming units [12].

Alternative processes are partial oxidation (POX) and autothermal reforming (ATR): in the former case the desulfurized gas is combined with air before the partial oxidation reaction takes place to produce CO and hydrogen, while the latter is a hybrid process involving both steam and pure oxygen.

Coal then takes 23% of the remaining hydrogen production slice of the market, with China playing a large part in this number [10]. Coal gasification (CG) is the oldest method of producing hydrogen and consists of producing syngas from coal. The CO_2 emissions from this practice are the highest, as 80% more CO_2 is released from coal combustion than from the combustion of natural gas [11]. The working energy efficiency can reach 67% at HHV, but 11 kg of CO_2 is released into the atmosphere for every 1 kg of hydrogen produced, based on the stoichiometry of the overall reaction [12].

The dominance of fossil fuels as a resource from which to produce hydrogen is very heavy on the environment, accounting for 2.5% of global emissions in energy and industry. Carbon capture, utilisation and storage (CCUS) plays a key role in getting closer to environmental goals, allowing up to 90% of the emitted carbon to be captured and with CO_2-capture efficiency expected to reach 85-95% [13], but at the same time generates an increase in cost. In fact, the levelized cost of hydrogen (LCOH) from SMR varies between 0.7 and 1.5 €/kg H_2, which reaches 1.6-1.9 €/kgH_2 when using CCUS (2014) [14], [9].

Besides fossil fuels, hydrogen can also be produced from water and electricity via electrolysis and from biomass via biomass gasification.

Hydrogen production via water electrolysis amounts to only 0.1% of global production, of which 40% is defined as 'green' and involves electricity from renewable energy sources (RES), which include wind and solar energy, biomass, hydropower, as well as tidal, geothermal and wave energy. Great interest has arisen around green hydrogen production as it avoids the emission of almost any greenhouse gas (GHG) and allows hydrogen to be used to alleviate the shortcomings of renewables, including volatility and a difficult balance between demand and response [9], [15].

The overall water electrolysis reaction can be written as:

$$H_2O \rightarrow H_2 + \frac{1}{2}O_2 \tag{1.4}$$

Several technologies have been developed for water electrolysis which, despite working with different materials and conditions, are united by their operating principles. The main ones are alkaline water electrolysis (AWE), proton exchange membranes (PEMs), alkaline anion exchange membranes (AEMs), and solid oxide water electrolysis (SOE) [16].

A comparison of their main advantages and disadvantages is given in Table 1.1.

Table 1.1 - Pros and cons of main water electrolysis technologies [17]

	Advantages	**Disadvantages**
AWE	Technology readiness No noble-metal catalyst High stability	Gas crossover High molarity of electrolyte Limited current densities
PEM	Technology readiness High purity of gases High current densities	Acidic electrolyte Expensive components
AEM	No noble-metal catalyst Low molarity of electrolyte	Limited stability Development phase
SOE	High efficiency High working temperature	Limited stability Development phase

The cost of renewable hydrogen is expected to rise from $6.00 (around €5.10, in 2021) per kilogram in 2020 to $2.50 (€2.12) per kilogram in 2030, but the continued reduction in RES electricity prices, together with a lower cost for electrolysers (expected to halve in 2050), could lead to even better outcomes [18], [13].

Finally, there are two possible alternatives for producing hydrogen from biological processes, both of which have in common the conversion of solar energy into chemical energy via photosynthesis [11]:

- via photosynthetically produced biomass and subsequent thermochemical treatment;

- via photobiological processes using certain types of bacteria, usually cyanobacteria (research phase).

1.1.2. Hydrogen transport

A critical factor in the realisation of a future hydrogen economy is the development of a transport system that is both cost-effective and reliable.

There are multiple options for transporting hydrogen from the production site to the site of use, and the choice must be made on the basis of several factors that will be discussed in the following.

First of all, it is useful to make a distinction between transporting pure hydrogen, a blend of hydrogen and natural gas and hydrogen carriers, i.e. larger molecules that make it easier to handle the hydrogen from which this element will then come.

1.1.2.1. Transport of pure hydrogen

Two possibilities exist with regard to the storage and transport of hydrogen: compression or liquefaction. This is due to the low density that this gas assumes in ambient conditions and which makes its handling more difficult than, for example, natural gas. Both processes require energy, and liquefaction in particular is the more energy intensive of the two. For example, supposing you wanted to compress from an initial pressure of 30 bar, a typical value at electrolysers and SMR outlets, to 160 bar, you would need 1kWh$_e$/kg$_{H2}$ for compression and about ten times as much for liquefaction [9].

At the distribution level, the most frequent choice nowadays for distances of less than 300 km falls on compressed hydrogen trucks, with a single trailer capable of transporting up to 400 kg$_{H2}$ in metal cylinders at 200 bar or 1100 kg$_{H2}$ in cylinders made of composite material and with pressures of 500 bar (although the values actually achieved are often lower due to regulations in the various states). For longer distances, insulated cryogenic tanker trucks are used instead, carrying up to 4000 kg of liquefied hydrogen at -240.2 °C [9], [10].

When it comes to large distances, as is the case with oil and natural gas, it is more convenient to transport hydrogen via pipelines and ships.

Nowadays, there are still no ships dedicated to transporting pure hydrogen, which would be transported after being brought to a liquid state, but these will not be too different from those used for liquefied natural gas (LNG).

For long distances, greater than 500 km, transporting hydrogen gas via pipelines is the most efficient, economical and environmentally sound method of supplying large quantities of gas, which can justify the initial CAPEX of installing a hydrogen pipeline, linked to right-of-way, labour and material costs [19].

Taking into account both capital and operating expenses, in the case of pipelines, the cost of transporting hydrogen gas over a distance of approximately 1500 km is estimated to be around $1/kg$_{H2}$, while the total cost of moving and converting hydrogen in the case of ships is approximately $2/kg$_{H2}$ [10].

1.1.2.2. Transport of natural gas-hydrogen blend

While transporting hydrogen via pipeline is the most cost-effective way in the long run, the need for a dedicated infrastructure can be a major barrier. Hence the idea of transporting hydrogen mixed with natural gas within the existing natural gas network. This not only allows hydrogen to be delivered in considerable quantities over long distances, but also reduces the investment cost and implementation time compared to the construction of dedicated H_2 pipelines [20].

Since there are about 3 million natural gas transmission pipelines worldwide, this option would be a practical way to increase the presence of hydrogen in energy systems and give a real boost to the development of a hydrogen economy [10].

At the downstream end-use level, there are two possible scenarios. In the first, hydrogen is extracted from the blend by means of separation technology, in the second, the blend is directly used in conventional applications [21].

The physical and chemical properties of the two gases are significantly different and this must be taken into account when blending.

For example, the volumetric energy density of hydrogen is around one-third that of natural gas. Consequently, as the percentage of hydrogen in the blend increases, the calorific value of the blend decreases and a greater volume of gas must be supplied to meet the same energy demand [21].

Some components along the natural gas value chain are able to work well with high percentages of hydrogen, while others are less adaptable. The overall tolerance of the entire grid depends on the components with the lowest tolerance. For instance, many gas heating and cooking appliances in Europe are certified for hydrogen contents of up to 23%, but the long-term effects are still uncertain [10].

1.1.2.3. Pipe-in-pipe

The transportation of pure hydrogen through pipelines is feasible only by relying on a new infrastructure where material selection is suitable for the intended purpose. Existing grid components might be susceptible to contact with hydrogen under operational conditions, and this susceptibility needs to be locally tested.

On the other hand, transporting hydrogen within blends with natural gas is considered a retrofit operation. This approach would allow the use of the current infrastructure designed for natural gas, with limits for hydrogen content. These limits

are currently being examined, and they might become less restrictive with appropriate adjustments to certain infrastructure components.

The pipe-in-pipe model represents an intriguing possibility. It enables the transportation of pure hydrogen without mixing it with natural gas and can also be applied as a retrofit solution, utilizing the existing pipelines. This concept involves placing a smaller inner pipe within a larger outer pipe, creating separate regions for transporting two fluids. This arrangement facilitates the transportation of hydrogen through the inner pipe while allowing natural gas to flow in the annular space, in contact with the existing natural gas pipeline. The simultaneous transport of hydrogen and natural gas would meet the energy demands expected in the near future, where hydrogen consumption is expected to grow and natural gas is still used. At a later stage, it is possible to consider no longer delivering NG and using the annulus as a safety cushion gas layer for the internal hydrogen pipe.

In this case as well, it is necessary to use a material that is suitable for operating in the presence of hydrogen, especially at the transmission level that is characterized by higher pressures and more demanding conditions than the distribution level.

1.1.2.4. Hydrogen carriers

Alternative delivery methods are being developed, which consist of incorporating hydrogen into larger molecules that facilitate its handling and transport, including ammonia and liquid organic hydrogen carriers (LOHC). They all require additional processing steps [22]

Ammonia passes to a liquid state at -33 °C and contains 1.7 times more hydrogen in a cubic metre than liquefied hydrogen, facilitating its transport [23], [24].

Ammonia has an international transmission and distribution infrastructure on its side, so it is not difficult to imagine it being transported by pipeline even over long distances: a pipeline of no less than 2400 km exists in the region between Ukraine and Russia, and in the United States there are pipelines totalling 4830 km in length [10].

It is necessary to consider that ammonia is a toxic chemical species and that there may be limitations in its use, as well as the risk of particulate matter formation and acidification following the incomplete combustion of ammonia. In fact, dehydrogenation technology to obtain hydrogen from ammonia is still being developed [24].

To generate a LOHC, the procedure involves loading these molecules with hydrogen with the advantage that liquefaction is not required to be transported as a liquid. The hydrogen is then extracted and used.

Energy is required both to convert hydrogen into LOHC and ammonia and, vice versa, for their reconversion back to hydrogen. For LOHC each of the two processes requires

a contribution equivalent to 35-40% of the hydrogen itself, for ammonia between 7% and 18% [10].

Both of these solutions can be competitive with long-haul transport pipelines in terms of cost (complete with conversion and conversion costs), especially if sea passage is required. The cost of moving and transporting hydrogen by ship for 1500 km is $1.2/kg$H_2$ for ammonia and half that, $0.6/kg$H_2$, in LOHC form [10]

1.2. Thesis outline

From what has been discussed so far, it becomes evident that hydrogen can play a strategic role in the energy transition and in achieving greater energy security. It is indeed included in national and international plans that focus on energy and environmental development.

To establish a functional hydrogen economy, it is crucial to connect hydrogen production sites with usage points, ensuring a mutual balance between supply and demand, and this requires an efficient transmission and distribution network. There are various methods through which hydrogen can be transported, and among these, pipeline transportation appears as the most efficient, economically feasible, and environmentally safe method when dealing with large quantities and significant distances.

In this context, retrofitting plays a crucial role, as it enables the reuse of the existing natural gas infrastructure, which is well-developed, extensive, and interconnected. This avoids the need to construct a new dedicated network for hydrogen. In this regard, the pipe-in-pipe concept emerges as a promising option, accommodating the growing hydrogen demand while maintaining a significant natural gas flow, which is projected to remain substantial for decades.

The objective of this thesis is to investigate the behaviour of the pipe-in-pipe system in the context of hydrogen transportation, particularly at the transmission level, where operational pressures are higher, and working conditions are more demanding both in terms of stress and issues related to hydrogen exposure (such as hydrogen embrittlement of steels). For this purpose, the use of fibre-reinforced polymers (FRP) is being evaluated as materials for the fabrication of the inner tube, which operates in contact with pressurized hydrogen.

An experimental analysis of these materials is conducted to determine their characteristics in terms of roughness and hydrogen permeability, exploiting the facilities available at the ITA Institute (Institut für Textiltechnik) of RWTH University in Aachen, Germany, where I had the opportunity to do a four-month internship, having been awarded the “Thesis Abroad” scholarship following selection by Politecnico di Milano.

This is followed by a numerical analysis, performed using the MATLAB® programming language, that investigates the performance of the pipe-in-pipe system in the aforementioned context.

The structure of the thesis is organized as follows.

Chapter 2 provides an overview of the current state of hydrogen transportation through pipelines. It discusses the compatibility of metallic and polymeric materials when in contact with hydrogen and explores the feasibility of transporting hydrogen in a blend with natural gas – an increasingly considered approach by various countries, evidenced by numerous projects. The chapter then delves into the discussion of steel pipelines currently used for hydrogen transportation and introduces pipelines constructed from FRP materials, outlining their respective characteristics.

Chapters 3 and 4 summarize the experimental analysis conducted on FRP specimens. In particular, glass fibre-reinforced epoxy resin (GFRE), carbon fibre-reinforced epoxy (CFRE) e glass fibre-reinforced polypropylene (GFRPP) are considered. In Chapter 3, the focus is on the surface roughness measurements carried out on specimens cut from tubes fabricated using the multi-filament winding (MFW) technique. These measurements are conducted using a digital microscope. In Chapter 4, the discussion centres around hydrogen permeation measurements, which are undertaken using a modified version of the electrochemical method outlined in the ISO 17081 standard for metallic materials, adapting the technique to suit the characteristics of the materials under consideration.

Chapter 5 describes the fluid dynamics model that is utilized in the subsequent chapters, beginning with Chapter 6, where a study on blend transport is conducted as the reference case. The analysis is divided into two scenarios: one involving the transportation of an equal amount of energy for all blends with varying hydrogen percentages, and the other involving a retrofit of the natural gas infrastructure. This retrofit specifically pertains to compression stations, which are located at the same distance and operate with identical inlet and outlet pressures.

Finally, Chapter 7 revolves around the pipe-in-pipe model. It commences by examining the influence of the diameter ratio between the two tubes on pressure losses. The analysis then seeks to identify the value of this diameter ratio at which the pressures of the two gases on the inner pipe's walls are equal. This condition is recognized as optimal, since, disregarding occasional pressure fluctuations at the transmission level, it represents the best situation in terms of mechanical stress. Consequently, it allows for a focus on hydrogen permeation and ensures that both hydrogen and natural gas are recompressed at the same distances. Additionally, the chapter encompasses a study on permeation through GFRE and the contamination of natural gas in the annulus due to hydrogen that has passed through the inner pipe.

.

2 State of the art

This Chapter provides an overview of the state of the art of hydrogen transport via pipeline, focusing on the performance and challenges of the adopted materials. First, an overview of the compatibility of line pipe materials, both metallic and polymeric, with hydrogen is provided, with a particular focus on the consequences for mechanical properties and durability. Then, the topic of transporting blends of natural gas and hydrogen is discussed, which is currently the most studied solution for delivering hydrogen. Some of the major completed and future projects are presented, and a general overview is given of how the properties of natural gas are modified after H_2 injection and the existing possibilities for separating (almost) pure hydrogen from the blend. Next, fibre-reinforced polymers (FRP) are introduced together with the multi-filament winding (MFW) technique as innovative method for pipe production using these materials. Finally, a summary of the major existing pipelines, made of metallic materials, for hydrogen transport is provided, with a final analysis of the possible design of pipes made for the same purpose using FRP.

2.1. Hydrogen compatibility with line pipe materials

2.1.1. Steels

The correlation between hydrogen and changes in metal properties has been investigated extensively over the years. As early as 1875, W.H. Johnson [25] derived evidence of decreased toughness and breaking-strain of steel temporarily immersed in hydrochloric acid and sulphuric acid. The connection with the responsibility of hydrogen was soon established. In metallic materials, hydrogen ingress occurs after dissociation of hydrogen molecules on the surface into hydrogen atoms, which can diffuse through the interstitial sites of metal crystal lattices [26].

Of all the hydrogen-related mechanisms that can lead to fracture and degradation of the mechanical properties of materials, only a few can really be attributed to the transport of hydrogen via pipelines and can be grouped under the concept of hydrogen gas embrittlement at room temperature [27].

Hydrogen gas embrittlement (HGE, or simply HE) is the generic term used to describe the adverse effects that engineering alloys can experience in hydrogen gas at ambient

temperatures. Many metallic materials can suffer embrittlement in hydrogen gas environments: these include steels (especially high strength steels), stainless steel, and nickel alloys [27].

Exposure under pressure to hydrogen gas mainly affects adversely the fracture toughness and fatigue strength of steel pipes and other components working in contact with it within the network.

This fact is very decisive as fatigue crack growth and fracture resistance are aspects taken into account in fitness-for-service assessments of pressure pipes [28].

Several factors are recognised as affecting the susceptibility of a material to HE [29]:

- Strength of material and residual stress in material.
- Pressure, temperature and exposure time.
- Applied strain rate and surface condition of a material.
- Concentration or amount of hydrogen and amount of hydrogen trap.
- Metallic coatings and specific precipitates.
- Microstructure of a material.
- Heat treatment of a material.

Figure 2.1 provides a graphical summary of the main factors involved in the phenomenon of hydrogen embrittlement.

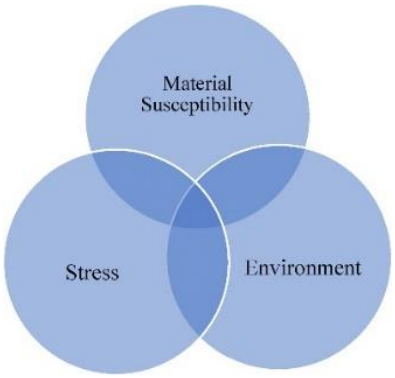

Figure 2.1 – Main factors involved in HE [29]

Several mechanical properties are considered when defining a material resistance to a quasi-static loading, namely tensile properties (i.e., yield strength, tensile strength, ductility) as well as fracture resistance properties (i.e., fracture toughness). Contrarily to what happens to yield and tensile strength, that are only slightly affected, the presence of gaseous hydrogen frequently results in a considerable loss in the ductility of steel, commonly characterized in terms of reduction in area at fracture or elongation to fracture (see Figure 2.2). Tensile tests conducted both in air and hydrogen gas lead

to a decrease in the area of fracture ranging between 20% and 50% in the second case [30].

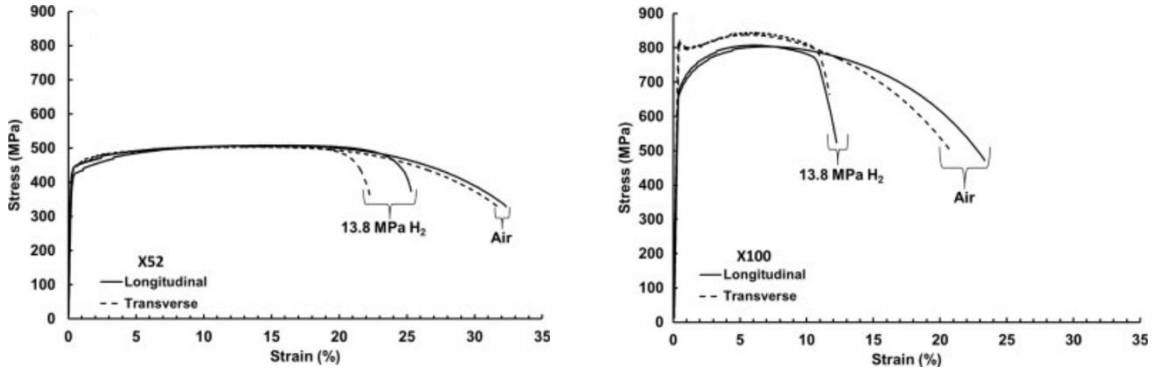

(a) X52 (b) X100

Figure 2.2 - Stress-strain curves of different metallic specimens, tested in 13.8 MPa hydrogen at strain rate of 0.007 s^{-1} [31]

As Figure 2.3 shows, tensile tests carried out on API L X52 iron in air and following the introduction of hydrogen through an electrolytic process by means of a 1 V voltage exhibit that the strain at break is significantly reduced (38%), while yield stress (3.8%) and ultimate strength (7.4%) are less affected [32].

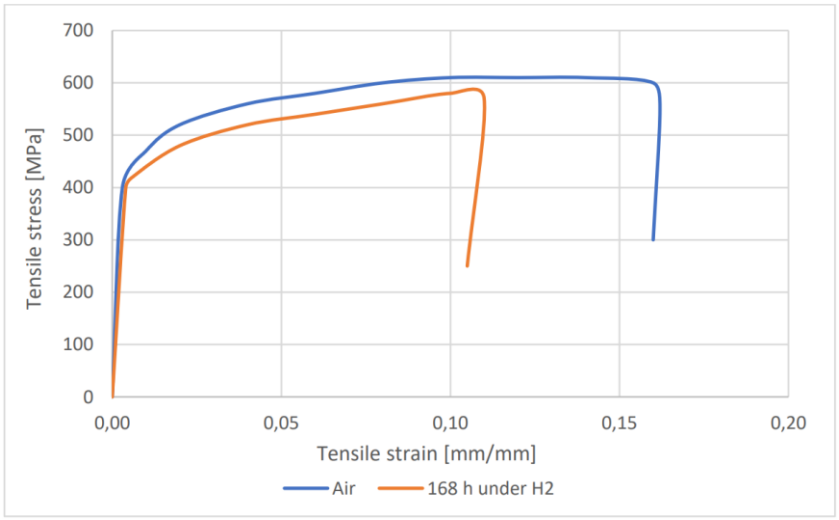

Figure 2.3 - Tensile test of API L X52 steel in air and after hydrogen introduction by electrolytic process under a potential of 1 V [32]

By means of fracture toughness tests, it is then possible to investigate the fracture resistance properties, typically represented by the critical stress intensity factor K_{Ic}, by

applying a monotonically increasing dynamic stress or strain to a fatigue pre-cracked specimen.

Depending on the grades tested in 6.9 MPa hydrogen gas, a decrease of approximately 48% to 60% is observed compared to tests performed in air. Crack growth resistance is also affected by this exposure, resulting in easier crack propagation [30], [28].

Exposure to hydrogen gas generates an increase in crack growth rate under cyclic pressure, reducing the pipe service life by 20-50% [33]. This can be examined through fatigue crack growth rate (FCGR) test, relating the crack growth rate per cycle da/dN to the stress intensity range ΔK, but, as can be seen from Figure 2.4, this effect is similar for all steel grades subjected to the same conditions. Various studies report an increase by one or two orders of magnitude in FCGR in steels exposed to hydrogen with respect to when exposed to air [30].

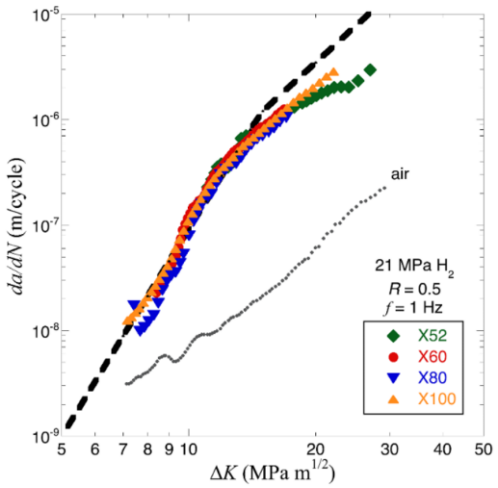

Figure 2.4 - Fatigue crack growth of different steels exposed to gaseous hydrogen [28]

Investigating the fatigue behaviour of a steel pipeline is therefore crucial in order to understand the outcome of pressure fluctuations and possible shutdowns and restart of operation [34].

Referring now more specifically to the natural gas grid, it is possible to differentiate the impact of hydrogen between steels used in the transport and distribution network. The former is the most critical section being characterised by higher pressures and higher strength pipelines (e.g. grades API 5L X60 and above) [35].

For example, the gas pipelines in the Italian national transport network are divided into land pipelines, whose maximum diameter reaches 1400 millimetres and operate at a pressure of between 24 and 75 bar, and submarine pipelines, with a diameter of between 500 and 600 millimetres and transport gas at a pressure of up to 115 bar [36].

In turn, the steel grades typically used in distribution (API 5L A, B, X42 and X46) are relatively low-strength and, although they may suffer a loss of tensile ductility and blistering, have a tendency to fail in a ductile, non-brittle manner [34].

Particular attention must be paid to the welds of a pipeline, which can be critical points and defects, critical microstructure, residual stresses and imperfections, especially related to the thermal cycling to which they are subjected. In the scientific literature there are contradictions regarding the resistance of welds to HE, which would appear to show sometimes better and sometimes worse performance than base metal, both in terms of tensile and fracture toughness tests and fatigue crack growth rates.

A quick way to predict the susceptibility of steels to HE is by computing the carbon equivalent (CE), that is based on chemical composition: the higher it is, the higher the degree of embrittlement. The main aim is to avoid the formation of untempered martensite during welding, being it extremely susceptible to HE [30].

Sulphur and phosphorus contents should not exceed 0.01 wt.% and 0.015 wt.% respectively in microalloyed steels, together with a CE lower than 0.35, to limit hydrogen embrittlement [30].

2.1.2. Polymers

Polymeric pipes are commonly employed in the distribution system with the aim of supplying gas to end users, characterised by operating pressures in the 0.04-5 bar range and smaller diameters than those typical of the transmission system [37].

Contrarily to metals, for polymers there is no need for hydrogen molecules to dissociate on the surface to have diffusion. They are typically considered as chemically inert to hydrogen and damage results predominantly from mechanical issues. This is the case with explosive decompression failure (XDF), generated by the decompression of high-pressure hydrogen absorbed within the polymer and leading to blistering, exfoliation and failure [38].

The properties of polymeric materials do not depend solely on their chemical structure, but are influenced by several factors such as the molecular weight (and relative distribution) of the macromolecular chains and the processing history, as well as their formulation involving the addition of additives, including fillers, plasticisers, etc. All this introduces great variability [39].

Data concerning the influence of pressurised hydrogen on mechanical properties and the effects of long-term exposure are necessary for pipe design. However, not many tests have been carried out on polymers to date. When it comes to long-term exposure of plastic materials to liquids or gases, three main phenomena can take place, namely diffusion of fluid molecules within the matrix, physical ageing and degradation. In all these cases, the mechanical properties are affected, through altered mobility of macromolecules and structural changes.

Polyethylene (PE) is a polymeric material whose use in the gas distribution network is more than well established. Castagnet et al. [40] performed tests on PE and PA11 (both currently used in gas transport) in a hydrogen environment. Tensile stress-strain curves were recorded to investigate mechanical behaviour and Differential Scanning Calorimetry (DSC) was also used in order to highlight any changes in the microstructure of the material (see Figure 2.5 and Figure 2.6).

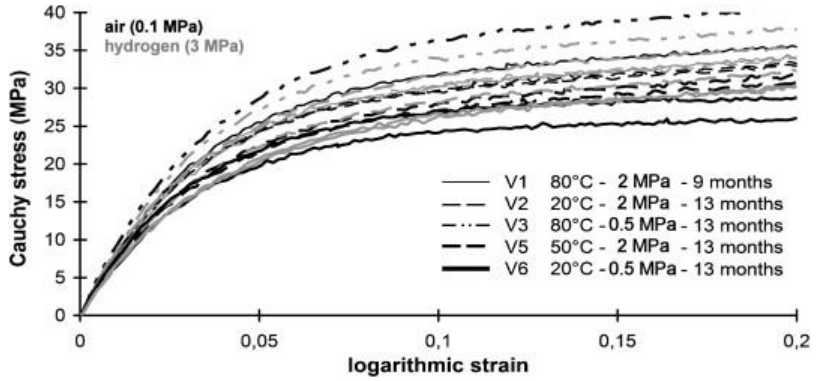

Figure 2.5 - Stress-strain curves for PE in air and 3 MPa H_2 after different aging histories [40]

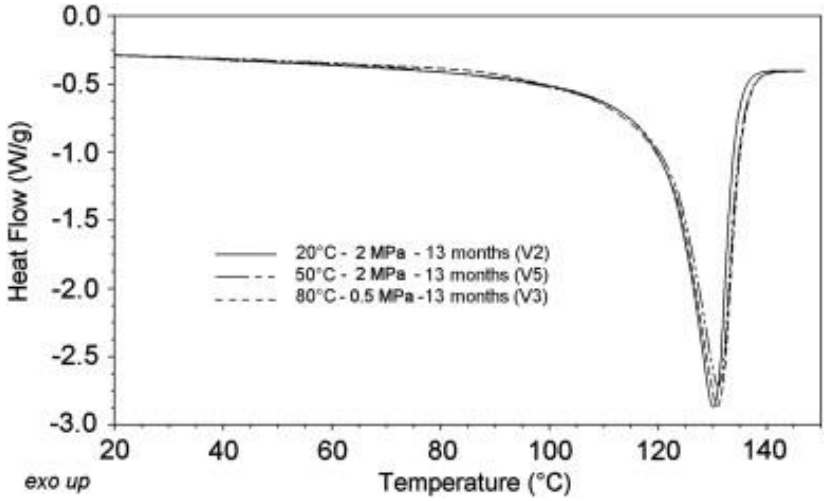

Figure 2.6 - DSC thermograms for PE samples with different aging histories [40]

The results lead to the assertion that long-term exposure (up to 13 months) to pressurized hydrogen doesn't cause deleterious effects neither on tensile properties nor on microstructure changes and that, therefore, the design of dedicated hydrogen pipes is feasible from data obtained from tests carried out in air, even over extended periods of use [40].

Supporting these conclusions in favour of polymer-hydrogen compatibility under pressure, also the project report [41] state how even in the case of uninterrupted

exposure to hydrogen for 4 years of PE80 and PE100 no form of degradation was found.

2.2. Hydrogen and natural gas blending

The gradual mixing of H_2 and NG is considered suitable for a first step towards the development of a hydrogen economy, enabling initial use of this gas to begin, especially in view of the transition towards increasingly low-carbon and sustainable systems.

Many projects are investigating the concept known as "power to gas" (P2G), in which hydrogen is produced from surplus or low-cost renewable electricity from solar and photovoltaic energy by means of water electrolysis. This hydrogen could be mixed with natural gas in the existing infrastructure, either for storage purposes or to be transported to end users.

The transition from one fuel to another brings with it numerous implications that could be more or less binding. One might mention, for example, the need for new regulations, safety codes that take into account different fuel characteristics, possible adjustments in personnel training, as well as technology that can effectively manage the transition and ensure that the end user's energy needs are met [42].

Stepwise increasing blends of hydrogen into the existing natural gas grid would certainly be more easily instituted than a complete fuel switch. It would not require significant capital investments and such onerous risks for stakeholders as there would be in creating new transmission and distribution grids.

Economic factors, on the other hand, weigh heavily in the choice of modus operandi. Consequently, countries that have extensive, widespread, and well-established natural gas grids would have great interest, at least in the short to medium term and perhaps even ultimately, in leveraging them for this energy transition.

It is then important to keep in mind the need to update existing national regulations and harmonize them among neighbouring countries, as this is the only way to really get a market started internationally. There are currently considerable differences, even between neighbouring countries (see Table 2.1)

Table 2.1 - Blending limits in different countries [43]

Country	Max H_2 concentration allowed in gas grid
Japan	0%
Netherlands	0.02% (plans for 0.5%)
Belgium	< 0.1% (up to 2% could be considered)
UK	0.1%
Italy	2%
Spain	5%
France	6%
Germany	10%

A graphical overview of the current hydrogen concentration limits in the gas is shown in Figure 2.7.

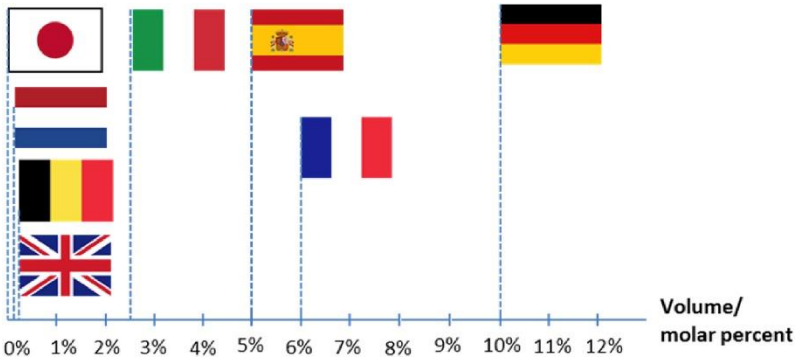

Figure 2.7 - Illustration of blending limits in different countries [43]

Among the opportunities in the short term to be exploited to boost hydrogen toward its increasing and widespread use, the IEA recognized precisely the possibility of replacing in the millions of kilometres of natural gas pipelines as little as 5% of the natural gas supply with hydrogen.

Considering the approximately 3 million kilometers of natural gas pipelines currently available around the world, using a 3% volume blend of hydrogen to meet global natural gas demand of 3900 bcm, as in 2018, would involve 12 Mt of H_2 [10].

However, hydrogen blending faces challenges that should not be overlooked, including [10]:

- Blending at 3% by volume would result in reducing the energy transported in the pipeline by 2% [44] due to the fact that the energy density of hydrogen is one-third that of natural gas. Therefore, larger volumes are required to meet the energy needs of users.
- Depending on the level of blending, there could be negative consequences on the equipment and this should be considered on a case-by-case basis based on the lowest tolerance found in the grid. End-use devices could also experience a negative impact as well.
- New safety measures should be developed and adjustments should be made to existing ones. New detectors are required, being hydrogen odourless, burn faster than NG, and the flame from it is not very bright.

Several studies have been performed, for example, on the European natural gas grid in order to examine how feasible its use is for extensive hydrogen storage and transport. One of the most interesting is the NaturalHy [45] project, funded by the European Community, which started in 2004 and ended in 2009. Its purpose was to investigate all critical aspects arising from transmission, distribution and use of such mixtures, paying particular focus on possible shortcomings in terms of safety, integrity and durability. As a result, the allowable percentage of hydrogen is limited and must be restricted, but admixture up to 10% has no negative consequences in most cases.

In contrast, other studies have disclosed that adverse conditions do not occur for hydrogen content up to 15-17% [42], [46].

However, these numbers must be approached with caution and seen as indicative values, as it is very complex to define a universal limit that succeeds in considering the great variability of conditions in which all pipelines and other network components are found.

2.2.1. Blending projects

Injection of hydrogen within the natural gas transportation network has been investigated since the 1980s.

Over the past decade, several projects have been pursued on the topic of mixing hydrogen and natural gas, mainly on the European continent, but not excluding, for example, the United States, Canada and Australia.

Table 2.2 shows some of the major completed, ongoing and future projects regarding the blending of hydrogen into natural gas.

Table 2.2 - Blending projects around the world [47], [22], [48]

Project name	Location	Blending ratio (vol %)	Start-up year
NaturalHy	EU	< 20	2002
WindGas Falkenhagen	Germany	2	2012
WindGas Hamburg	Germany	2	2015
Energiepark Mainz	Germany	0-15	2013
GRHYD	France	20	2014
THyGA	EU	0-100	2019
HyDeploy	UK	0-20	2018
H21	UK	100	2018
Snam	Italy	5	2019
Snam	Italy	10	2019
HyBRIDS	Italy	1	2025
SoCalGas	USA	1-20	2020
HyBlend	USA	1-30	2021
HyP SA	Australia	5	2021
HyP Murry Valley	Australia	10	2021
Fort Saskatchewan	Canada	5	2020
Cummins-Enbridge	Canada	2	2018

Starting from Italy, Snam, the leading European operator in natural gas transportation, with a network of about 38000 km in Italy and abroad, on April 1st, 2019 began the supply of hydrogen-enriched natural gas (HENG, or H2NG) to two industries in the Contursi Terme area in the province of Salerno in southern Italy. The test consisted of introducing a 5% blend of hydrogen and natural gas into the Italian gas transmission network and was the first of its kind in Europe. Carrying a 5% fraction of hydrogen out of the total gas flowing through Snam's networks in a year means injecting a

volume of 3.5 billion cubic meters, which corresponds to the annual consumption of 1.5 million homes. Translated into environmental terms, it corresponds to a reduction in CO_2 emissions of 2.5 Mt [48].

This test was the first stage in Snam's plan, which is to test the full compatibility of the infrastructure in the presence of blends with increasing fractions of hydrogen. Indeed, in December of the same year, the percentage of hydrogen injected was doubled, reaching 10%.

Snam's work was again made noteworthy when in 2021 it took the lead in the world's first supply test of a 30% hydrogen and natural gas blend in steel forging processes. It was used to heat the furnaces of the plant Forgiatura A. Vienna (Giva Group) in Rho (Milan, Italy), and neither alterations in the final product nor the need of adaptations to industrial burners were found. If such a blend, hypothetically derived from renewable energy, was permanently employed by the Giva Group's three plants, it would lead to an emission reduction of about 15000 tonnes of CO_2 annually, equivalent to the emissions of 7500 cars [49].

Another Italian project is HyBRIDS, which is based on an agreement between Società Gasdotti Italia (SGI) and Società Chimica Bussi (SCB) in Abruzzo, involves the permanent injection of green hydrogen into the gas network to achieve a 1% blend of hydrogen, with the goal of increasing this percentage depending on legislative constraints. The aim is to reach 10% and the planned duration is 24-36 months [50].

One of the most relevant projects at the moment is HyDeploy [51], which consists of the UK's first hydrogen blending project, launched in October 2019. The trial is based on three stages and uses a hydrogen content in the blend equal to 20% by volume.

In the first phase, laboratory tests were carried out for 18 months by Keele University to analyse the effects of the blend on the network and appliances: the blend was supplied to 100 homes and 30 university buildings. The results of this certified that blended at 20% does not adversely impact either infrastructure or housing components (such as boilers, hobs and cookers), and the UK Health & Safety Executive (HSE) confirmed that it is safe. The success of the first phase led to a second stage with larger-scale trial that had the goal, then achieved, of giving further confirmation that hydrogen could be added safely within the UK gas network. a 20% volume blend of hydrogen was again used. It lasted 10 months, until June 2022, and involved 668 homes, a school, several small businesses, and a church. In the final step HyDeploy aims to definitively demonstrate safety and economic feasibility in the practice of blending across the distribution grid so that the UK Government takes note and acts accordingly.

Moving to central Europe, the French project GRHYD was launched in 2014. Divided into two sub-projects, it focused on the Power-to-Gas (P2G) concept, i.e. using the surplus energy produced by wind to solar power and converting it into hydrogen,

then blended with natural gas. The tests were carried out with a 20% blend by volume and focused on the residential and transportation energy sectors [52].

In the meantime, the two projects WindGas Falkenhagen and WindGas Hamburg, respectively started in 2013 and 2015, were being developed in Germany, also focusing on the possibilities related to the P2G concept.

As mentioned, blending trials are not limited to the European continent, and two examples in the United States are the HyBlend Project [53], led by the National Renewable Energy Laboratory (NREL), with five other national laboratories working alongside it, and the SoCalGas Project.

The aim of the former is to investigate what effects the use of hydrogen-enriched natural gas (up to 30% of hydrogen) has on the compatibility of components in pipelines and buildings, the environment and costs [47]. In fact, three research tasks are to be pursued:

- Hydrogen compatibility of piping and pipelines, both with regard to metallic and polymeric materials.
- Life-cycle analysis (LCA).
- Techno-economic analysis, focusing on costs and opportunities for hydrogen production and blending.

The latter, on the other hand, plans to start with a 5% hydrogen blend that would be slowly increased to 20%. The purpose is to determine the feasibility of transporting renewable hydrogen within the natural gas system in operation in California [54].

2.2.2. Property changes

Hydrogen and natural gas differ significantly in both physical and chemical properties, as can be seen from Table 2.3. Therefore, the mixing of hydrogen with natural gas leads to a mixture with properties different from the starting properties, which cannot be neglected.

Table 2.3 - Overview of methane and hydrogen properties [55]

Property	Methane	Hydrogen
Gas density (kg/m³)	0.68	0.09
Boiling point (°C)	-161.6	-252.9
Minimum energy for spark ignition (MJ)	0.210	0.016
Auto-ignition temperature (°C)	600	560
Range of flammability (%vol)	4.4–17.0	4.0–75.0
Higher/Lower Heating Value (MJ/m³)	39.8/35.8	12.7/10.8

In all of the following considerations, it must be kept in mind that natural gas consists mainly of methane, followed by other hydrocarbons and inert species (such as carbon dioxide and nitrogen), with variable composition depending on the extraction point and on mixing with other types in the grid.

2.2.2.1. Physical properties

The addition of hydrogen affects both the density and viscosity of the mixture. Considering a blend of methane (which is by far the main constituent of natural gas) and hydrogen, it will possess a lower density than that of pure methane and this will impact the gas leakage flow rate, which will be higher than in the case of a pure methane pipeline.

Similarly, viscosity is affected, as can be seen from Figure 2.8: as the hydrogen fraction in the blend increases, viscosity decreases nonlinearly, with a significant drop for fractions greater than 50%.

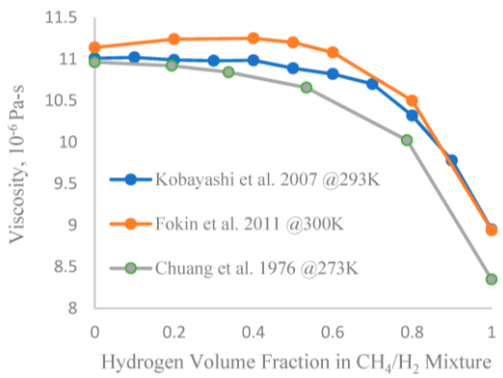

Figure 2.8 - Viscosity variation as a function of hydrogen fraction in methane [47]

Generally, the heating value of a fuel may be reported on two bases, the higher heating value or gross calorific value, and the lower heating value or net calorific value. The higher heating value (HHV) refers to the heat released from the fuel combustion with water in the flue gases in a condensed state, while the lower heating value (LHV) considers gaseous water as the product [56].

The higher heating value, density and specific gravity of hydrogen and natural gas are compared in Table 2.4.

Table 2.4 - HHV, density and specific gravity relative to air of hydrogen and natural gas [42]

	HHV (MJ/Nm³)	**Density**	**Specific gravity relative to air**
Hydrogen	13	0.084	0.07
Natural gas	40	0.65	0.55

The comparison of the values of HHV of hydrogen and natural gas shows how three times the volume of former is needed to have an equivalent energy transfer. Moreover, since hydrogen density is almost one-ninth of the other, a flow rate of hydrogen equal to three times that of natural gas would ensure a pressure drop approximately equal to that of NG, which is a key factor in pipeline design [44].

Figure 2.9 shows how the HHV changes with hydrogen fraction in the blend, both in MJ/m³ and MJ/kg.

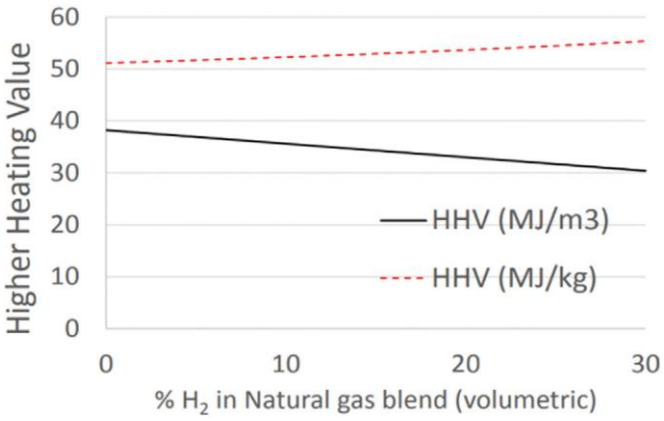

Figure 2.9 - HHV as a function of blending ratio [19]

Having to work with a higher volumetric flow rate to keep the energy transferred constant may require readjustments to valves, pipes and meters [19].

Therefore in the case of a mixture, to transfer the same energy, the volumetric flow increases and with it the gas velocity and pressure drop along the pipe. Instead, assuming an unchanged pressure drop, a lower amount of energy is transported in the case of hydrogen blends with respect to natural gas, with a monotonically decreasing trend up to a given upper limit. This can be seen in Figure 2.10, where comparisons are made with L-gas and H-gas. The former stands for "lean" natural gas and is a low-calorific NG; the latter is a "rich" natural gas and is a high-calorific NG [44].

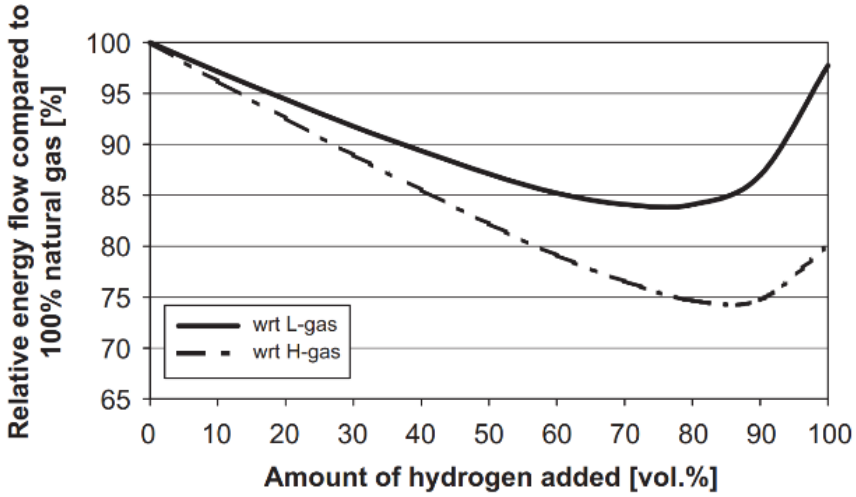

Figure 2.10 - Transported energy losses by blending hydrogen and natural gas, same pressure drop scenario [44]

2.2.2.2. Combustion properties

A commonly used index to assess the interchangeability of different fuel gases is the Wobbe Index (WI). If two gases have the same WI value and are burnt with the same burner nozzle and with the same nozzle pressure, they will release the same heat load [20], regardless of the calorific value. Therefore, the WI is the most important combustion parameter for gas appliances (except for engines) [57].

It is calculated as:

$$WI = \frac{HHV}{\sqrt{d}} \tag{2.1}$$

where d is the relative density compared to air (dimensionless).

Figure 2.11 shows the trends of HHV, d and the resulting WI for different blending ratios.

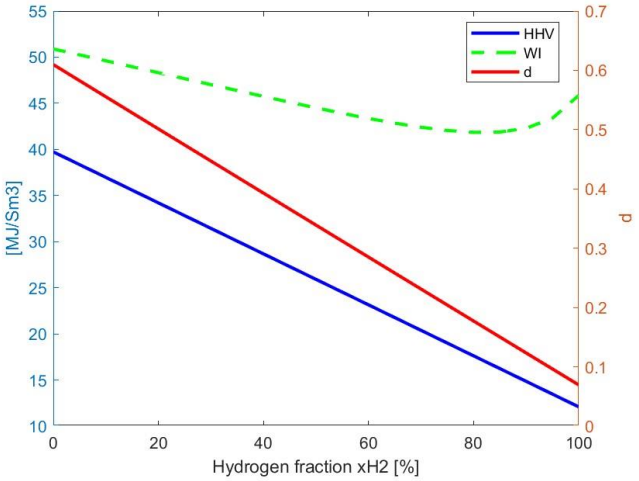

Figure 2.11 – Higher heating value, Wobbe Index and relative density of H_2/NG blends

As Figure 2.11 shows, while both d and HHV decrease linearly with higher fractions of H_2, the reduction of the Wobbe Index is less pronounced, and also non-linear.

Speaking of hydrogen admixtures in natural gas, it is also necessary to mention how the variation of the laminar combustion velocity S_L, which is crucial in the case of residential appliances being related to backfire and flame stability in premixed burners. In appliances, an increase in S_L could lead to so-called flashbacks, a phenomenon in which the local combustion velocity is higher than the local flow speed and, because of this, the flame moves upstream into the burner itself. This is precisely what happens in the case of the blend of hydrogen and natural gas (or methane) in appliances that were not specifically made to work under those conditions. The consequence is safety shutdown or even damage to the component. A 10% hydrogen mixture results in an increase in flame speed of approximately 5-10% [57].

It is then necessary to consider how the combustion temperature is changed if the burner is supplied by the blend and not by natural gas. In addition to possible damage to the end-use equipment by overheating, it may also be related to higher emissions of nitrogen oxides (NO_x), having high global warming potential and involved in ozone layer depletion and acid rain. Holding operating parameters such as air excess ratio λ constant, the adiabatic combustion temperature T_{ad} increases as the percentage of hydrogen increases, as shown in Figure 2.12 [57].

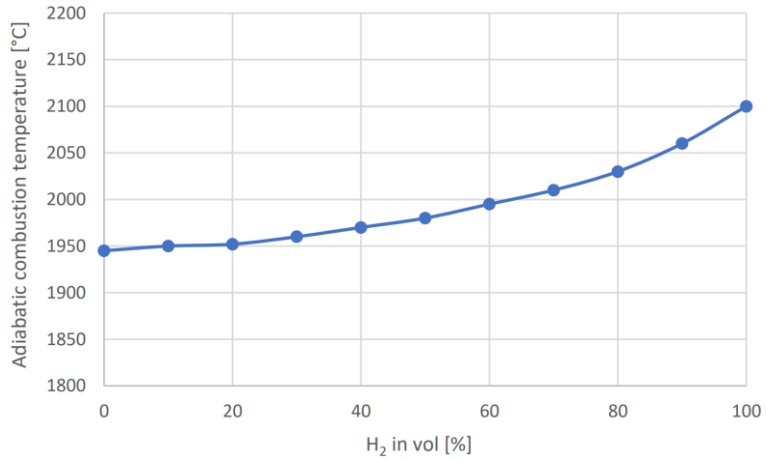

Figure 2.12 - Adiabatic combustion temperature for H_2/CH_4 blends [57]

As previously stated, the Wobbe Index is often used as the primary criterion to assess the impact of varying fuel gas compositions on combustion equipment, particularly for residential and commercial appliances, or to specify permissible gas qualities. Table 2.5 highlights why looking only at the Wobbe Index is insufficient when discussing the impact of hydrogen admixture on end-use equipment.

The methane blends were chosen in such a way that they have almost identical Wobbe Indices as pure hydrogen. It can be seen that, despite near identical Wobbe Indices, all other given fuel properties are very different when comparing H_2 with the blend.

Table 2.5 - Fuel properties at 15°C of different mixtures with similar WI [57]

	Unit	**100% CH_4**	**94% CH_4 6% CO_2 (v/v)**	**92% CH_4 8% N_2 (v/v)**	**100% H_2**
WI	MJ/m^3	50.64	45.28	45.27	45.78
HHV	MJ/m^3	37.80	35.53	34.78	12.10
d	-	0.5571	0.6157	0.5901	0.0698
T_{ad} (λ=1)	°C	1982	1971	1974	2096
S_L (λ=1)	cm/s	38.57	36.79	37.52	209

Two additional parameters that are changed by the addition of hydrogen and that are related to the area of safety are the Lower Explosive Limit (LEL) and the Upper

Explosive Limit (UEL), which indicate respectively the minimum and maximum concentration (in %) such that ignition of a gas or vapor can occur. Blend LEL and UEL are different from both pure methane (5% and 16%, respectively) and pure hydrogen (5% and 76.5%, respectively): if we consider a hydrogen fraction of 10%, the LEL and UEL are approximately 4.6% and 19.9%, respectively. As the hydrogen percentage increases, the explosive range also widens (see Table 2.6).

Table 2.6 - Explosive range as a function of blending ratio [19]

H_2 (%)	**0**	**20**	**40**	**60**	**80**	**100**
LEL	5.0	4.6	4.4	4.4	4.6	5.0
UEL	16.0	19.9	26.0	33.5	47.6	76.5

2.2.3. Hydrogen deblending

There are several methods to separate gases, such as absorption, adsorption, cryogenic distillation and membrane separation.

Gas absorption cannot be exploited to separate hydrogen blended with natural gas, since this process requires the use of a liquid solvent selective for hydrogen itself, which, however, does not exist [58].

Adsorption, on the other hand, is based on bond formation between gas molecules and a solid substrate, and Pressure Swing Adsorption (PSA) is the most industrially exploited technology for purifying hydrogen, ensuring a product with a high degree of purity and recovery [58], [59].

Cryogenic distillation relies on the partial condensation of gases and to do this must work at high pressures and very low temperatures. Such operating conditions drive up costs.

Finally, there is also the possibility of separating hydrogen by exploiting a pressure gradient using membranes, which make this process simple and cost-effective [58].

2.2.3.1. Pressure swing adsorption

PSA works by exploiting the principle of isothermal adsorption, according to which there is a characteristic correlation between the partial pressure of a gas and the adsorption of the gas by a material. As the gas pressure increases, the fraction of material adsorbed on the substrate surface also increases [34].

PSA is a versatile technology capable of producing high-purity hydrogen (99.99+%) from various gas mixtures [59]. Typically it is used for obtaining hydrogen from steam

methane reforming off-gas (SMROG) and refinery off-gases (ROG), and its use has become the state of the art in the chemical and petrochemical industries for the production of pure hydrogen from gas mixtures containing 60-90% hydrogen [60].

The principle behind this technology is based on the selective adsorption of certain molecules onto the surface of the adsorbent bed at relatively high pressure, leaving the desired gas flow undisturbed.

The bed materials are tailored based on the gas composition, and a wide variety of adsorbent families are available, such as zeolites, activated carbons, polymers, etc.

2.2.3.2. Cryogenic distillation

Cryogenic distillation processes are widely used for high degree purification of industrial gases, including oxygen, nitrogen, natural gas, argon, helium and hydrogen. It is a method that can be used to obtain 90-98% pure hydrogen with 95% recovery rate on a large scale [61].

It is a separation process that is carried out at extremely low temperatures, taking advantage of the different boiling temperatures of the different constituents of the gas to have a stepwise condensation of the gas feed. Accordingly, it is a very energy-intensive technology, yielding high OPEX. In particular, hydrogen is the element with the second lowest boiling point (20 K), beaten only by helium (4 K), so all contaminants will already be condensed when this temperature is approached.

2.2.3.3. Membrane technology

Membranes are barriers that can work by different mechanisms and allow the selective passage of certain molecules through them. Typical active mechanisms are the Knudsen diffusion, surface diffusion, capillary condensation, molecular sieving and solution diffusion (see Figure 2.13) [62].

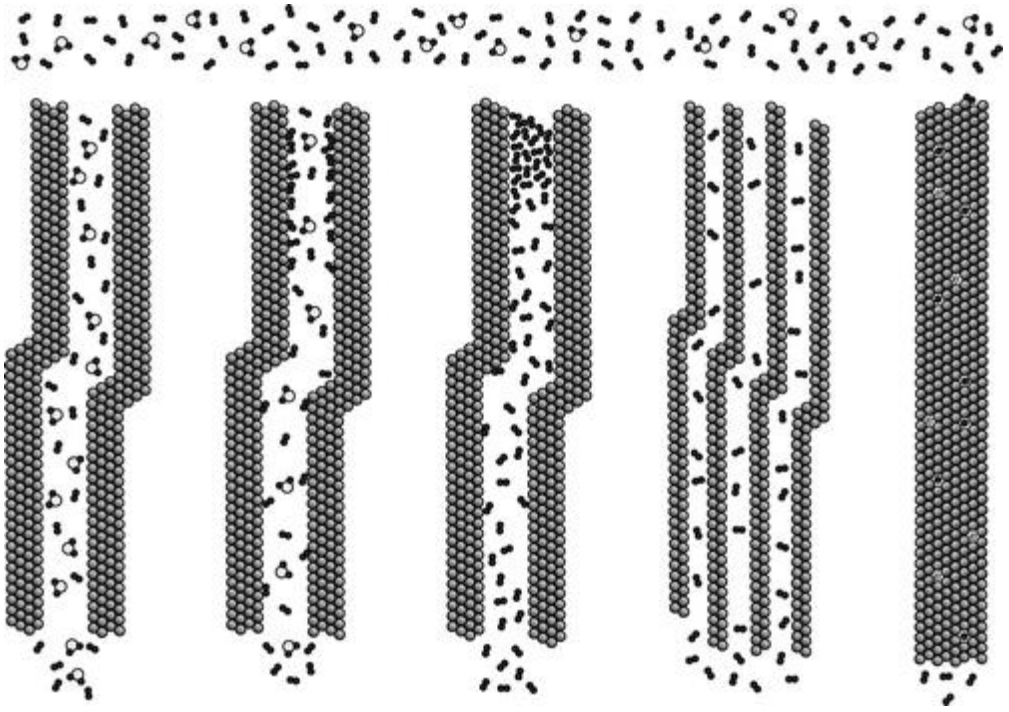

Figure 2.13 - Illustration of H_2 separation mechanisms [62]

Generally, membranes are categorized on the basis of their composition, and the main types are metallic, polymeric, carbon-based and ceramic membranes.

Membrane separation technologies are small in size, energy- and cost-efficient, and the mechanisms of operation are relatively simple. Some of them are capable of achieving degrees of purity of separated hydrogen close to 100%, but they typically need to work at high concentrations of hydrogen in order to be highly effective. For example, with some dense metallic membranes based on palladium, 99.999% pure hydrogen can be achieved, requiring, however, temperatures above 300°C [63].

In the case of dilute hydrogen mixtures there would be a need for higher pressure differential between the two sides of the membrane. This type of separation method could therefore find excellent application in transmission grid pipelines, which operate at considerable pressures [34].

The main advantages over PSA and cryogenic distillation include compactness, low maintenance, modular design, energy- and cost-effectiveness [64]. However, in addition to membrane material issues, one must also consider that the higher the pressure gradient, the higher the hydrogen flux through the membrane. However, this implies that the permeated stream has low pressure and may need recompression afterwards [63].

The hydrogen separation performance of different membrane materials is summarized in Figure 2.14.

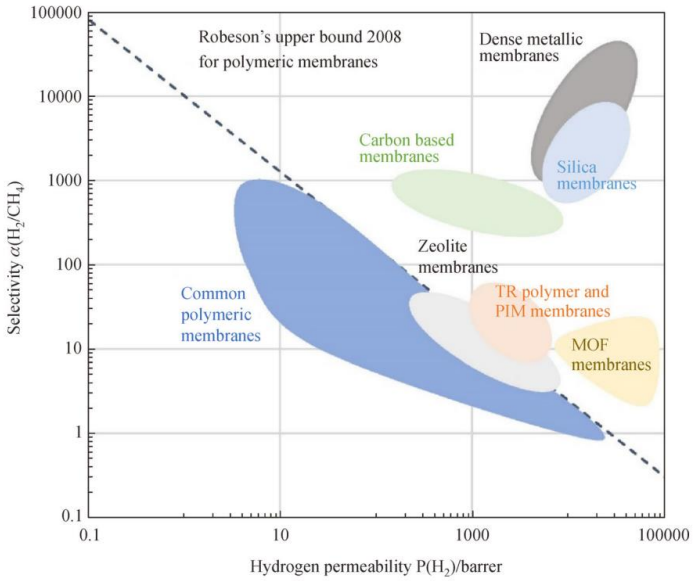

Figure 2.14 - H_2 permeability vs H_2/CH_4 selectivity of common membrane materials [65]

Metallic and polymeric membranes are the options available on a commercial scale.

Metallic membranes are dense sheets or films that have found great interest in obtaining very high purity hydrogen from a gas. The mechanism underlying the operation of this type of membranes consists of the dissociation of the hydrogen molecule due to the catalytic action of the metallic surface and the transport of hydrogen in the form of protons and free electrons, provided that a partial pressure gradient exists across the membrane [34]. Protons and electrons will reassociate on the low-pressure side, as can be seen in Figure 2.15. This process is unique to hydrogen and does not occur in the case of other gas constituents, such as CH_4, CO, CO_2 and so on. As a result, hydrogen can be separated with purity up to 99.999999% with this type of membrane [65].

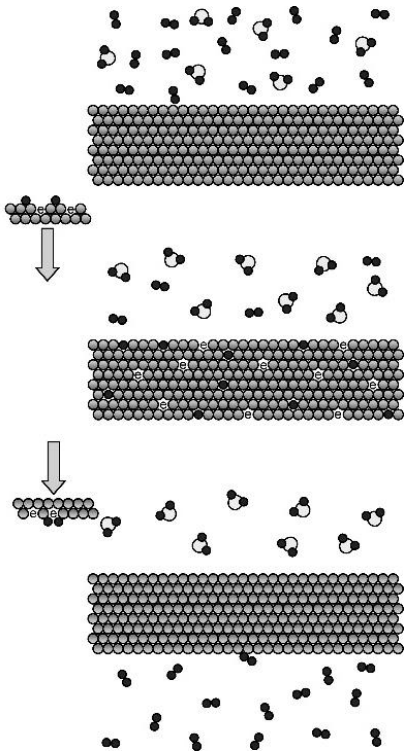

Figure 2.15 - Solution diffusion mechanism in metallic membrane [62]

There are several categories of metallic membranes for hydrogen separation, which can be divided into: (i) pure metals: Pd, V, Ta, Nb, and Ti; (ii) binary alloys of Pd: Pd-Cu, Pd-Ag, Pd-Y, and Pd alloyed with Ni, Au, Ce, and Fe; (iii) complex alloys: Pd alloyed with 3-5 other metals; (iv) amorphous alloys: typically Group IV and Group V metals; and (v) coated metals [66].

The metals that are most suitable for H_2 separation membranes typically have high H_2 permeabilities, high diffusivities or solubilities, and good thermal stability at elevated temperatures [62].

Palladium membranes are the most common metallic membranes used for hydrogen separation by solution-diffusion mechanism, however, requiring temperatures of about 400°C for proper operation [34]. They have some critical issues, including cost that can be prohibitive for their production and poison effects of sulphur-containing impurities, such as H_2S and CO in the feed gas. In addition, membranes with high diffusivity or solubility tend to be more prone to hydrogen embrittlement, which undermines their durability. Efforts have been made to overcome these adversities by alloying palladium with other metals, including silver (Ag), copper (Cu), gold (Au) and zirconium (Zr) [67].

The use of thin palladium membranes allows for increased hydrogen flow and recovery, but at the expense of mechanical strength. To cope with this problem, substrates such as Vycor glass (silica glass with symmetric structure and a mean

average pore size of 4 nm), porous ceramic α-alumina with asymmetric multilayer structure, ceramics and stainless steel (SS) are used. In the case of SS, one would take advantage of its mechanical stability, gas sealing ability and thermal expansion coefficient not too dissimilar to that of Pd[66].

The possibility of separating hydrogen from gas mixtures containing CO, hydrocarbons and nitrogen using polymer membranes is not new. As early as the 1970s, Dupont launched some products on the market based on the use of small-diameter hollow fibres.

Unlike other hydrogen separation membranes, these do not require high temperatures but, in general, the degree of purity they can guarantee does not reach the levels of other technologies, which are required in specific applications [62]. Advantages include low cost and ease of fabrication of hollow fibre or spiral wound modules with high surface area/volume ratio, but on the other hand, certain difficulties must be overcome, such as susceptibility to certain chemical species, including hydrochloric acid (HCl) and sulphur oxides (SO_x), and limited mechanical strength [66].

There is a characteristic limit in the performance of polymeric membranes, known as Robeson's upper bound, determined by a trade-off between gas selectivity and permeability (see Figure 2.16). As technology progresses, this limit will rise higher and higher, slipping toward increasingly optimal values.

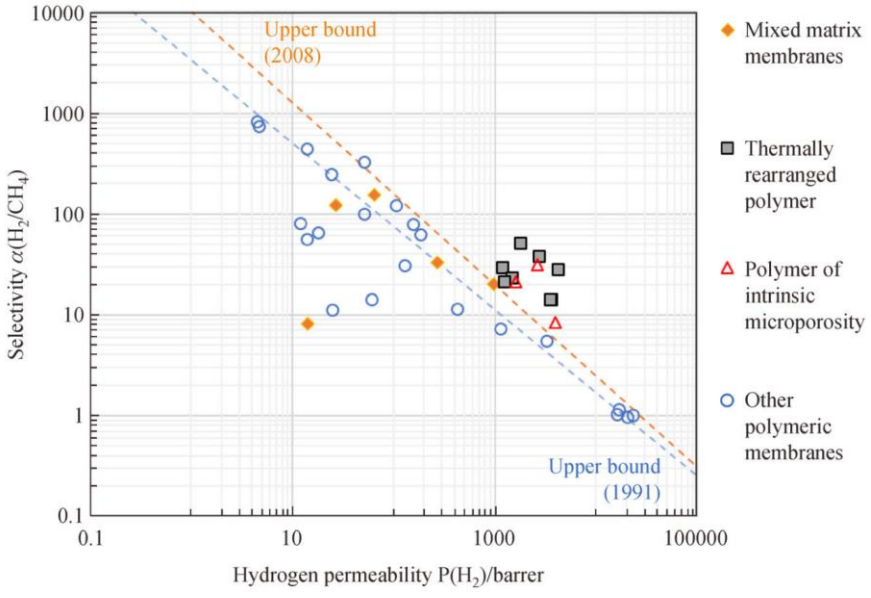

Figure 2.16 - Robeson's upper bound of polymeric membranes for H_2/CH_4 separation [65]

In recent years more than one membrane made at laboratory scale has succeeded in exceeding that ceiling between H_2/CH_4 selectivity and hydrogen permeability [65].

Such advancements include polymers of intrinsic microporosity (PIMs), thermally rearranged (TR) polymer membranes and mixed matrix membranes (MMMs) [67].

A recent product that has entered the market is Evonik's Sepuran Noble membrane [68], developed for hydrogen recovery and purification, providing an ideal instrument for separating hydrogen from natural gas when transported together in the natural gas grid. Evonik claims hydrogen recovery in excess of 90%, very high selectivity and efficiency even for low hydrogen partial pressures at the inlet.

2.3. Fibre-reinforced polymers

Composite materials are heterogeneous materials that combine two or more phases of a different nature. At least two of these must have sufficiently dissimilar properties to generate distinctive properties and different from those of the individual constituent materials, synergistically improving those of the final product [69], [70]. The different phases retain their individual identities and are distinguishable within the composite, they do not blend or dissolve, unlike mixtures or solid solutions [70].

Specifically, fibre reinforced polymers (FRP) are composite materials consisting of a polymer matrix, which represents the continuous phase, in which fibres are dispersed, and their union generates enhanced properties. They were originally commercialized to meet the high performance requirements of aerospace, automotive and marine industries as low weight-to-high modulus and strength materials [71].

The embedded fibres provide the greatest reinforcement contribution, being stronger and stiffer, while the polymer matrix holds them in place and protects them from environmental factors such as humidity and temperature [72]. The key to maximising the mechanical properties of the composite material lies in the interface between these two components, because it allows the transfer of stresses to and between the fibres [73].

Fibres are the fundamental elements, with diameters of the order of 10 μm, from which yarns are obtained, from which textiles can then be formed. The result of combining these with a matrix makes up the composite. Yarns can be either twisted or untwisted. From the interlacement of yarns, two-dimensional and three-dimensional textiles can be realised [74]. The following lines will refer to 2D textiles, with fibres that can be unidirectional, woven and nonwoven.

Nonwoven fabrics are simply obtained by bonding fibre webs together through mechanical, thermal or chemical action and fibres, contrary to woven fabrics, do not need to go through the preparatory/transitory stage of yarn spinning in order to be transformed into a web of a certain pattern [75]. Instead woven fabrics can be obtained by intertwining yarns at right angles to each other, obtaining different possible

patterns (see Figure 2.17). They show better dimensional strength in both weft and warp directions [76].

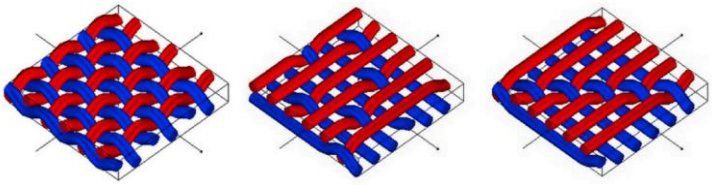

Figure 2.17 - Schematic representation of different weave patterns [77]

Finally, non-crimp fabrics are produced by arranging individual layers of unidirectional yarn on top of each other, each with a specific orientation according to the target application, as depicted in Figure 2.18. The different layers are then fastened together with knitting yarns. Compared to woven fabrics, they achieve better performance at the same weight or equal mechanical properties at a reduced weight.

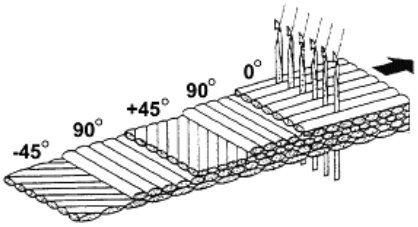

Figure 2.18 - Schematic representation of non-crimp fabric [78]

In terms of both matrix and fibres, the choice is quite varied. A brief summary is here provided.

The matrix can be both thermoplastic and thermosetting and a brief comparison between these two categories is done in Figure 2.19.

In the first case, we speak of linear or branched polymers which, by increasing the temperature to a characteristic value, switch to a viscous liquid state and are processable several times over. They can be either amorphous or semi-crystalline. Examples of thermoplastics used as polymer matrices are PP, PA, PE, PB, PEEK and PBT [79].

Thermosetting polymers, on the other hand, increase their stiffness and do not melt when heat is provided. This is related to the fact that their macromolecules are crosslinked, i.e., chemically bound, and cannot flow, preventing the polymeric material from behaving as a melt. Furthermore, they are insoluble and do not swell, unlike thermoplastic polymers. The transformation processes of thermosets involve

the use of precursors of low molecular weight and therefore low viscosity, which are subjected to the curing reaction due to a stimulus, forming a network. Different types of stimuli are possible: thermal input, light input, moisture input and mixing between two mutually reactive components. The wetting of fibres with resins is rather easy due to their low viscosity and good adhesive properties. These resins include polyesters, vinylesters, epoxies and phenolics [79].

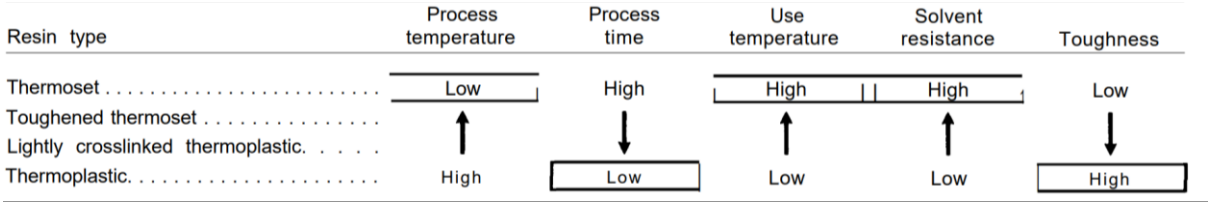

Figure 2.19 - Comparison of general features of thermoset and thermoplastic matrices [80]

As far as reinforcing fibres are concerned, it is essential to make a careful selection of fibre type and orientation in order to achieve tailor-made properties for the final application.

The most common options are glass fibre, carbon fibre and aramid fibre, for each of which there are different types or grades. Table 2.7 provides a summary of the relevant properties of these fibres.

Glass fibres are obtained from a mixture of metal oxides, including silica (SiO_2) in particular, and are the cheapest of all reinforcing fibres. The most commonly used grade in composites is E-glass, that is cheaper than S-glass, which contains a higher percentage of alumina and has higher tensile strength. Other examples are grade C and D, which respectively exhibit high chemical resistance and have low dielectric constant [81], [82]. The strength of glass fibres is higher than that of the bulk due to a reduced number of defects, but they exhibit the same Young's modulus as they have an isotropic structure [82]. Depending on the quality, the moduli are in the range of 70-85 GPa and the ultimate elongation around 2-5% [83]. In general, they have interesting mechanical properties, but, compared to the alternatives, they feature a lower elastic modulus and high density. They are also susceptible to moisture but can be protected with a suitable matrix.

Carbon fibres are defined as such if the carbon content exceeds 92 wt.%, while percentages above 99 wt.% are referred to as graphite fibres. Carbon fibres offer the best performance in terms of specific modulus and strength. A possible classification based on the mechanical properties divides them into ultra-high modulus (> 500 GPa), high modulus (> 300 GPa), intermediate modulus (> 200 GPa), low modulus (100 GPa), and high strength (>4 GPa) [84]. They do not absorb water, show no creep or relaxation, are electrically and thermally conductive, with a relatively low coefficient of thermal

expansion, and have high thermal and chemical stability in the absence of oxidising agents [83], [84]. Carbon fibres are nowadays mainly produced from polyacrylonitrile (PAN) and show high versatility, as well as high cost.

Finally, aramid fibres are obtained from aromatic polyamides (hence their name) and show moduli of 70-200 GPa, with ultimate elongation of 1.5-5%, depending on quality [83]. A well-known trademark is Kevlar, made of poly-p-phenylene terephthalamide (PPTA), used in applications where light weight, high strength, stiffness and fatigue resistance are required [81]. Kevlar fibres show five times the tensile strength of steel in air for the same weight and tend to have elastic behaviour. However, when bent, they deform plastically on the side subject to compression, which improves toughness and impact resistance [82]. Aramid fibres are cheaper than carbon fibres, however they are sensitive to high temperature, UV exposure and moisture [83].

Table 2.7 - Relevant properties of different fibres [85]

Fibre	**Density [g/cm³]**	**Elongation [%]**	**Tensile strength [MPa]**	**Elastic modulus [GPa]**
E-glass	2.5	0.5	2000–3500	70
S-glass	2.5	2.8	4570	86
Aramid	1.4	3.3–3.7	3000–3150	63.0–67.0
Carbon (PAN-based)	1.4	1.4–1.8	4000	230–240

2.4. Multi-filament winding

Filament winding (FW) is a fabrication technique for both close-end products, such as pressure vessels, and open-end products, such as pipes, made of FRPs [74].

This technique consists of winding fibre rovings under tension around a mandrel, which is rotated around its axis. These pass through a delivery eye mounted on a carriage that moves in a horizontal direction, parallel to the axis of rotation of the mandrel. Before being applied to the core body, the fibre bundles are passed through a liquid resin bath. Alternatively, it is also possible to use towpregs, i.e. pre-impregnated untwisted multifilament [74]. In the latter case, the winding speed can be tripled, although the material cost is higher. However, considering the increased productivity, FW is an economical manufacturing method, especially for components with a simple shape, and ensures good reproducibility of features. The last step

involves curing the matrix, which is usually performed in an autoclave or on the mandrel using UV radiation heaters.

This manufacturing process has evolved over time and led to the development of multi-filament winding (MFW), developed by Murata Machinery Ltd. (Kyoto, Japan), a manufacturer of advanced and innovative textile technologies. They presented the process at the 20th International Conference on Composite Materials and installed the MFW-48 system at the Institut für Textiltechnik der RWTH Aachen (ITA), Germany, in 2017 [86].

Figure 2.20 - MFW machine at ITA Institute of RWTH University, Germany [87]

The most important feature of such a filament winder is the multiple yarn system, which allows a high degree of design freedom and reduced manufacturing times, resulting in increased productivity and economic efficiency [88]. This technology has the ability to process 48 tows simultaneously, resulting in unidirectional, non-crimped structures. In contrast to traditional filament winding, the mandrel is moved horizontally back and forth while rotating around its axis, and in the process the fibres are wound around according to the desired pattern. During the rotation, an entire layer is placed down on the mandrel at the same time [87]. Figure 2.21 shows schematically the operating principle of MFW.

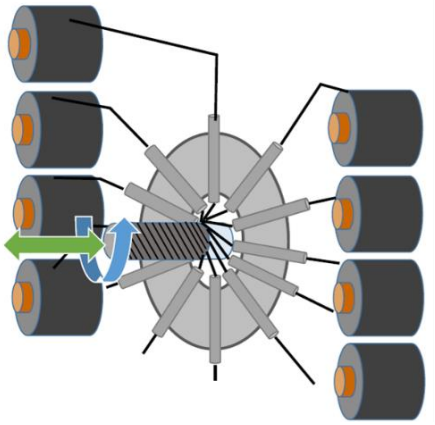

Figure 2.21 - Schematic representation of MFW working principle [89]

In this manufacturing process, there is also the possibility of wrapping the component with shrinking tape, which acts during the subsequent thermal cycle, so as to have a better compactness of the different layers, also removing excess resin and increasing the volumetric percentage of the fibres. The possibility of using the shrinking tape must be also taken into account for the considerations regarding surface roughness that will be made in Chapter 3.

2.5. Hydrogen pipelines

2.5.1. Existing steel infrastructure

Gas transportation via pipeline is now a well-established phenomenon in the energy sector, and this has been helped by the fact that it is a safe, cost-effective and environmentally sound solution to supply large amounts of gas.

The first hydrogen pipeline of considerable length was built in 1938 in Germany in the Ruhr region, and since then 4542 km of pipelines have been built around the world, mostly in Europe and US. Table 2.8 and Table 2.9 show the main hydrogen pipelines operators in Europe and North America, respectively. Typically, such pipelines have diameters in the order of 200 mm and are not very extended, just enough to connect industrial H_2 production sites to refineries and chemical industries [35].

Table 2.8 - Main operators and corresponding H_2 pipelines in Europe [11]

Operator	Network	Length	Country
Air Liquide	France Centre East	57	France
	France South East	42	France
	Le Havre	4	France
	Ruhr	240	Germany
	Monthey	2	Switzerland
	Priolo	6	Italy
	Leuna-Bitterfeld	135	Germany
Linde	Teesside	35	United Kingdom
	Rozenburg/Rotterdam	70	Netherlands
Air products	Teesside	5	United Kingdom
	Porto Marghera	2	Italy

Table 2.9 - Main operators and corresponding H_2 pipelines in North America [11]

Operator	Network	Length
Air Liquide	Edmonton	3
	Pennsylvania	3
	Louisiana	210
Air Products	Texas/Gulf Coast	390
	California	21
	Canada	10
	Texas and Louisiana	482
Praxair	California	< 10
	Indiana	< 10
	Alabama	< 10

The major actors of hydrogen transportation and distribution are Air Liquide, Air Products, Linde, and Praxair [11].

More than 1600 km of pipeline are currently dedicated to hydrogen in Europe, second only to the United States where the total length exceeds 2500 km, 983 km of which is operated by Air Products to supply hydrogen to refineries and chemical manufacturing along the Gulf Coast (Texas and Louisiana) [39].

The main adopted material is low-carbon steel (including ASTM 106, API 5L Grade B and API 5L X42/X52 steel), while the operating pressures are between 3 MPa and 5 MPa, with diameters up to 360 mm [22].

In Europe (see Figure 2.22), the greatest distance is covered by the pipeline operated by Air Liquide, which runs 1103 km distributed among France, Belgium, and the Netherlands, with an average diameter of 158 mm and service pressures of 10 MPa [22]. In Germany Air Liquide still operates today the first pipeline mentioned before. It is 240 km long, it has a flow rate of about 250 million Nm^3/year of hydrogen and it is still in service today, connecting about fourteen production sites [11].

Figure 2.22 - Air Liquide pipeline in France, Belgium, the Netherlands and Germany [11]

For the construction of new pipelines specifically for the transport of hydrogen, it would be necessary to start with the basic notions of natural gas infrastructure and implement them with additional measures that take into account the difference in the properties of the two gases in consideration.

Common design codes to refer to are EIGA (European Industrial Gases Association) guidelines and ASME B31.12 standard [35].

In the former, specifications are expressed both in general for metallic materials and more specifically for the different classes, especially aimed at combating the problem of hydrogen embrittlement. The main requirements for steels used in hydrogen pipeline service must have high toughness, maximum hardness of 22 HRC (Hardness Rockwell C) or 250 HB (Hardness Brinell), roughly corresponding to tensile strength of 800 MPa. The same limits apply to welds, which may lead to the need to use steel with a tensile strength below 500 MPa. Since these are more susceptible to HE, pre- or post-welding thermal treatments must also be evaluated [27].

A list of "significant metallurgical considerations" is also made, namely [27]:

- avoid alloys that are too hard or high-strength;
- prefer alloys that have fine-grained microstructures;
- avoid components with obvious internal and surface defects;
- minimise non-metallic inclusions, which undermine both HE strength and toughness.

ASME, on the other hand, suggests using greater thicknesses for pipelines working with 100% H_2, but recent research is optimising the choice of steels so that the required over-thicknesses can be reduced and larger diameters and pressures can be worked with [35].

2.5.2. FRP pipes

Existing pipelines currently dedicated entirely to hydrogen are mainly made of carbon steel, however, this technology cannot be relied upon if the desired goals in terms of performance and costs of network expansion and implementation are to be achieved [90].

As discussed in Section 2.1, steel pipelines suffer from hydrogen embrittlement when placed in contact with high-pressure hydrogen, resulting in a reduction in tensile strength, ductility, etc. This degradation could lead to premature failure of the component, resulting in leakage of gas and, in the worst cases, bursting. But there are also other critical aspects of steel pipes: due to their weight and size, they are difficult to handle, and both parameters should not be underestimated when considering the desired network extension.

Research is therefore being conducted into materials that can be used for hydrogen delivery at high pressures.

There is a growing interest in FRPs in this field of application, as this type of material would be able to overcome the issues of carbon steel in terms of cost, handling, weight, safety, welding and joining [91]. The use of polymers might also be considered, as they are already used to transport fluids and show high chemical resistance. However, they would not work well at high pressures, which is why fibres are added to them, in order to significantly boost the mechanical properties of the component. For example, pressure vessels made from FRP are able to withstand pressures exceeding 700 bar [92].

In addition to the simpler FRP-only pipe concept, which is based on that of conventional pipes made of metallic materials, it is also possible to think of a concept consisting of several layers, each of which is designated to perform a different task. Starting from the inside, there is a liner in direct contact with the fluid, which must guarantee the lowest possible permeation, a protective layer, an interface layer, several layers of composite material (usually CFRP, with carbon fibre, or GFRP, with glass fibre), an outer barrier layer and finally a protective layer [90].

The inner liner can be made of polymer such as high-density polyethylene (HDPE), which is a good candidate in terms of price and permeability, but other solutions, such as nylon, can also be used [39].

The central part made of composite material has the primary role of mechanically supporting the pressure inside the pipe while the outer protective layer works in direct contact with the environment and can be chosen depending on the context in which the pipeline must work [92].

Below is a list highlighting the strengths of pipelines made of polymer composite material [93], [94], [95]:

- FRP is an existing commercial technology currently employed in the oil & gas industry;
- improved burst and collapse pressure ratings, increased tensile strength, compression strength, and load carrying capacity, compared to non-reinforced, non-metallic pipelines;
- Reduced installation costs and improved reliability for H_2 pipes;
- Improved chemical and corrosion resistance and no susceptibility to hydrogen embrittlement;
- One-mile lengths can be spooled for delivery to installation sites and later emplaced as a seamless monolith;
- no welding and minimal joining (that are simple and can be performed on site);
- emplacement requirements are less stringent than those for metal pipeline (and therefore can be installed in areas where right-of-way restrictions are severe);
- sensors can be embedded directly into the structural wall of the piping, allowing to operate it as a smart structure (real time monitoring of parameter and conditions).

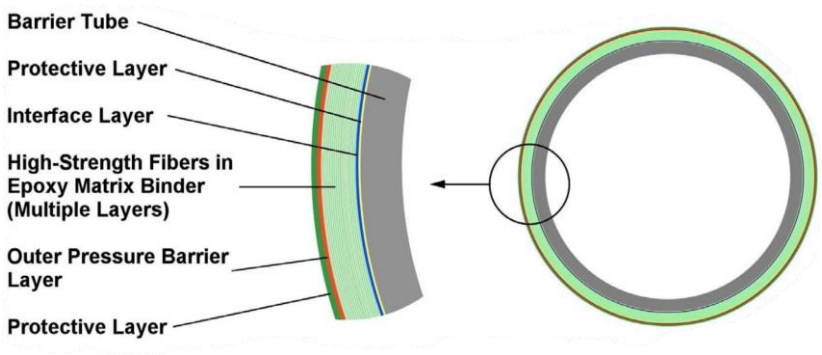

Figure 2.23 – Example of FRP pipe architecture [95]

3 Roughness tests on FRP

The roughness values of the pipe walls in contact with which the fluid flows are fundamental for the study of fluid dynamics. In fact, they fall within the expression of the friction factor (f) which is used to calculate the head losses along the pipe, according to the Darcy-Weisbach equation:

$$\Delta p = \frac{fL}{D}\,\rho\frac{v^2}{2} \tag{3.1}$$

The friction factor is a function of relative roughness (i.e., the ratio between roughness and pipe diameter) and is therefore more relevant in small diameter pipes. In large-scale pipelines, the effect of roughness on pressure drops is low due to the large diameter. Anyway, this parameter is investigated for the possible use of the materials in smaller pipelines or for the effects on other phenomena during production and operation of the pipe.

The standard ISO 21920-2 [96] distinguishes the primary profile, waviness profile and roughness profile, as regards the analysis of the texture of a surface. We are interested in the latter and it can be derived from the primary profile through the use of specific filters.

In particular, among all the different R-parameters (derived from the roughness profile, of which an overview is provided in Table 3.1, the one that is relevant to determine the friction factor is the arithmetic mean height R_a. As the name suggests, it is the arithmetic mean of the absolute values of the ordinate values. It is calculated as [96]:

$$R_a = \frac{1}{l_e}\int_0^{l_e} |z(x)|dx \tag{3.2}$$

where l_e is the evaluation length.

Table 3.1 - Overview of some roughness parameters [96], [97]

R-parameter	Description
Ra	**Arithmetic mean roughness** Arithmetic mean of the absolute values of the ordinate values
Rq	**Root mean square roughness** Square root of the mean square of the ordinate values
Rt	**Total height** Sum of the largest height and the largest depth
Rp	**Maximum profile peak height** distance between the highest point of the profile and the mean line
Rv	**Maximum profile valley depth** distance between the deepest valley of the profile and the mean line

The experimental procedure adopted for measuring the roughness of FRP samples is described in the next paragraphs. Results of the assessments will then be used in the fluid dynamics study of the pipe-in-pipe system presented in Chapter 7.

3.1. Roughness tests: methodology

Roughness measurements are performed for three different polymer composite materials with which pipes are manufactured: glass fibre-reinforced epoxy resin (GFRE), carbon fibre-reinforced epoxy resin (CFRE) and glass fibre-reinforced polypropylene (GFRPP).

The test specimens are obtained directly from previously manufactured tubes by cutting them out using an oscillating saw. Small test specimens are sufficient as the area to be tested is small: in this case, approximately square in shape and a couple of centimetres per side were obtained.

The abovementioned pipes have been manufactured by means of multi-filament winding (MFW) process described in Section 2.4. Measurements are performed using the VHX 6000 digital microscope from Keyence [98]. Such a microscope is capable of 3D mapping a defined area, thus enabling the topography of the sample surface to be obtained. Line profile measurements are subsequently performed in this area.

The principle behind the generation of the 3D panorama is the same as that for obtaining a focused image in its entirety even in the case of objects with a significant

variation in height: this is done by superimposing images at different focal planes. By recording the focal position data, the three-dimensional model can be reconstructed. This procedure is called 'depth from focus' (DFF). The tool is also able to exploit the opposite procedure, i.e. 'depth from defocus' (DFD), where the texture is determined on the basis of how much the different points are defocused.

In the area selected for the test, several line roughness measurements are carried out in both the X- and Y-directions, circumferential and longitudinal respectively, with an evaluated length of approximately 2 mm in both directions. The data initially obtained are relative to the primary profile. Therefore, it is necessary to use filters that take into account the cutoff value that needs to be removed to obtain the roughness profile. This is achieved by removing the long-wavelength component from the primary profile using a high-pass filter. Among the R-parameters, R_a is the one that will be used later in this work. Both the inner and outer surfaces of the various samples are analysed, because data may differ due to the production process and it will be of interest to consider the gas flow on both sides of the FRP tube in the pipe-in-pipe model.

3.2. Results and discussion

The areas where roughness measurements were taken, both on the inner and outer surface, are depicted in Figure 3.1, Figure 3.2, Figure 3.3.

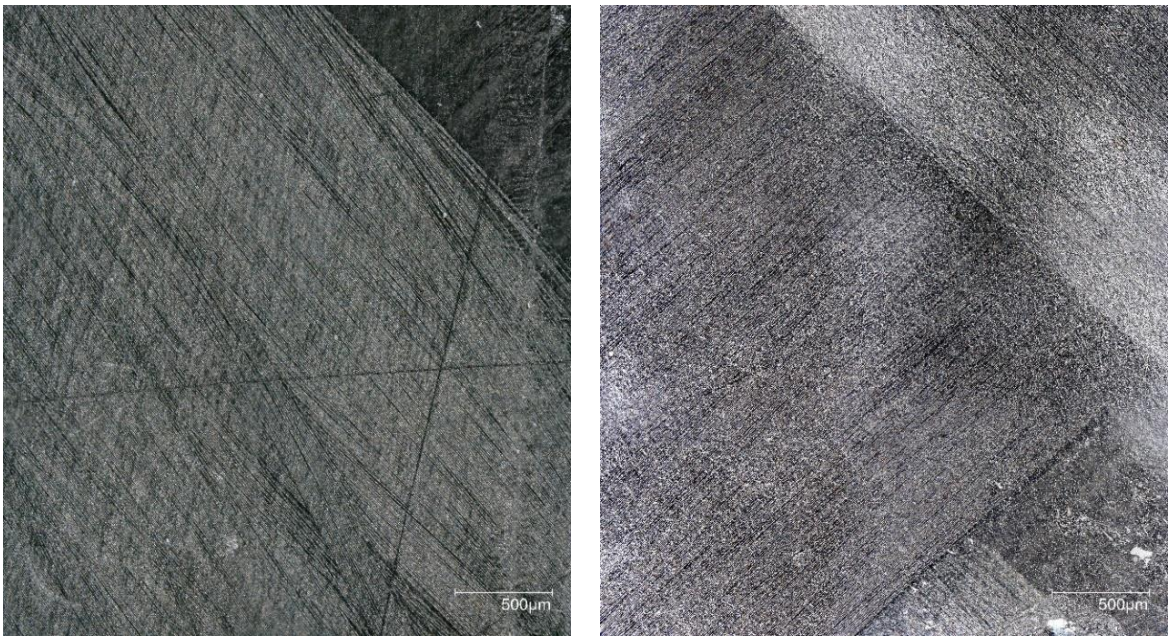

(a) (b)

Figure 3.1 – Internal (a) and external (b) test surface for CFRE

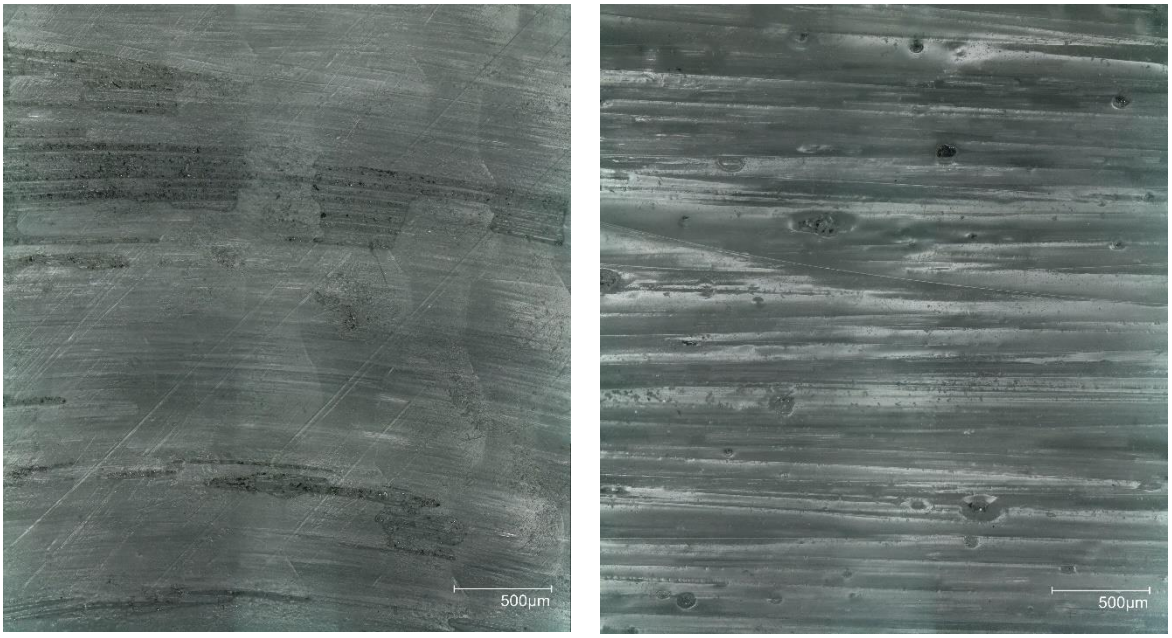

(a) (b)

Figure 3.2 – Internal (a) and external (b) test surface for GFRE

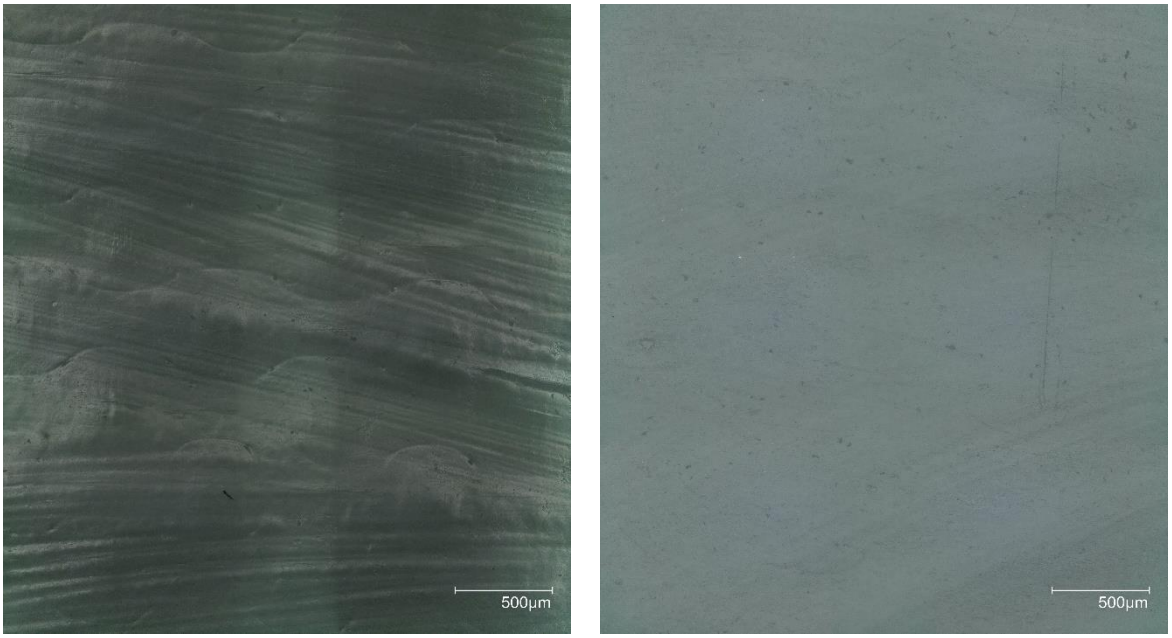

(a) (b)

Figure 3.3 – Internal (a) and external (b) test surface for GFRPP

The arithmetic mean roughness values of glass fibre-reinforced epoxy, glass fibre-reinforced polypropylene and carbon fibre-reinforced epoxy are shown in the

following tables. Specifically, Table 3.2 and Table 3.3 contain the outer surface values in the circumferential (X) and longitudinal direction (Y), respectively. Also their mean value and standard deviation are calculated.

Table 3.2 – R_a values for internal surface and circumferential direction

Ra [μm]	**Internal surface Direction: X (circumferential)**					**Average**	**Standard deviation**
# Meas.	**1**	**2**	**3**	**4**	**5**		
CFRE	0.36	0.36	0.31	0.27	0.57	0.374	0.10
GFRE	0.53	0.44	0.44	0.53	0.45	0.478	0.04
GFRPP	1.17	0.32	0.35	0.59	0.34	0.554	0.32

Table 3.3 – R_a values for internal surface and longitudinal direction

Ra [μm]	**Internal surface Direction: Y (length)**					**Average**	**Standard deviation**
# Meas.	**1**	**2**	**3**	**4**	**5**		
CFRE	0.31	0.33	0.31	0.28	0.49	0.344	0.07
GFRE	0.77	0.69	0.77	1.27	0.49	0.798	0.26
GFRPP	0.54	0.72	0.56	0.78	0.69	0.658	0.09

On the inner surface, whether in the circumferential or longitudinal direction, the CFRE sample has the lowest mean R_a and also the lowest standard deviation of all three materials. The other two samples show less consistency in the results: while in the X (circumferential) direction GFRE has a lower mean Ra and a better standard deviation than that of GFRPP, the opposite behaviour is observed in the Y (longitudinal) direction. In the X-direction, the mean R_a values for GFRE and GFRPP are 28% and 48% higher than the value for CFRE, respectively; in the Y-direction, both percentages increase to 132% and 91%, respectively. These considerations are clearly visible on the graph in Figure 3.4.

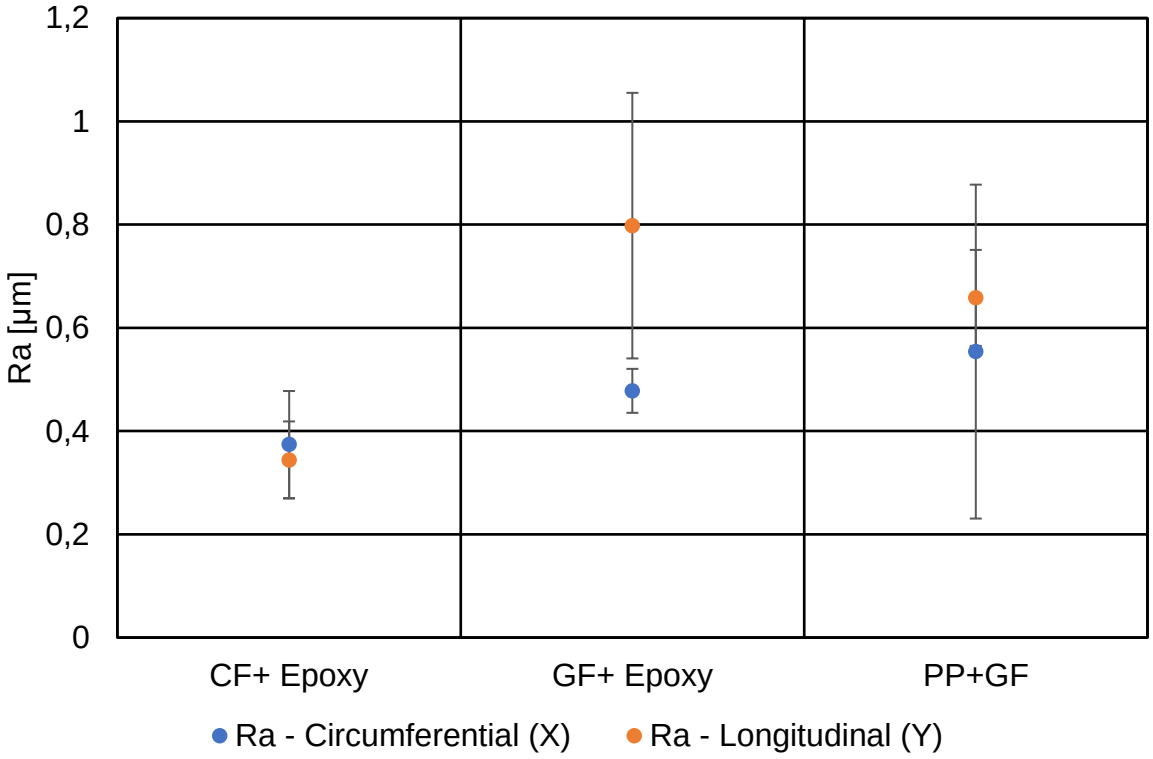

Figure 3.4 – Overview graph for Ra values of the internal surface

The results of R_a in the longitudinal and circumferential direction for the outer surface of the samples are reported in Table 3.4 and Table 3.5, together with their mean value and standard deviation.

Table 3.4 – R_a values for external surface and circumferential direction

Ra [µm]	**External surface Direction: X (circumferential)**					**Average**	**Standard deviation**
# Meas.	**1**	**2**	**3**	**4**	**5**		
CFRE	0.38	0.33	0.41	0.60	0,60	0.464	0.11
GFRE	0.51	1.49	0.69	0.55	1.22	0.892	0.39
GFRPP	0.41	0.36	0.49	0.37	0.34	0.394	0.05

Table 3.5 – R_a values for external surface and longitudinal direction

Ra [µm]	External surface Direction: Y (length)					Average	Standard deviation
# Meas.	1	2	3	4	5		
CFRE	0.26	0,41	0.48	0.51	0.49	0.430	0.09
GFRE	3.21	2.95	2.34	2.49	2.12	2.622	0.40
GFRPP	0.83	0.79	0.91	0.87	0.91	0.862	0.05

Both the CFRE and GFRPP samples show a low mean R_a and an equally low standard deviation, which are both desirable conditions. On the other hand, larger values are obtained for the GFRE sample , in both cases. Particularly remarkable is the growth of the average R_a in the longitudinal direction compared to the other two materials: it is 510% higher than in CFRE and 204% higher than in GFRPP. In the circumferential direction those percentages are 92% and 126% respectively. A graphical overview of the values is provided in Figure 3.5.

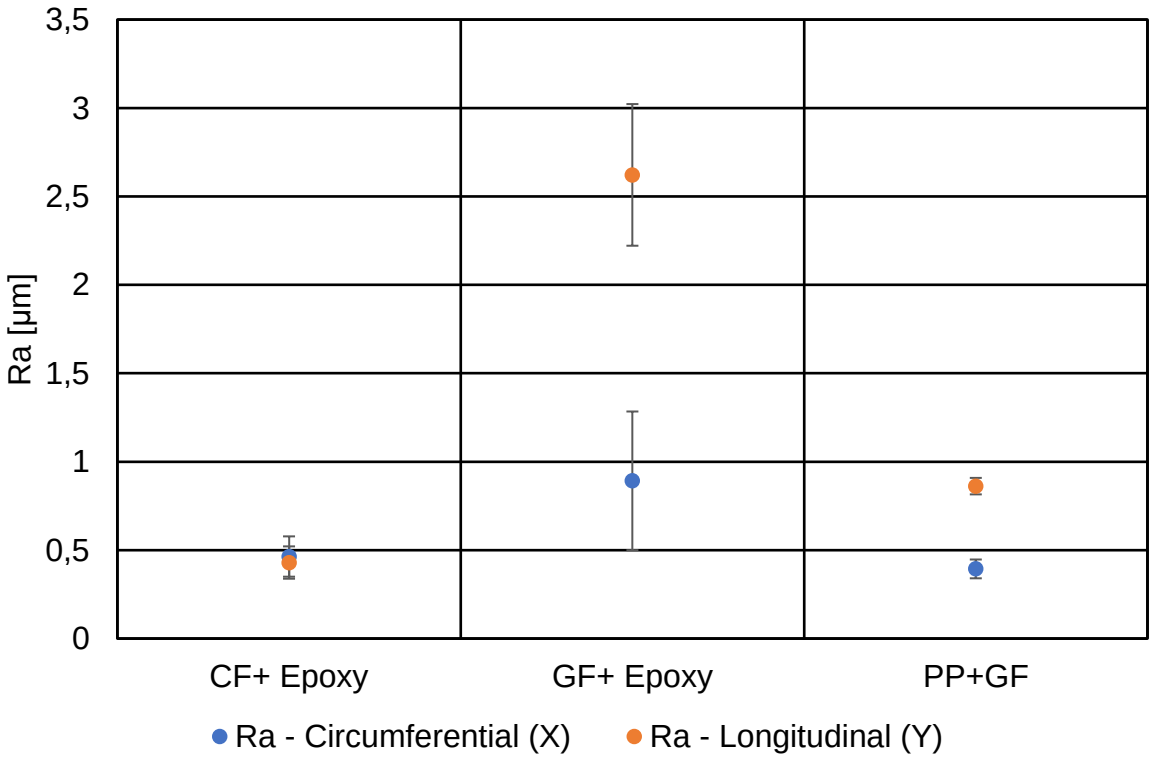

Figure 3.5 – Overview graph for Ra values of the external surface

In the following calculations, the average of the R_a values in the circumferential and longitudinal direction was taken as the surface roughness, distinguishing between the inner and outer surface. All measurements in the previous tables are taken into account as no outliers are shown by means of the interquartile range (IQR) criterion.

These values are shown in Table 3.6.

Table 3.6 – FRP roughness values used in calculations

	Internal surface	**External surface**
ε_{CFRE} **[μm]**	0.359	0.447
ε_{GFRE} **[μm]**	0.638	1.757
ε_{GFRPP} **[μm]**	0.606	0.628

Considering that commercial steel [99] and pure epoxy resin [100] specimens have roughness values of 46 μm and 0.1 μm, respectively, it is evident that the analysed samples are smoother than a metallic material but rougher than the pure matrix without fibres. It is important to keep in mind that the production process significantly influences the roughness value, but this comparison can still provide a greater awareness of the typical ranges of surface roughness for different materials.

The internal and external roughness of the tube made with MFW is influenced by different factors.

The outer surface of the mandrel is in direct contact with the inner surface of the tube and therefore it is desirable that it is as smooth as possible. Its coefficient of thermal expansion α_T must be high, so as to press against the inside of the tube and achieve greater consolidation and a smoother surface. Various materials are available, both metallic (e.g. aluminium and steel) and polymeric (e.g. polypropylene), as long as they can withstand the temperatures reached in the autoclave.

The surface finish of the outer wall of the artefact, on the other hand, is definitely affected by the winding tension and the cover factor, i.e. the ratio of the area covered by a single layer of yarns to the area of the underlying mandrel. The cover factor must be 100% in order to avoid multiple layers of towpregs to generate a grid-like structure. This can be achieved by optimising the combination of the horizontal and rotational speed of the mandrel, which also has an effect on the inclination of the fibres affecting the difference in roughness in the circumferential and longitudinal direction.

In addition, the application of a shrinking tape surely contributes to the external surface roughness by compressing the tube during the thermal cycle inside the autoclave.

4 Permeation test

Permeability is the degree of permeate transmission through a resisting material [101]. The mechanism of gas permeation through a solid material consists of the following fundamental physical processes: adsorption and absorption, diffusion and desorption [102]. In compact materials, diffusion is the time-determining process [103].

The driving force behind diffusion is a concentration gradient and the flow of matter occurs to reduce the difference in concentration. Fick's first law correlates the flux of a material, i.e., the mass m (or equivalently the number of moles) flowing per unit area A and unit time τ, and the concentration gradient $\frac{\partial c}{\partial x}$ in the flow direction, with a linear dependence between the two. The proportionality constant is the diffusion coefficient D of the material.

$$J = \frac{m}{A\,\tau} \tag{4.1}$$

$$J = -D\left(\frac{\partial c}{\partial x}\right) \tag{4.2}$$

The negative sign in equation (4.2) indicates that flow occurs in the opposite direction to the gradient.

Fick's first law is particularly useful to investigate a steady-state flow situation, where the concentration of the diffusing species does not vary in time but only in space [104]. This hypothesis is adopted in the coming chapters, as these conditions are similar to those to which pipelines are subjected, in which the concentrations of the diffusing species are kept constant on both sides of the wall, or at least their variations have very slow time constants.

In stationary state, the flux is constant at any position inside the barrier (see Figure 4.1) and equation (4.2) can be expressed in this way:

$$J = D\,\frac{\Delta c}{d} \tag{4.3}$$

where d is the thickness of the barrier itself.

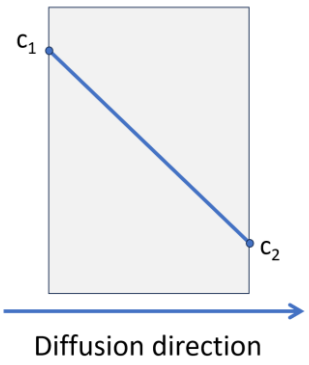

Figure 4.1 – Schematic representation of steady state diffusion mechanism

Permeability is defined as the product of the diffusion coefficient D and the solubility coefficient S that relates the concentration of a gas at the barrier's surface and its partial pressure [104], [105]:

$$P = D\,S \tag{4.4}$$

4.1. Permeation measurements

Two methods for measuring gas permeation through solids are briefly discussed below. The first is a manometric test, which therefore has pressure as the basis of its operation, and the second is an electrochemical method.

The manometric method is applied to plastic films and sheets and relies on the ISO 15105 standard, which is divided into two parts, each dedicated to a different procedure setup. However, the core of the setup is the same: two pressure chambers separated by the specimen under examination.

In the first part [106], the variant of the test utilizing differential pressure is analysed. Both chambers are initially evacuated, and then gas is introduced into the high-pressure chamber. The gas permeates towards the low-pressure chamber until the partial pressure in both becomes equal. From the measured pressure profiles and volumes of the chambers, the flow rate of the gas through the material can be estimated. The second part of the standard [107] is dedicated to the equal pressure method, where one of the two chambers is swept with a carrier gas, while the other is fed with the test gas. The total pressure is the same and equal to atmospheric pressure in both chambers, but the partial pressure of the test gas is higher in the second chamber. Consequently, the test gas permeates into the carrier gas through the sample, which acts as a barrier. A sensor is employed to measure the quantity of test gas that permeates and is carried out of the cell by the carrier gas. The sensor generates a current proportional to the amount of gas permeating per unit of time. An alternative

version of this method involves the use of a gas chromatograph for determining the gas transmission rate.

The electrochemical method is discussed in more detail below, as it is the one that has been employed, following several adaptations, to study hydrogen permeation through FRP materials. This approach is selected due to the absence of specific standards for FRP and constitutes a novelty aspect introduced in this work.

4.1.1. Electrochemical method

The electrochemical measurement of hydrogen permeation is based on the principle that for each hydrogen atom that diffuses through the metallic sample and is oxidized to a hydrogen cation on its surface, an electron is introduced into the external circuit. Therefore, it is possible to correlate the measured current with the flow of hydrogen atoms through the sample.

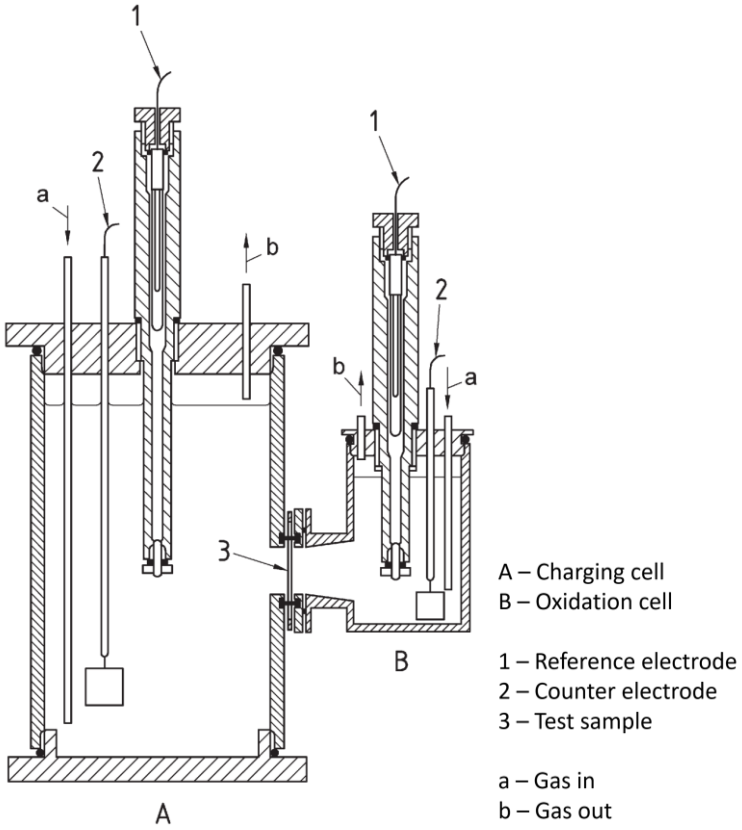

Figure 4.2 - Hydrogen permeation cell for electrochemical method [108]

ISO 17081 [108] deals with the description of a method for measuring hydrogen permeation in metals, as well as the quantification of its uptake and transport, using an electrochemical method.

The experimental apparatus consists of two different compartments, a charging cell and an oxidation cell, between which the metal sample to be tested is placed.

A three-electrode system is provided in both cells: the working electrode (WE), which in both partitions is the metal sample, the counter electrode (CE) and the reference electrode (RE) [109]. The counter electrode is typically platinum Pt, while saturated calomel electrode (SCE) or silver/silver chloride (Ag/AgCl) is suggested as the reference electrode, bearing in mind that the former is banned in some countries due to environmental issues. The three electrodes are connected to potentiostats in order to keep the voltage at the desired values.

The charging cell is filled with an electrolyte and the electrochemical reactions leading to the formation of hydrogen take place in it. For the construction of the cells, it is suggested that metallic materials be avoided, and a possible candidate is polytetrafluoroethylene (PTFE), which is suitable for temperatures of up to 90°C.

In aqueous environments, hydrogen atoms are produced on the surface of the workpiece by electrochemical reactions. Equations (4.5) and (4.6) are valid in acidic and alkaline environments respectively [110]:

$$H^+_{(aq)} + e^- \rightarrow H_{(ad)} \tag{4.5}$$

$$H_2O + e^- \rightarrow H_{(ad)} + OH^- \tag{4.6}$$

The adsorbed hydrogen atoms on the surface of the metal diffuse through it in atomic form. The hydrogen atoms on the other side of the sample, exposed to the oxidation cell where it works as anode, are oxidised and escape as hydrogen cations.

$$H \rightarrow H^+ + e^- \tag{4.7}$$

It is necessary that the background current existing prior to hydrogen permeation is small and stationary compared to that generated by the oxidation of the hydrogen atoms. Therefore, both the electrode potential and the working environment in the oxidation cell must be such that the metal is in a passive condition or even immune to corrosion.

The standard goes on to emphasise that it is important to ensure that the oxidation of the hydrogen atoms is limited by transport and therefore the electrode potential in the oxidation cell must be kept at a sufficiently high value (the addition of a palladium coating on the surface of the sample facing that compartment can increase the oxidation rate).

As far as the constraints on the samples are concerned, these must be in the form of a plate or pipe in order to be tested and the dimensions must be such as to favour unidirectional flow.

The flow of electrons is proportional to the flow of hydrogen, so it is possible to derive the flow of hydrogen atoms from the permeation current, obtained by subtracting the passivation current from the total measured current.

$$J = \frac{I_{perm}/A}{F} \tag{4.8}$$

where A is the tested area of the sample and F is the Faraday constant (96485 C/mol).

4.2. Hydrogen permeation measurement in FRP through electrochemical method

The method for testing and measuring the permeation of hydrogen through polymeric composite materials used in this work is a revisitation of the electrochemical method described in the previous Section (ISO 17081 [108]), being less expensive and requiring less attention in terms of safety considerations than the manometric method. The underlying equipment consists of the Automated Measurement and Control Box (AMB) from the company iChemAnalytics GmbH [111] and the ElyFlow test cell from Gaskatel [112] (see Figure 4.3).

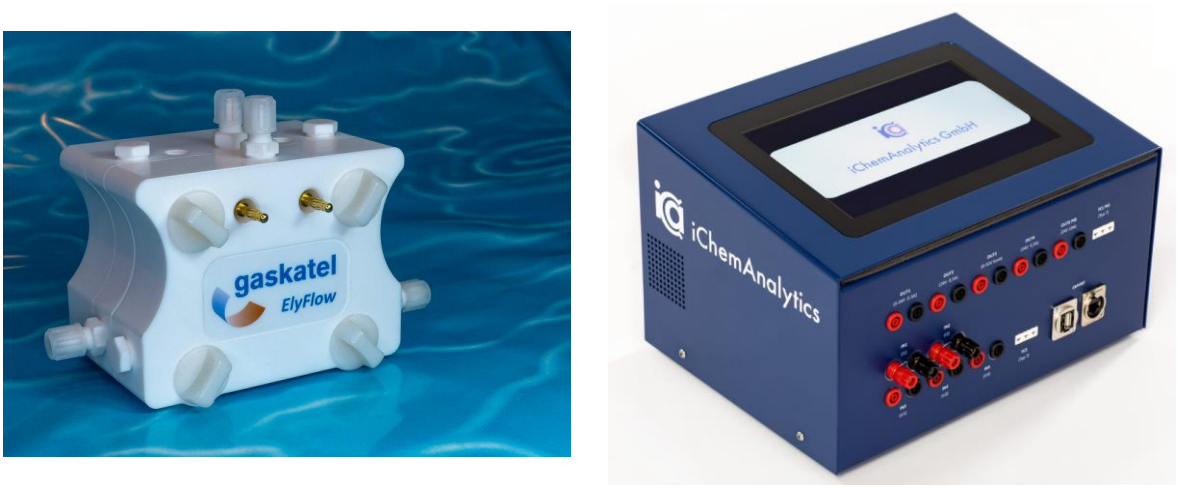

Figure 4.3 - ElyFlow test cell (left) and AMB (right)

Thanks to the assistance and experience provided by the company iChemAnalytics GmbH, an attempt was made to exploit the method in patent [110]. The subject matter of this patent relates to the measurement of hydrogen permeation through metallic or metallised workpieces and the main advantage over the method in ISO 17081 is the lower complexity of the instrumentation.

4.2.1. Experimental equipment and procedure

The following procedure refers to the use of a metallic sample. The modifications that need to be made when dealing with an FRP sample will be specified later.

The equipment include two components: AMB, dedicate to electric signals analysis, and ElyFlow, that is the actual electrochemical cell.

The AMB enables high-resolution measurements and control tasks by exploiting the five voltage inputs, two temperature inputs and five parameterisable outputs that are made available. All inputs and outputs can be viewed in real time (with a maximum sampling rate of 1 acquisition each 2 seconds) and data records can be made, which can then be conveniently exported to Microsoft Excel or as screenshots.

ElyFlow, on the other hand, is the actual test tool. It is made of PTFE, as opposed to many other cells based on the Devanathan-Stachurski cell that is made of glass, which, however, is a more fragile material and can have chemical stability problems with aggressive solutions, such as alkalis. ElyFlow consists of two compartments separated by the sample that takes part in both: there is a loading cell (in which the electrolysis of water takes place) and a measuring cell (or oxidation cell). The former comprises a compartment for the counter-electrode (two options are provided: Ti-MMO or nickel) and one for the electrolyte, that is also present in the measuring cell together with a gas diffusion electrode GDE-compartment. Oxygen arrives directly to the GDE from the outside via channels communicating with the outside within the corresponding compartment.

The first step is to arrange the sample as a separation between the two cells, making sure that the O-rings in EPDM (ethylene-propylene diene monomer) of the two analyte chambers are tightly adhered to it. The area of the sample exposed to the electrolyte on both sides is 10 cm^2. Next, the analyte compartment of the oxidation cell, whose capacity is 25 mL, is filled, while the loading cell is kept empty. It is important to ensure that all the holes in the analyte chamber are closed. A 0.5 M (molar) solution of sodium bicarbonate ($NaHCO_3$) is used as the electrolyte for both cells.

Bearing in mind that this set-up is designed for metal specimens, the apparatus is left under these conditions for several hours, allowing the passivation reaction of the sample surface exposed to this environment to take place. The aim is to obtain a low value of current that is as constant as possible over time. The formation of this passive layer seeks to prevent the workpiece from taking part in the redox reaction occurring in the measuring cell. In the case of materials that do not form such a layer, a palladium coating can be applied to the surface facing that compartment.

Once the current has stabilised, the electrolyte chamber of the loading cell is filled with the same electrolyte as before, which works as the source of water necessary for hydrogen production. A pump and an external container in which the electrolyte is placed are used so that electrolyte is continuously circulated in this compartment and

excess hydrogen is carried away. The pump used is the NF1.10 diaphragm liquid pump by KNF [113].

An overview of the main components of ElyFlow, once assembled, is shown in Figure 4.4.

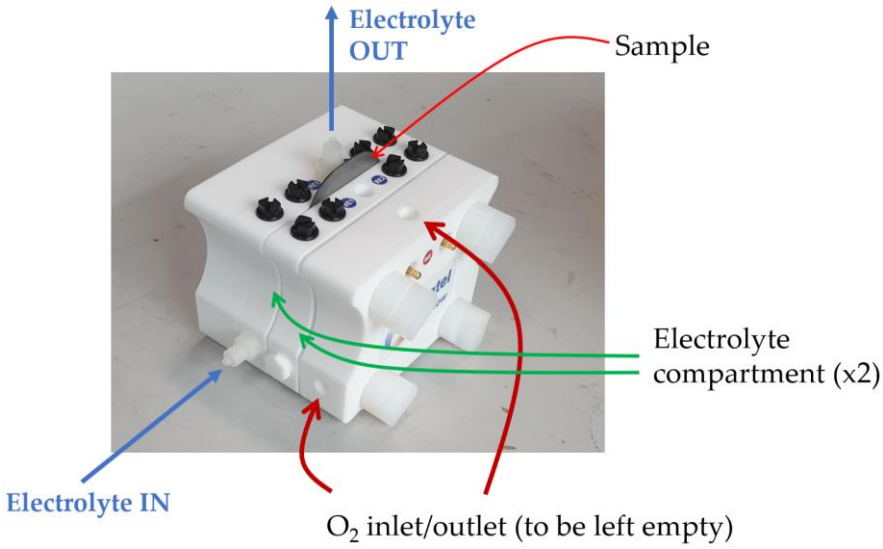

Figure 4.4 - ElyFlow cell overview

In the “Output”' section of the AMB box, a potential of 3 V is set at the loading cell, which is required for the electrochemical water splitting reaction to take place, and a potential of 0-10 V at the pump. The "Input" section, on the other hand, records the electrolysis current and oxidation current.

Data recording is continued until a steady current is reached. Usually a time of 30-40 minutes is sufficient. The measured values will be essential for the quantification of hydrogen permeation through the sample.

Figure 4.5 shows the whole equipment ready for use.

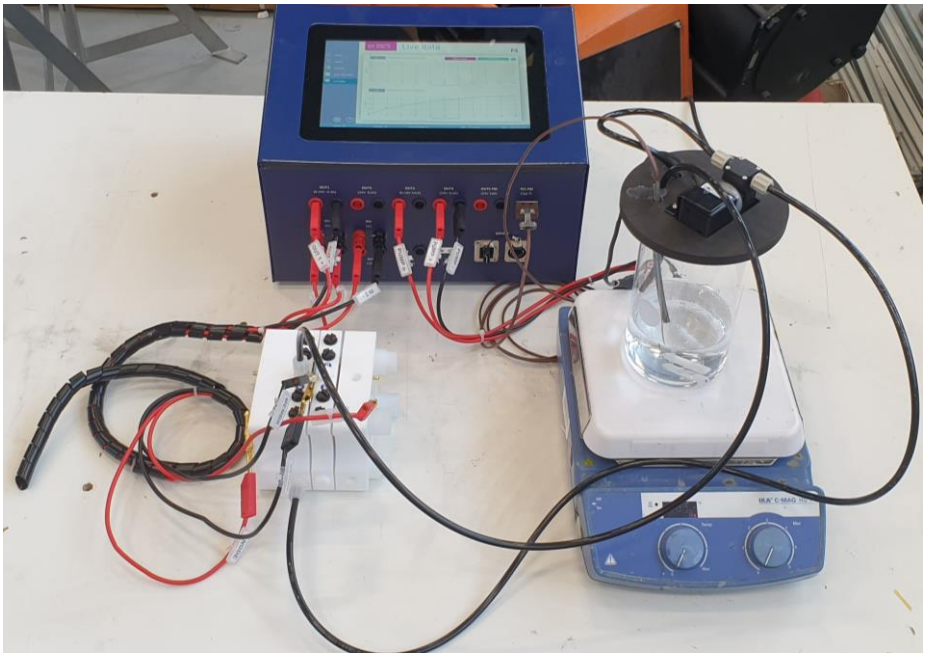

Figure 4.5 - Hydrogen permeation test equipment setup

The underlying theoretical basis is no different from that explained in the previous Section with reference to standard. Hydrogen is produced on the surface of the sample facing the loading cell by electrochemical water splitting. Since the system operates in an alkaline environment, the reference reaction is [110]:

$$H_2O + e^- \rightarrow H_{(ad)} + OH^- \tag{4.9}$$

After being adsorbed on the surface of the sample, hydrogen diffuses within it in monoatomic form, trying to balance the concentration gradient, and reaches the opposite face, the one exposed to the electrolyte in the measuring cell. Here, the oxidation of the hydrogen atoms to protons takes place.

$$H \rightarrow H^+ + e^- \tag{4.10}$$

The operating principle of the oxidation cell is practically the same as that of a fuel cell and therefore an external current source is not required: the second surface of the workpiece acts as an anode and the oxygen electrode acts as a cathode where oxygen reduction occurs.

Free electrons flow into an electrical conductor that is connected at the other end to the GDE, generating a current, while hydrogen cations diffuse inside the electrolyte.

The gas diffusion electrode consists of a current collector and a catalyst layer (that is the actual electrode): the former is a nickel mesh, while the latter consists of manganese dioxide (MnO_2). It must provide the largest possible three-phase interface between

oxygen, electrolyte and electrode material (in order for electrons to take part to the reaction). A porous support is therefore used.

The reduction of oxygen (see equation (4.11)) provides the driving force for the hydrogen oxidation reaction (HOR) [110].

$$O_2 + 2H_2O + 4e^- \rightarrow 4OH^- \tag{4.11}$$

The last steps to be performed, in short, are to measure the current circulating in the electrical conductor and determine the amount of hydrogen diffused on the basis of the charge flowed. The flow of electrons is determined through the AMB box amperometrically. That current is the total current I_{tot}, namely the sum of permeation and passivation currents, I_{perm} and I_p respectively, but the former is the only one required for calculations. It is therefore necessary to subtract the background current from the total measured current:

$$I_{perm} = I_{tot} - I_p \tag{4.12}$$

Since for every hydrogen atom oxidized, one electron enters the circuit, it's possible to express the flow of electrons $\dot{n}_e$ as the flow of hydrogen atoms $\dot{n}_H$ permeating through the tested area of the sample A.

The flow of hydrogen atoms in terms of permeation current is therefore:

$$J_H = \frac{\dot{n}_H}{A} = \frac{\dot{n}_e}{A} = \frac{I_{perm}/A}{F} \tag{4.13}$$

To find the diffusion coefficient D of the material, three different approaches can be used [114].

The first involves calculating the diffusion coefficient from the breakthrough time t_b, recognized as the time required for the first hydrogen atom to completely permeate through the sample, where the permeation current I_{perm} is 10% of the steady-state current I_{SS} [114]. The formula is:

$$D = \frac{d^2}{15.3\ t_b} \tag{4.14}$$

where d is the thickness of the tested sample.

The lag time method, on the other hand, incorporates the time t_{lag} into the calculation, during which I_{perm} reaches 63% of I_{SS} [114]:

$$D = \frac{d^2}{6\ t_{lag}} \tag{4.15}$$

Finally, it's possible to fit the entire permeation transient to an approximate solution of Fick's second law, which is indeed valid for non-steady-state conditions, obtained from either a Laplace or Fourier transform.

A graphical representation of the three thresholds used in the presented methods is shown in Figure 4.6.

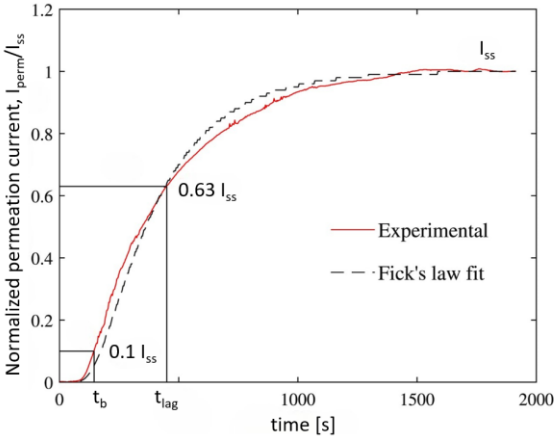

Figure 4.6 - Representative permeation transient and visual representation of the thresholds for diffusion coefficient calculation [114]

4.2.2. Sample requirements and adaptations

The geometry of the sample is very important because it affects the results and must be suitable for the test apparatus.

The patent [110] refers in particular to the fact that the sample should preferably be planar and with a maximum thickness of 5 mm, specifying however that thicknesses below 1 mm (even better below 0.5 mm) are the best option. This is to ensure one-dimensional hydrogen diffusion and better detection sensitivity. At the same time, the requirements of the ElyFlow test cell, which allows samples with widths between 52 mm and 62 mm and heights above 95 mm, must be met.

Since the objective of this study is the measurement of hydrogen permeation through FRP materials and, therefore, the samples to be tested are non-metallic, adaptations must be made to the samples themselves so that the same equipment can continue to be used.

The main complication is that the FRP samples are not electrically conductive and consequently neither electrochemical reactions, in the loading and measuring cell, can take place. The path taken is to coat them with a metal layer.

Palladium is an excellent candidate for metallising the sample, as it is able to catalyse the hydrogen oxidation reaction. In fact, the ISO 17081 standard mentions the

possibility of adding a palladium coating to the side of the sample facing the oxidation cell to ensure that HOR is transport limited [108].

The Sabatier principle, proposed in 1913 by the scientist of the same name, which was based on empirical observations, provided a conceptual framework for the search for a high-performance catalyst [115]. It provides an intuitive explanation of numerous experimental results, but its predictive power is limited in certain situations [116], [117].

The basic idea is that the binding energy with the reaction intermediate must be neither too high nor too low for an optimum catalyst. This leads to a relationship between free energy of adsorption and reaction speed that takes the form of a volcano, as shown in Figure 4.7. If the deviation from thermoneutral adsorption is in the form of a too weak binding, the catalyst barely interacts with the reactant and this limits the overall rate; if, on the other hand, the binding strength is too high, desorption is negatively affected [116], [117].

To describe the degree of catalytic performance, it is widely accepted to use the exchange current density, which is proportional to the HOR reaction rate at the equilibrium potential [118].

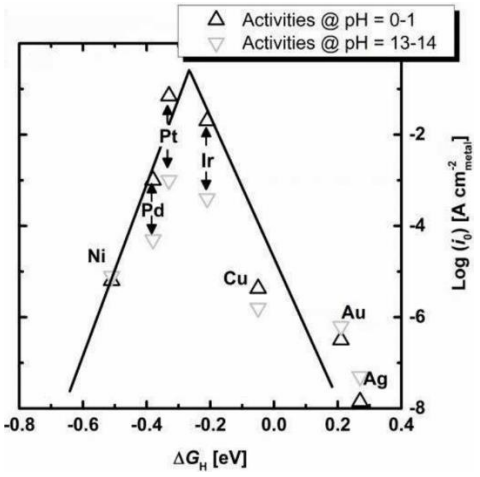

Figure 4.7 - H_2 adsorption energy as a function of HOR exchange current density [119]

Although platinum (Pt) and iridium (Ir) have superior catalytic properties for the HOR reaction, palladium (Pd) is here preferred thanks to the lower price and larger availability of the material. Indeed, both the high cost and limited world supply of Pt make Pd an attractive alternative, due to its chemical similarity, four times lower cost and 50 times higher abundance [120], [121].

Overall, the aim of these modifications would be to expand the scope of applicability of the test method to more materials, while ensuring that permeation behaviour is

affected as little as possible. However, the presence of the palladium coating may not have a negligible influence.

Further research must be done regarding the effect that palladium coating has on permeation measurements in FRP materials, especially at the level of hydrogen absorption within the sample. Indeed, the permeation of hydrogen in metals is only possible in atomic form, whereas in the case of polymeric materials, the dissociation of the hydrogen molecule is not necessary. The possibility of hydrogen atoms recombination into hydrogen molecules inside the FRP sample needs to be evaluated.

4.2.3. FRP test sample production

This section is devoted to the description of the manufacturing process of FRP samples, both GFRP and CFRP, which will then be subjected to hydrogen permeation tests.

The process is divided into numerous steps. It starts with the production of plates made from heat-treated prepregs, followed by the cutting of samples from them and finally their preparation for the permeation tests.

A Section is devoted to each of these steps.

4.2.3.1. FRP plates production

The aim of this section is to obtain FRP plates from rectangular-shaped prepregs by thermal cycling.

The prepregs are made from carbon and glass fibres that are pre-impregnated with epoxy resin and kept in a cooler to prevent the curing reaction from starting.

The first step is to take a slab of safety tempered glass (ordinary glass would not work because it would shatter during the heat treatment that will need to be carried out at the end) and clean it thoroughly to remove any residue of glue, tape or resin that may have been left over from previous processes.

The next step is the application of sealant tape, which can withstand high temperatures of up to 180°C. It is applied to all four sides of the rectangular pane, ensuring that no gaps are left where the different strips of tape intersect: this is necessary because the following step involves applying three layers of a solution of releasing agent with an impregnated cloth that must be prevented from getting into even the smallest gaps left by the sealant tape. In the event that this happens, it would not be possible to apply the vacuum. Its role, as the name suggests, is precisely to prevent the prepregs that we now place on the glass from sticking to it, making it extremely difficult, if not impossible, to remove them, at least without severely damaging them.

The prepregs that are used in this work are rectangular in shape, either with carbon fibres (CF) or with glass fibres (GF), arranged in both cases unidirectionally and impregnated with epoxy resin. In particular we used two made with glass fibres, made of 6 and 9 layers of fibres, and two with carbon fibres, again of 6 and 9 layers, and they

are subject together to the same procedure two by two, depending on the number of layers. Therefore, the following steps refer to two prepregs, one with GF and one with CF, having the same number of layers, either 6 or 9.

Before they can be placed on the glass plate, the prepregs are stored in a freezer while awaiting their use, in order to keep them at a low temperature, below 0 °C, preventing the resin curing reaction, which would already take place at room temperature, from starting and increasing their shelf life.

Prepregs are removed from the freezer and, after waiting for approximately 30 minutes for them to warm-up while being wrapped in plastic, so that the condensation of air humidity does not interfere, they are placed in position on the glass plate, taking great care that neither one bends or splits so as not to compromise the permeation measurements, which would certainly be affected by this type of heterogeneity.

Then both prepregs are covered first with peel ply and then breather fabric, without these ending up on top of the sealant tape. The former consists of a fabric made of polyamide (PA) and allows easy separation of the breather fabric from the FRP plates, while the latter serves to absorb the excess epoxy resin in which the fibres are immersed, which would otherwise risk being sucked up by the vacuum pump when it is put into action, while providing an air path to the vacuum connector. The breather fabric is also used to make a sort of pedestal for the suction end of the tube attached to the vacuum pump, by folding a couple of times a strip of it.

Finally, the vacuum foil, which is capable of withstanding temperatures of up to 180°C, is placed on top of the breather fabric, making it stick to the sealing tape.

However, some care must be taken. Four spikes must be made with the sealant tape on top of the previously laid tape strips, one on each side, in a precise configuration. It is crucial to ensure that these spikes are arranged so that the lines connecting the two spikes on opposite sides form a cross, the intersection of whose arms coincides with the end of the suction tube. By doing so, the vacuum foil, tightly adhered to the modified profile of the sealant tape, avoids being overstretched in the area of the suction point and this prevents it from tearing.

As far as pressure is concerned, since we want to work in vacuum, our goal is to achieve -1 bar with respect to atmospheric pressure (as indicated on the pressure gauge). Once this pressure value is reached, everything is ready and the prepregs, together with all the rest of the equipment (see Figure 4.8), can be placed in an autoclave where they will be subjected to a thermal cycle.

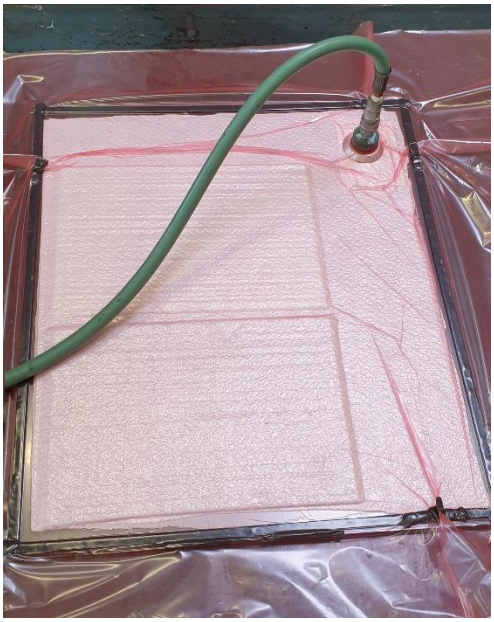

Figure 4.8 - Plates after vacuum creation

The cycle starts at 25°C, then the temperature is raised to 80°C within thirty minutes and held there for another half hour. Then it is raised again to 130°C in thirty minutes, held for two hours. The complete cycle lasts five to six hours, considering also the need to cool everything down to room temperature in a controlled manner.

Figure 4.9 shows the two plates made of epoxy resin and carbon/glass fibres obtained downstream of the entire process.

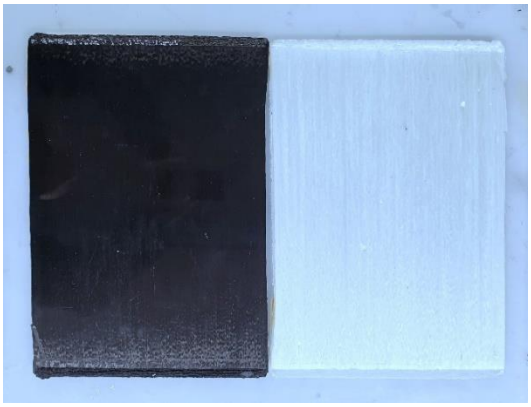

Figure 4.9 – Final result of CFRE (left) and GFRE (right) plates

4.2.3.2. FRP sample production

The next step is to cut the plates so that at least two of the four sides are perfectly perpendicular. This will allow for perfect alignment inside the waterjet machine that will soon be used to cut out the samples.

To do this, a sawing machine, such as MAIKO K 680 S [122], can be used to cut one straight side at a time. It has a cutting length up to 690 mm and rotary frequency of the saw blade tunable between 2000 and 6000 rpm. The maximum material thickness it can handle is 8 mm. In this work, it is decided to make the cut parallel to the direction of the fibres, just to have the same alignment of the fibres for all the samples (the fibre alignment in the plane should not affect the permeation measurements anyway).

It is now possible to place the plate accurately inside the waterjet machine. To carry out this step, the ProtoMAX waterjet machine by OMAX [123] was used.

Figure 4.10 – ProtoMAX waterjet machine by OMAX [123]

The jet is fired with a pressure of 2000 bar by a 5HP (3.7 kW) pump and exits a nozzle that is moved above the plate to be cut, which must have a maximum allowed thickness of 25 mm. The translation speed can reach values up to 100 in/min (2,540 mm/min) with ±0.005 in (±0.127 mm) linear positional accuracy[123]. The path of the plate is determined in advance by a computer programme depending on the shape of the specimens to be obtained (see Figure 4.11).

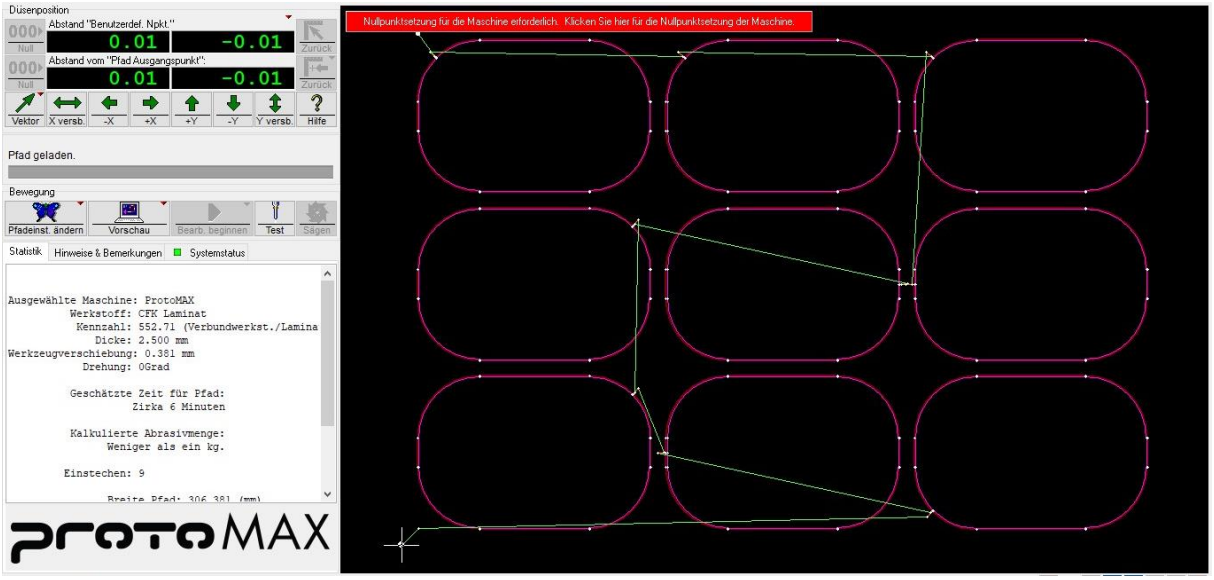

Figure 4.11 - Path of the water jet set on the computer program

In this analysis, 9 identical test specimens for each plate are obtained: 18 with glass fibre, of which 9 with 6 layers of fibre and 9 with 9 layers, and as many with carbon fibre.

The dimensions of the sample are those shown in Figure 4.12.

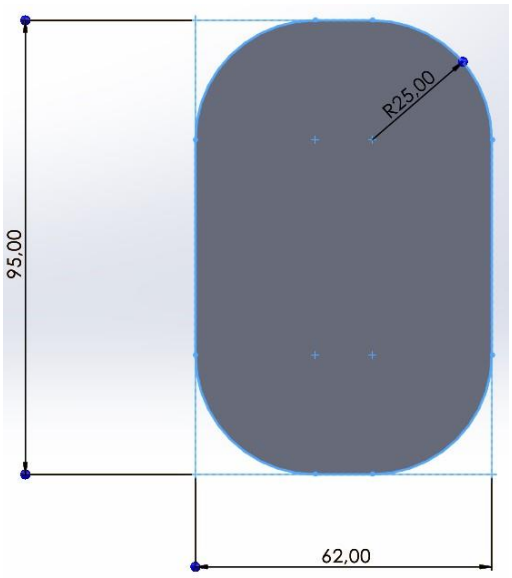

Figure 4.12 - Dimensions of sample front in millimeters

The thickness varies depending on the material and especially the number of layers it consists of. The thickness of a specimen for each type is shown in Table 4.1 to get an idea of typical reference values.

Table 4.1 - Measured thickness of FRP samples

	Thickness, 6 Layers [mm]	**Thickness, 9 Layers [mm]**
CFRE	2.30	3.46
GFRE	2.32	3.33

Once the body of the sample is obtained, the perimeter faces generated by the cutting action must be coated with epoxy resin. The choice fell on the so-called 5-minute epoxy and its appropriate hardener. The mixing ratio between the two must be 1:1 and the quantities involved must be adequate in order to avoid excessive generated heat. According to the information on the label, the processing time is 3-5 minutes and this is to be interpreted as the limit for the application of the resin, after which it is no longer possible to apply the resin as it has now hardened, and after 10 minutes it is possible to apply loads.

A small amount of resin is put close (but not in contact) to a small amount of hardener, forming drops that had approximately the size of a €1 coin. From experience it is preferable not to exceed 100 mL of both the resin and the hardener, otherwise, a very intense heat would be released when the two are mixed.

The final step involves the fast mixing of the two drops with a wooden stick or brush and the immediate application of the mixture along the boundary of the samples, trying to make the most of the 5 minutes available, treating as many samples as possible, as a matter of efficiency. The final results are shown in Figure 4.13.

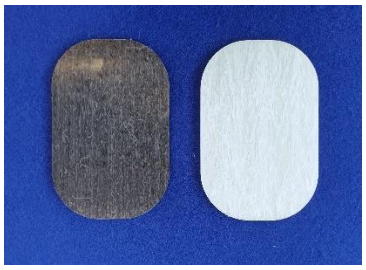

Figure 4.13 - CFRE (left) and GFRE (right) samples before palladium coating

4.2.3.3. Palladium coating

The FRP samples need to be coated with palladium, as discussed in Section 4.2.2, so as to make their surface conductive, otherwise it would not be possible to perform permeation measurements through an electrochemical method. The covering is

performed via sputtering deposition of one sample at a time, using the machine in Figure 4.14.

Figure 4.14 - Sputtering machine used for palladium coating deposition

Prior to palladium sputtering, however, it is necessary to sand the surface of the samples in order to achieve uniform coverage and to even out the surface by reducing possible surface hydrogen traps. The AutoMet 250 Grinder Polisher machine by Buehler [124] allows to have a small water jet on the rotating disk, so as to capture the powder that is released from the sample surface, that would otherwise be volatile and could be easily inhaled by the operator (that necessarily needs to work close to the machine itself). Abrasive discs P80 (coarser) and P320 (finer) were employed, corresponding to a grit size of 201 μm and 46.2±1.5 μm respectively [125].

Both the palladium target and the sample are then placed in their dedicated position inside the sputtering chamber, which is then closed, and the vacuum pump is activated. Once the pressure has reached 0.06 torr, argon is made to flow inside for about 15 seconds by opening the dosing valve.

At this point, the process pressure is set to 0.1 torr, after which the sputtering current is set to 20 mA. The samples are subjected to the sputtering process for about two minutes, so that a sufficiently homogenous palladium coverage is achieved without damaging the sample surface with the developed heat. At the end of this procedure, sputtering is stopped, the argon valve is shut and the chamber is vented. At this point, the sample can be removed.

As only one of the two faces of the sample is exposed to the palladium target, the process is repeated in the same way after exposing the other face to the target. This makes both surfaces electrically conductive, as the sample has to work as a cathode in the charging cell and as an anode in the oxidation cell.

4.2.4. Results and discussion

Below are the results obtained by following the procedure described in Section 4.2.1, in accordance with the patent [110].

When the oxidation cell is filled with the 0.5 M $NaHCO_3$ solution, the passivation reaction of the metallised surface of the sample begins. A current must therefore be expected to flow through the conductor cable and be measured by the AMB box.

Looking at the Pourbaix diagram of palladium in Figure 4.15, which shows the theoretical domains of corrosion, passivation and immunity as a function of pH, one can see that it is a very noble metal. Its thermodynamic stability domain is very extensive and covers almost the entire pH range and is only dissolved by strongly acidic and oxidising solutions.

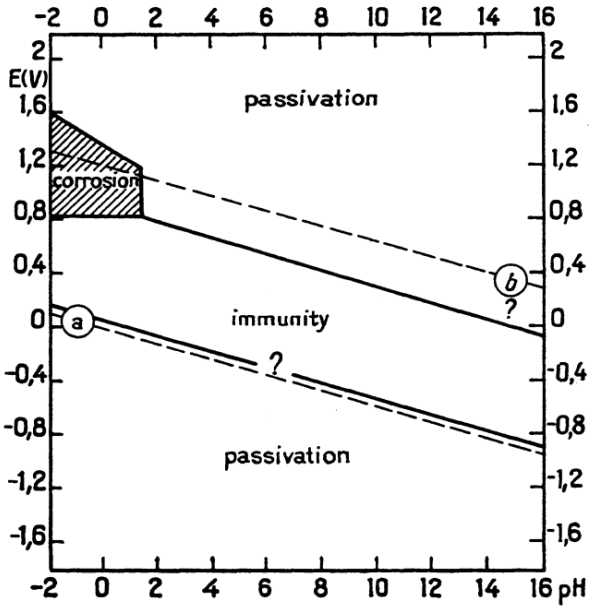

Figure 4.15 - Pourbaix diagram of palladium at 25°C [126]

What one expects to see is a current that gradually decreases over a long period of time until it reaches a stable and very low value, as shown in Figure 4.16, due to the formation of a protective layer.

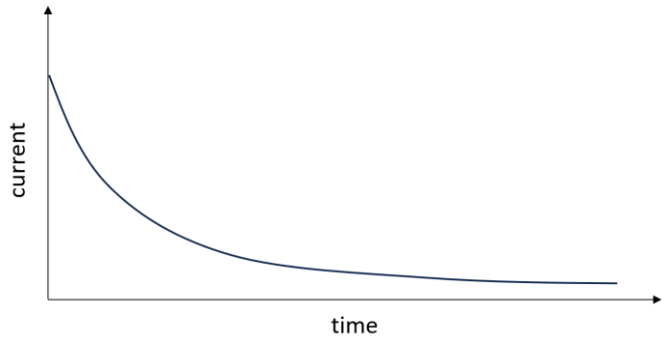

Figure 4.16 - Expected time evolution of the passivation current (before water electrolysis)

However, the results from the various tests carried out for the purposes of this thesis are different from what one would expect and an example obtained with a GFRE sample made of 6 layers of fibres is reported in Figure 4.17.

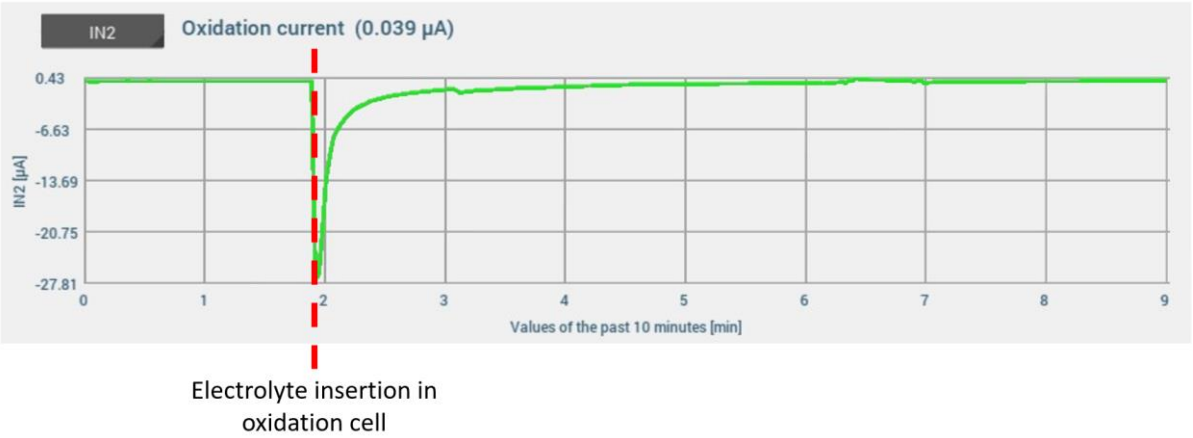

Figure 4.17 - Measured passive current evolution (GFRE, 6 layers)

The passivation current has a monotonically increasing trend. Moreover, it starts from a negative value and reaches a constant, positive value from below. This is counterintuitive and also incorrect. However, the value it settles at would not seem abnormal since, typically, the passivation current density falls approximately in the range between 0.01 mA/m^2 and a few mA/m^2. Considering that the sample surface exposed to the $NaHCO_3$ solution is 10 cm^2, the current density measured in this example is 0.039 mA/m^2, which is of the same order of magnitude as the expected value. But the time at which it reaches a constant value is rather short (in the order of minutes).

We now move on to the second step of the procedure, namely the application of the potential to the charging cell after filling it with the continuously recirculating electrolyte.

Continuing to measure the total oxidation current, consisting of permeation and background current, one would expect to see an increase in it from the application of the voltage (see Figure 4.18).

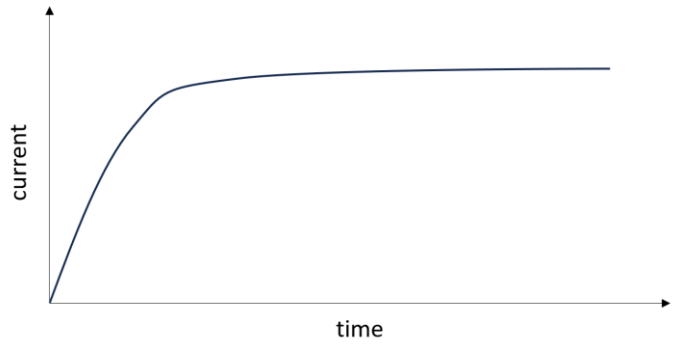

Figure 4.18 - Expected time evolution of the measured current after starting water electrolysis

This increase should be continuous, as the water splitting reaction starts and hydrogen atoms begin to infiltrate the sample. This occurs until a stable value is reached at stationary state. The attainment of a constant oxidation current value in this step is faster than in the case of the passivation current. On the other hand, the results of the tests carried out experimentally and shown in Figure 4.19 only highlighted that something was wrong.

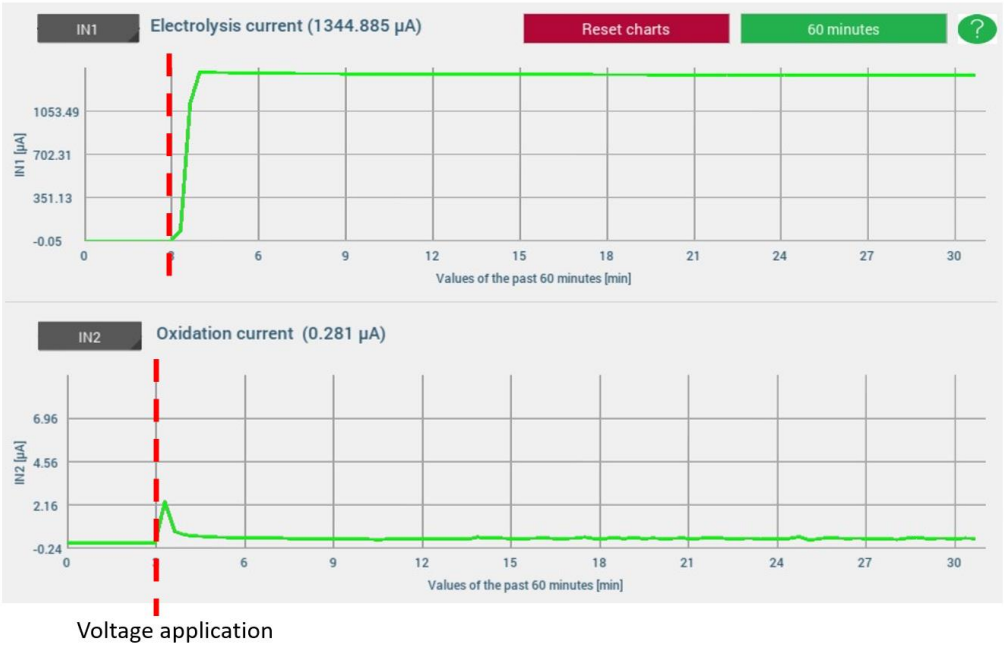

Figure 4.19 - Outcome of current measurements after water electrolysis start (GFRE, 6 layers)

Although a positive peak in the oxidation current is observed at the application of the voltage for electrolysis, it starts to decrease immediately afterwards. It develops a trend that is monotonically decreasing over time. However, it should be noted that the constant value of the oxidation current is greater than the background current (0,281 μA > 0,039 μA), as it should be.

Figure 4.20 gives an overview of the trends of total oxidation current (before and after the application of the potential in the loading cell.

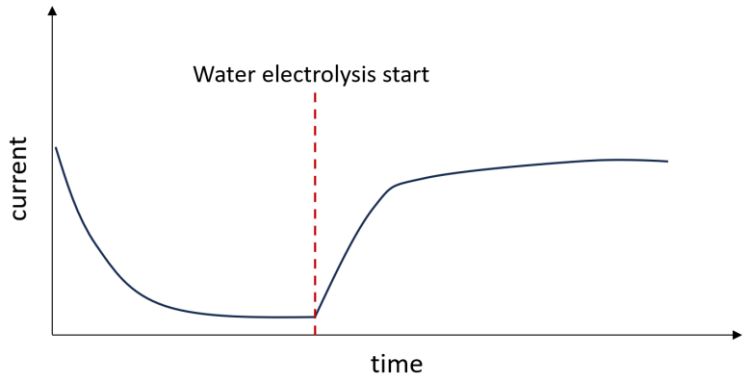

Figure 4.20 - Measured current as a function of time before and after water electrolysis

At first glance, it might seem that the error is due to a simple inversion of the connections to the positive and negative poles of the AMB box's ammeter, since the trends obtained are often almost opposite to those expected, at least in qualitative terms. However, it was verified that this was not the trivial reason for the errors.

The anomalies cannot even be justified as possible consequences of the fact that the material tested is not the one typically used for these tests, as this would not result in a distortion of the current trend over time, nor would it be due to hydrogen escaping from the areas of the sample exposed to air, as this would simply result in less hydrogen permeating and therefore less current. The same effect would be attributable to palladium if it were taken as the responsible, having a different permeability to hydrogen with respect to the FRP sample, namely a different amount of permeated hydrogen.

After several interventions by the company iChemAnalytics GmbH, which oversaw the entire setup, to check the correctness of the implemented procedure, all the equipment was sent to them, as per their request, to carry out further checks on the entire apparatus.

5 Fluid dynamic model

Since the previous analyses were performed to check the feasibility of the use of FRP as materials for pipe-in-pipe hydrogen transport, a model for the evaluation of the performances from the point of view of fluid dynamics has been also developed. The model allows to check if the pipe-in-pipe solution as a concept, the influence of roughness and the permeation of hydrogen allow to make this option competitive with conventional solutions (i.e., separate hydrogen and natural gas pipelines or blends)

The model that is used to describe the gas flow in the pipe is a stationary one-dimensional (1D) finite-volume model. This approach discretizes the pipe into small volumes in which the properties of the gas are assumed constant (e.g. pressure, density).

The simplifying assumption of being in a steady state is often chosen as a simple and efficient tool for design concerns [127] and it is representative of most of the conditions actually present in large pipelines in which the transients are usually slow.

The gas flow within the pipe is hence studied assuming these conditions:

- constant pipe section;
- 1D flow;
- compressible fluid;
- Newtonian fluid;
- isothermal flow.

The general 1D conservation equations underlying the problem are the continuity equation (5.1), the momentum equation (5.2) and the energy equation (5.3), whose form in the case of stationary conditions is:

$$\frac{\partial(\rho u)}{\partial x} = 0 \tag{5.1}$$

$$\frac{\partial p}{\partial x} = -\frac{f}{2D}\rho u^2 - \frac{p\,MM}{Z\,R\,T}\,g\,sin\theta \tag{5.2}$$

$$\frac{\partial}{\partial x}\left(\rho u\left(e + \frac{p}{\rho}\right)\right) = q\frac{\mathcal{P}}{A} + k\frac{\partial^2 T}{\partial x^2} + \frac{f}{2D}\rho u^3 \tag{5.3}$$

Since the flow is assumed isothermal, the energy equation is substituted by $T = const$.

In order to obtain the pipeline flow equations for the stationary case, the momentum equation is considered to obtain an equation that relates the operating conditions of temperature T and pressure p with the properties of the transported fluid (molecular mass MM, dynamic viscosity μ) and the pipe (diameter D, length L and roughness ε).

Having made the assumption of compressible fluid flow, the actual volumetric gas flow rate is not conserved and it is therefore common to refer to the standard volumetric flow rate F, which is instead conserved. Standard conditions are defined as p_0 = 1 atm and T_0 = 15°C. Using this assumptions, the abovementioned equations can be rewritten and integrated in the form that is known as Ferguson equation.

$$\frac{dp(x)}{dx} = -B\frac{F^2}{p(x)} - Gp(x) \tag{5.4}$$

With:

$$B = \frac{8\,f}{\pi D^5}\,\rho_0^2\,\frac{Z\,R\,T}{MM} \tag{5.5}$$

$$G = \frac{MM}{Z\,R\,T}\,g\,sin\theta \tag{5.6}$$

The differential equation can be rewritten using the definition of p^2 differential.

$$d\left(p^2(x)\right) = 2\,p(x)\,dp(x) \tag{5.7}$$

$$\frac{1}{2}\frac{dp^2(x)}{dx} = -BF^2 - Gp^2(x) \tag{5.8}$$

Integration over x is then performed and the contribution related to the elevation of the pipe is enclosed in a coefficient A. This results in algebraic equations that can be used in the finite-volume approach, where subscripts 1 and 2 are indicative of two sections of a pipe (see Figure 5.1).

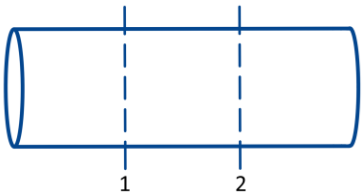

Figure 5.1 - Schematic representation of two generic sections of a pipe

$$BF^2 + Gp_2^2 = (BF^2 + Gp_1^2)\exp(-2GL) \tag{5.9}$$

$$A\,p_1^2 - p_2^2 = KLF^2 \tag{5.10}$$

$$S = 2GL = 2\,\frac{Z_0\,T_0\,\rho_0}{Z\,T\,p_0}\,g\,\Delta h \tag{5.11}$$

$$K = \frac{16\,f}{\pi^2 D^5}\,\frac{Z\,T\,p_0\,\rho_0}{Z_0\,T_0}\,\frac{1-e^{-s}}{S} \tag{5.12}$$

In the work to be developed later, a horizontal pipeline is considered (Δh = 0) and therefore the equation takes this form:

$$p_1^2 - p_2^2 = KLF^2 \tag{5.13}$$

Being:

$$S = 0 \tag{5.14}$$

$$\lim_{S\to 0}\frac{1-e^{-s}}{S} = 1 \tag{5.15}$$

$$K = \frac{16\,f}{\pi^2 D^5}\,\frac{Z\,T\,p_0\,\rho_0}{Z_0\,T_0} \tag{5.16}$$

It is not unusual to find studies in the scientific literature that assume constant values for the compressibility factor Z and the friction factor f. However, both parameters are influenced by the operating conditions along the pipeline and this simplification could lead to non-negligible errors. Anyway, the finite volume approach selected allows to keep values constant in each cell of the discretization, applying and solving the Ferguson equation in each one with the proper boundary conditions.

5.1. Compressibility factor

The compressibility factor Z is one of the factors that most influence the behaviour of the transported gas. It is a function of temperature, pressure and gas composition and indicates how far the gas deviates from ideal behaviour.

The standard ISO 12213-3 [128] defines it as “the ratio of the volume of an arbitrary mass of gas, at a specified pressure and temperature, to the volume of the same mass of gas under the same conditions as calculated from the ideal-gas law”.

Several equations of state and correlations exist for its calculation, depending on the application and the fluids involved.

The same standard gives a detailed characterisation equation for the calculation of Z for natural gas mixtures (see equation (5.17)).

$$Z = 1 + B\rho_m - \rho_r \sum_{n=13}^{18} C_n^* + \sum_{n=13}^{18} C_n^* \left(b_n - c_n k_n \rho_r^{k_n}\right) \rho_r^{b_n} e^{-c_n \rho_r^{k_n}} \tag{5.17}$$

where ρ_r is the reduced density, related to the molar density ρ_m by the equation:

$$\rho_r = K^3 \rho_m \tag{5.18}$$

In the previous formulas b_n, c_n, k_n are constants and B, K, C_n^* are coefficients that depend on composition and temperature. All these values are provided by the normative.

Since the implementation of this formula in numerical solvers is rather complicated, it is often replaced with empirical correlations such as the American Gas Association (AGA) equation (5.19) and the Papay equation (5.20) for gas mixture [129].

$$Z_{Papay}(p,T) = 1 - 3.52\, p_r\, e^{-2.260 T_r} + 0.274\, p_r^2 e^{-1.87 T_r} \tag{5.19}$$

$$Z_{AGA}(p,T) = 1 + 0.257\, \frac{p}{p_{pc}} - 0.533 \frac{p}{p_{pc}} \frac{T_{pc}}{T} \tag{5.20}$$

In both equations, the dependence of the compressibility factor on the composition of the gas mixture is concealed within the pseudo-critical temperature and pressure, T_{pc} and p_{pc}, respectively, which are calculated as weighted averages of the critical temperatures and pressures of the individual components, i.e. T_c and p_c.

$$T_{pc} = \sum_{i=1}^{N} x_i\, T_{c,i} \tag{5.21}$$

$$p_{pc} = \sum_{i=1}^{N} x_i\, p_{c,i} \tag{5.22}$$

Lastly, T_r and p_r are the pseudo-critical reduced temperature and pressure.

$$T_r = \frac{T}{T_{pc}} \tag{5.23}$$

$$p_r = \frac{p}{p_{pc}} \tag{5.24}$$

These last solutions are relevant to decrease complexity and calculation time, in particular when the number of evaluations of Z is high (e.g., iterative calculations, CFD, …). In our case, the study is limited to a single pipe and a limited number of cells, making possible to use the complete formulation. It is implemented in commercial libraries that can be linked to in-house codes. One possibility to assess the

compressibility factor is to use REFPROP, which is a computer programme distributed by NIST (US National Institute of Standards and Technology) [130].

The REFPROP database offers accurate and dependable data on the thermophysical properties of a wide range of fluids and fluid mixtures. The software draws upon an extensive reservoir of experimental data and sophisticated mathematical models, enabling the estimation of properties required by users under specific temperature and pressure conditions. These data and models are consistently updated and validated to ensure their accuracy.

The analyses performed in this work rely on this library, as it is the option that best represents the true values of the gas properties for both high pressures and high percentages of hydrogen in the gas mixture.

5.2. Friction factor

Even in the case of the friction factor, there are several correlations to choose from that are valid for different flow conditions.

In the case of laminar flow ($Re < 2300$), the Hagen-Poiseuille formula is used:

$$f = \frac{64}{Re} \tag{5.25}$$

Where:

$$Re = \frac{\rho\, u\, D}{\mu} \tag{5.26}$$

In the formula u is the fluid velocity.

When, on the other hand, the Reynolds number Re increases and one enters the turbulent flow regime, it is widely accepted that the friction factor calculated via the implicit Colebrook-White equation is the most accurate.

$$\frac{1}{\sqrt{f}} = -2\log\left(\frac{1}{3.71}\frac{\varepsilon}{D} + \frac{2.51}{Re\sqrt{f}}\right) \tag{5.27}$$

However, this equation is implicit and requires iterations to be solved. Consequently, it is often preferred to use explicit approximations, such as Hofer's, which is the one chosen for this work. It allows the calculation process to be simplified while still maintaining high accuracy.

$$\frac{1}{\sqrt{f}} = -2\log\left(\frac{1}{3.71}\frac{\varepsilon}{D} + \frac{4.518}{Re}\log\left(\frac{Re}{7}\right)\right) \tag{5.28}$$

6 Fluid dynamic assessment: natural gas – hydrogen blend transport

As far as the quality of the gas is concerned, Algerian natural gas is selected, such as that which enters Italy at Mazara del Vallo in Sicily. This choice is assumed to not influence in a relevant way the comparison, since the fluid dynamics behaviour of different natural gases are similar. The reference composition is shown in Table 6.1 .

Table 6.1 - Reference composition (% vol) of Algerian natural gas [131]

	CH_4	C_2H_6	C_3H_8	CO_2	N_2
% vol	89.9	8.4	1.2	0	0.5

Despite the possibility to analyse a continuous range of hydrogen fraction, some percentages of hydrogen in the blend are considered to limit the number of cases: 0% (pure natural gas), 2% (current limit in Italy), 5% (maximum allowed in Spain, also indicative of the current limit in France of 6%), 10% (situation in Germany), 20% (value frequently considered in natural gas infrastructure suitability tests), and then higher percentages where the hydrogen content in the blend is relevant, i.e. 50%, 80%, 90% and 100%.

The intention is to focus on the natural gas transmission grid where the diameters and pressures involved are larger than in the distribution grid, making more reasonable the concept of inserting a second pipe in the existing one.

Therefore, the values of the various parameters will be those typical of pipes of the first specie, according to the classification in force in Italy, which provides for the classification of seven pipe species on the basis of maximum operating pressure (MOP) and shown in Table 6.2 [132].

Table 6.2 - Pipeline classification based on maximum operating pressure

Species	**I**	**II**	**III**	**IV**	**V**	**VI**	**VII**
MOP [bar]	> 24	12-24	5-12	1.5-5	0.5-1.5	0.04-0.5	< 0.04

Therefore, metallic pipes with an internal diameter D of 0.7 m are considered and consequently a roughness of 0.046 mm is chosen (typical of commercial steel ducts) [99].

Two different cases are studied:

(i) the same energy flow rate is imposed as the case where pure natural gas is transported (no hydrogen addition), so that they can meet the same energy demand. In this case, different flow rates are allowed to match the energy flow for a given blend. This will be referred to as "Constant energy" case.

(ii) the same pressure drop of natural gas case is imposed for each of the different blends, representing a case in which the compressor stations are at the same distance. This will be referred to as "Retrofit" case.

The two cases are analysed considering a constant temperature equal to 15°C, while pressure value considers two scenarios, representative of national (A) and regional (B) first specie transport pipeline:

A. p_{in} = 70 bar;
   p_{fin} = 50 bar.

B. p_{in} = 50 bar;
   p_{fin} = 30 bar

where p_{in} is the initial inlet pressure while p_{fin} is the final pressure, i.e., the minimum acceptable pressure at which the gas needs to be recompressed.

6.1. Constant energy

This section investigates the variations that occur in the pressure drop as the percentage of hydrogen in the blend changes, keeping the energy flow inside the pipe equal to that which occurs with the transport of natural gas only. This case corresponds to a situation in which final users do not experience any variation in the amount of energy received.

The energy flow rate of natural gas $\dot{E}_{NG}$, considering a volumetric flow rate of F_{NG}, is equal to:

$$\dot{E}_{NG} = F_{NG} \cdot HHV_{NG} \tag{6.1}$$

The volumetric flow rate for all the different blends, which is necessary for the pressure drop calculations, is computed as:

$$F = \frac{\dot{E}_{NG}}{HHV} \tag{6.2}$$

while the higher heating value of a gas mixture is determined as:

$$HHV = \sum_i HHV_i \cdot x_i \tag{6.3}$$

wherex_i is the molar fraction of the different gases involved.

Thus, the HHV of a H_2-NG blend is:

$$HHV = HHV_{NG} * (1 - x_{H2}) + HHV_{H2} * x_{H2} \tag{6.4}$$

where x_{H2} is the hydrogen molar fraction in the blend.

Since we are dealing with a mixture of gases, we must also take into account in the calculations that the molar mass of the mixture is computed as:

$$MM = \sum_i MM_i * x_i \tag{6.5}$$

The standard volumetric flow rate of natural gas F_{NG} has been taken equal to 200000 Sm^3/h and the assumed values for the higher heating value of natural gas HHV_{NG} and hydrogen HHV_{H2} are 39.73 MJ/Sm^3 (from the Algerian gas composition) and 12.09 MJ/Sm^3 [133] respectively.

Table 6.3 contains the values of the higher heating value and volume flow rate of the different blends, keeping the energy flow rate equal to that of pure natural gas, i.e. 2207 MW.

Table 6.3 - HHV and volume flow rate for different H_2-NG blends and a constant energy flow of 2207 MW

% H_2	**HHV [MJ/Sm³]**	**F [Sm³/h]**
0%	39.73	200000
2%	39.18	202822.05
5%	38.35	207207.68
10%	36.97	214954.28
20%	34.20	232325.59
50%	25.91	306676.95
80%	17.62	451016.01
90%	14.85	534940.08
100%	12.09	657237.39

Since the volumetric higher heating value of hydrogen HHV_{H2} is lower than that of natural gas HHV_{NG}, the HHV of the blend decreases as the hydrogen fraction in the blend increases.

Consequently, it is easy to see that if the objective is to transport the same amount of energy, it is necessary to work with higher volumetric flow rates in the case of the blend, which increase proportionally to the hydrogen content.

6.1.1. Scenario A: p_{in} = 70 bar, p_{fin} = 50 bar

In Scenario A, the inlet pressure p_{in} (i.e., the maximum) is 70 bar while the minimum permissible pressure p_{fin}, such that it will be necessary to recompress, is 50 bar.

Figure 6.1 shows the variation of pressure along the pipeline for different blend compositions, as results from the application of the fluid dynamic model. The intersection between the pressure curves and the horizontal red line at 50 bar enables the identification of the distance L_{fin} at which the gas needs to be recompressed. In other words, L_{fin} corresponds to the distance at which the minimum pressure p_{fin} is reached.

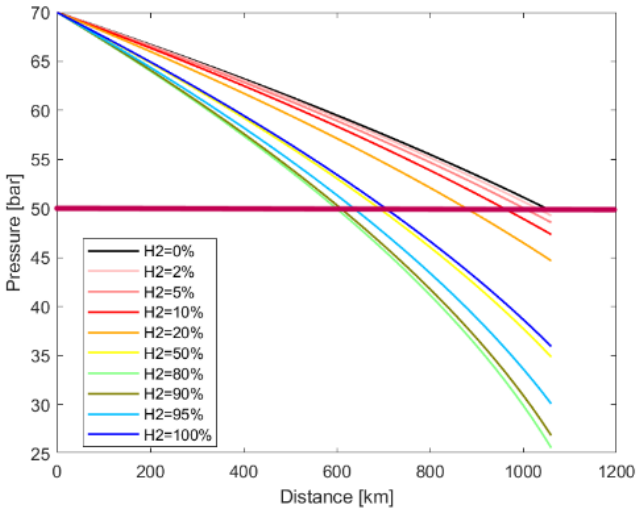

Figure 6.1 - Pressure drop of different H_2 blends (Constant energy 2207 MW, Scenario A)

As Figure 6.1 shows, when natural gas is blended with hydrogen pressure drops increase and, consequently, the distance between two compressor stations L_{fin} decreases. Looking at Table 6.4, it can be seen that the L_{fin} of the blend with H_2 at 90% is nearly 60% of that of the case of pure natural gas.

The trend, however, is not monotonically increasing, as the pressure drop increases up to an upper limit of hydrogen fraction at which a maximum is reached. In fact, L_{fin} in the 90% and 100% H_2 case is greater than the 80% H_2 case, contrary to what one would expect when observing the trend for smaller percentages (see Table 6.4). Having identified such behaviour, an additional point at high hydrogen fraction (specifically, a 95% H_2 blend) is investigated, and results confirm the observed trend.

Table 6.4 - Distance of compressor stations for different blends (Constant energy, Scenario A)

% H_2	**0%**	**2%**	**5%**	**10%**	**20%**	**50%**	**80%**	**90%**	**95%**	**100%**
L_{fin} [km]	1060	1040	1020	960	880	700	600	620	640	720

Figure 6.2 shows the increase in pressure drop compared to the case of natural gas alone (0% H_2) for a fixed distance of 100 km, and the trend to a maximum followed by a decline is evident.

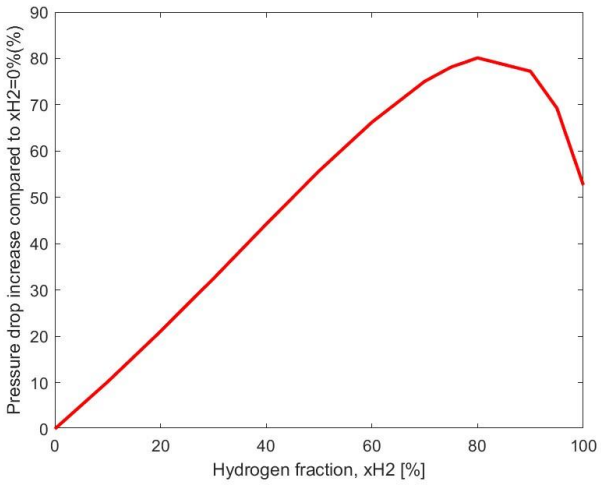

Figure 6.2 - Pressure drop increase compared to NG as a function of H_2 fraction in the blend (Constant energy, Scenario A)

Pressure losses increase significantly when mixing hydrogen with natural gas. An injection of 20% H_2, which is being discussed in many countries as a viable short-term solution, is related to around 20% increase in the pressure drop with respect to what happens for pure natural gas. The increase in pressure drop is not proportional to the hydrogen content in the blend but reaches a maximum for a hydrogen fraction of about 80 %. This behaviour results from the opposite trends that velocity and density feature as the hydrogen content increases. Specifically, density decreases monotonically, while velocity increases to ensure that the energy flow remains constant (see Figure 6.3). As both are included in the calculation of pressure drop, there will be a certain fraction of hydrogen in the blend beyond which the contribution of the reducing gas density is higher than that of the increase in velocity.

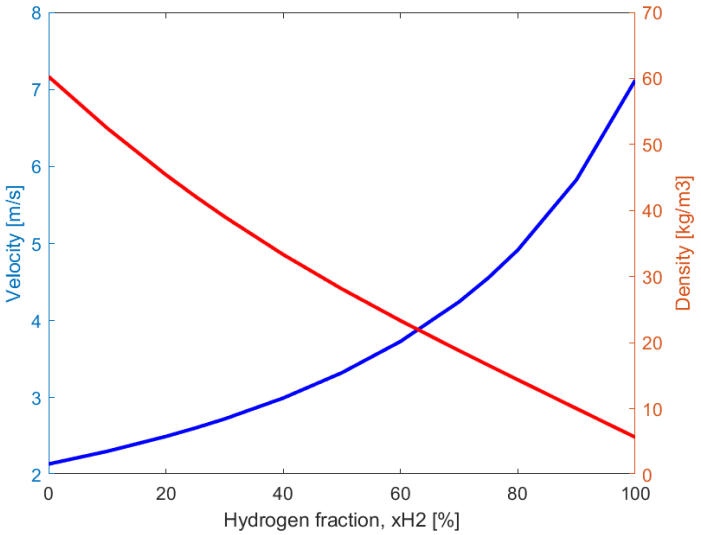

Figure 6.3 – Density and velocity as a function of H_2 fraction (Constant energy, Scenario A)

In Figure 6.4 is plotted the trend of gas velocities as a function of distance for different levels of hydrogen within the blend.

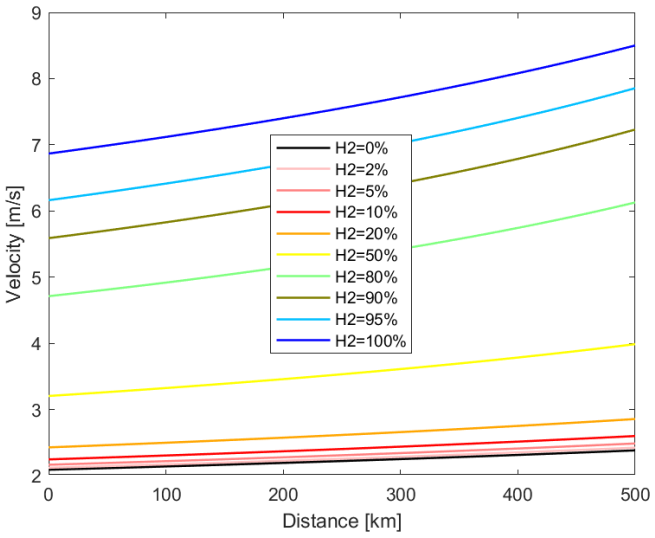

Figure 6.4 - Gas velocity as a function of the distance (Constant energy, Scenario A)

It can be seen immediately how, once a percentage of hydrogen is fixed, as the distance increases, the gas velocity also increases. The reason can be easily understood by considering the equation that correlates volumetric flow rate and gas velocity.

Knowing that the standard volumetric flow rate can be written as:

$$F = u \,.\, A \,.\, \frac{p}{p_0} \tag{6.6}$$

where u is the velocity of the gas inside the pipe and A is the cross section of the pipe itself, it is easily derived that:

$$u = \frac{\frac{F}{3600} \cdot \frac{p_0}{p}}{\frac{\pi D^2}{4}} \left[\frac{m}{s}\right] \tag{6.7}$$

The units to be entered in the formula are [Sm^3/h] for F, [m] for D and p_0 is the standard pressure, which is 1.01325 bar.

Therefore, considering that pressure is at the denominator and that it decreases with distance due to pressure drops, velocity increases along the pipeline, always considering the diameter constant.

Likewise, by increasing the percentage of hydrogen within the blend, the velocity also increases, as reported in Table 6.5. This happens because, for higher hydrogen contents, the volumetric flow rate (which is at the numerator) must increase to deliver the same amount of energy (see Table 6.3). In addition, the pressure (at the denominator) decreases as well, losses being greater for higher percentages of H_2 (except for very high values, where the phenomenon described above and depicted in Figure 6.2 occurs).

Table 6.5 – Initial and final velocity of the gas along the pipe (Constant energy, Scenario A)

% H_2	**0%**	**2%**	**5%**	**10%**	**20%**	**50%**	**80%**	**90%**	**95%**	**100%**
u_{in} [m/s]	2.090	2.119	2.165	2.246	2.427	3.204	4.712	5.589	6.162	6.867
u_{fin} [m/s]	2.940	2.981	3.057	3.146	3.402	4.514	6.601	7.895	8.648	9.713

The gas velocity should not be excessive so as to limit adverse phenomena such as transport of any impurities, pressure drop and noise. Regarding the transmission grid, particularly for pipelines classifiable as first species, typical velocity values are in the order of a few m/s, typically between 2 m/s and 3 m/s. These values could change for specifically designed pipelines dedicated to blends, but at the moment no indications are available in this sense.

As can be seen from Table 6.5, in the case of blends with up to 20% hydrogen, the velocity values at the inlet and at the point where the minimum pressure of 50 bar is reached are reasonable. The same does not hold for more substantial injections of hydrogen into natural gas, especially in the case of 80%, 90% and 100% (pure hydrogen), where the average velocity along the pipe exceeds 5 m/s. This could lead to problems such as those listed above and could require dedicated design of the pipeline, limiting the retrofit options.

6.1.2. Scenario B: p_{in} = 50 bar, p_{fin} = 30 bar

In Scenario B the values of inlet pressure and pressure at which recompression is required are lower than in scenario A, corresponding to 50 bar and 30 bar respectively, representative of regional transport grids.

It is possible to observe what changes there are in terms of pressure drop and flow characteristics compared to the case studied in the previous section.

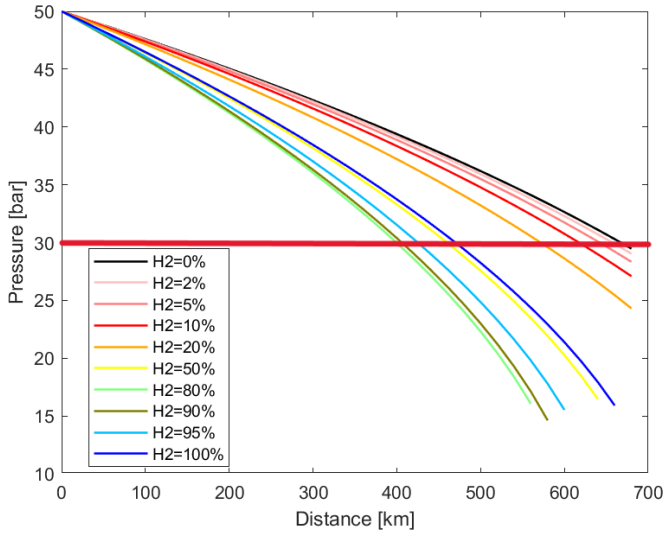

Figure 6.5 - Pressure drop of different H_2 blends (Constant energy 2207 MW, Scenario B)

Also in Scenario B, as expected, the pressure drop is greater in the case of blend transport than in the case of pure natural gas, and in fact the distance L_{fin} at which the minimum pressure is reached is lower, so it is necessary to recompress the gas sooner (see Figure 6.5).

It can be noticed that in this case the distance covered by NG before hitting the limit cannot be physically reached by blends above 80%H_2, for which the pressure drop is

too high. Hence, to transport the same energy, nearest compressor stations are mandatory.

If the growth of the pressure drop is plotted against the case of pure NG (0% H_2) as a function of the hydrogen fraction in the blend, as shown in Figure 6.6, it can be find again the same trend as in scenario (A): there is no continuous growth but a maximum is reached after which a moderate decrease begins to be observed. The maximum occurs near 80% H_2, similarly to what observed in Scenario A.

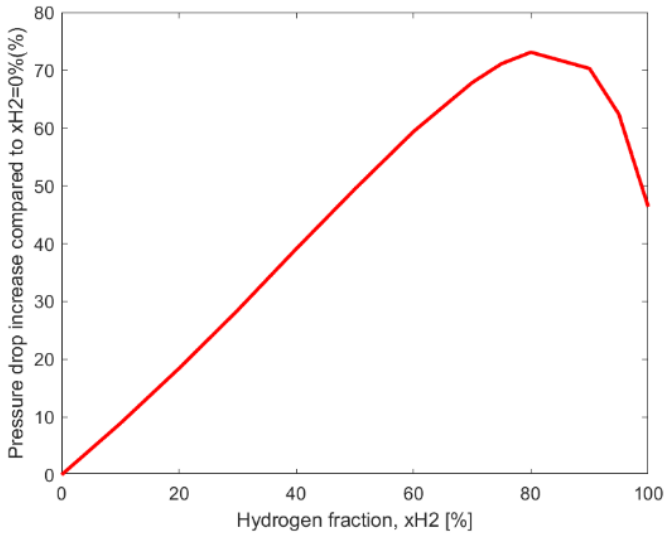

Figure 6.6 - Pressure drop increase compared to NG as a function of H_2 fraction in the blend (Constant energy, Scenario B)

The same behaviour is expressed in terms of L_{fin} in Table 6.6, which shows that this distance for the blend with 80% hydrogen (the case with the lowest L_{fin}) is slightly higher than half (59%) of the pure natural gas case, while it is about 71% increases in the case of 100% H_2.

Table 6.6 - Distance of compressor stations for the different blends (Constant energy, Scenario B)

% H_2	**0%**	**2%**	**5%**	**10%**	**20%**	**50%**	**80%**	**90%**	**95%**	**100%**
L_{fin} [km]	680	660	660	620	580	460	400	420	440	480

For the sake of completeness, the trends in gas velocity and density as a function of the hydrogen content in the blend are shown in the Figure 6.7. Confirming for the

behaviour observed for Scenario A, these two parameters have different, or rather, opposite trends.

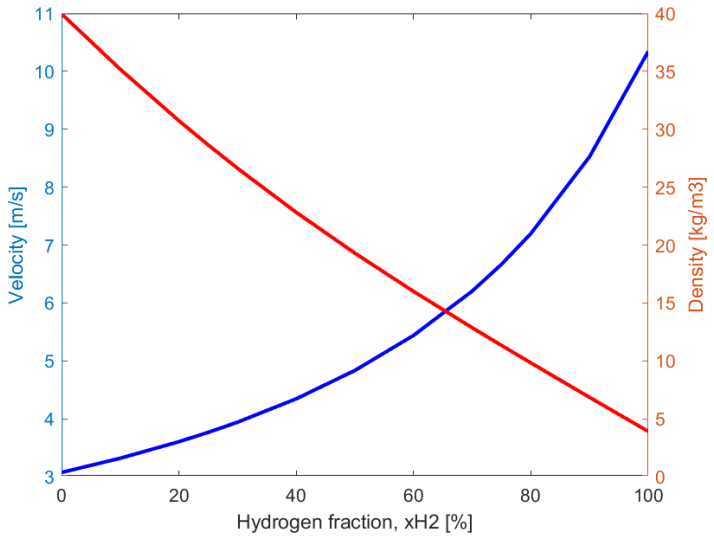

Figure 6.7 - Density and velocity as a function of H_2 fraction (Constant energy, Scenario B)

The interpretation of the graph in Figure 6.7 is still the same as before: having arrived at a hydrogen content close to 80%, the contribution of decreasing density to pressure loss weighs more heavily than that associated with increasing flow velocity.

The trend of velocity for different percentages of hydrogen in the blend along the pipeline is analysed for scenario B too (see Figure 6.8). The gas velocity increases as the distance travelled increases, the pressure being lower as one moves away from the inlet (due to friction phenomena). The same happens when a distance is fixed and the influence of hydrogen percentage is observed: the larger the amount of H_2 injected into natural gas, the higher the gas velocity.

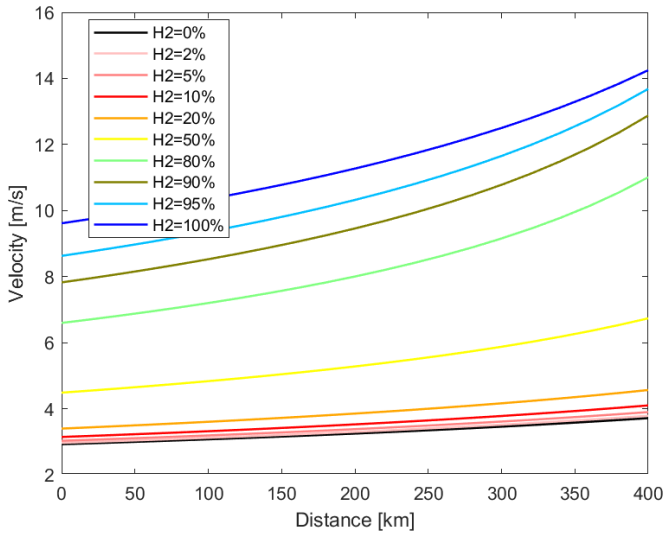

Figure 6.8 - Gas velocity as a function of the distance (Constant energy, Scenario B)

If we again consider the reference values for gas velocity in first species pipelines used in scenario (a), i.e., 2-3 m/s, it is immediate to see that the velocities in Table 6.7 deviate from these values already at low hydrogen percentages. Already at 50% H_2 the average velocity is above 5 m/s and for higher percentages it is higher than 10 m/s, with a maximum velocity along the pipe (the final one before recompressing) even exceeding 15 m/s.

Table 6.7 - Initial and final velocity of the gas along the pipe (Constant energy, Scenario B)

% H_2	**0%**	**2%**	**5%**	**10%**	**20%**	**50%**	**80%**	**90%**	**95%**	**100%**
u_{in} [m/s]	2.925	2.967	3.031	3.144	3.398	4.486	6.597	7.825	8.627	9.613
u_{fin} [m/s]	4.963	4.965	5.186	5.261	5.740	7.478	11.006	13.463	14.853	16.335

It is important to address this phenomenon as it could lead to mechanical and acoustic issues.

6.2. Retrofit

This section studies a case in which the same infrastructure is used for blends (i.e., no changes in maximum pressure drop and in compressor station distance) and the changes occurring for various fractions of hydrogen in the blend when the same pressure drop along the pipe as the case of pure natural gas (0% H_2) is imposed. The underlying idea is to simulate a complete retrofit case of the infrastructure used for natural gas: in addition to having equal p_{in} and p_{fin} in the different cases (same kind of compressor), the distance L_{fin} at which the compressor station is located is also the same and is set equal to the NG case. The degree of freedom in this case are both the volumetric flow rate and the energy transported.

Scenarios A and B are analysed as already discussed in Chapter 5.

6.2.1. Scenario A: p_{in} = 70 bar, p_{fin} = 50 bar

Scenario A considers compression from 50 bar to 70 bar, with compressor stations placed at the distance where a pure natural gas pipeline would reach the minimum pressure of 50 bar, i.e., 1060 km from the inlet (see Table 6.4).

Table 6.8 shows the volumetric flow rate and energy flow rate for different percentages of hydrogen contained in the transported gas.

Keeping the pressure drop of the gas along the pipe fixed, the volumetric flow rate increases as the fraction of hydrogen increases, in contrast to the energy flow rate, which undergoes the opposite behaviour: the greater the amount of hydrogen, the lower the energy transported by the pipeline.

Table 6.8 - Volume and energy flow rate as a function of H_2 fraction with compressor stations from 50 to 70 bar at 1060 km from each other (Retrofit, Scenario A)

% H_2	F [Sm^3/h]	Ė [MWh/h]
0%	200000	2207
2%	200751	2185
5%	202113	2153
10%	204689	2102
20%	210951	2004
50%	245189	1765
80%	334973	1639
90%	400318	1652
100%	529695	1779

This is made evident in Figure 6.9, where the two trends mentioned above are shown.

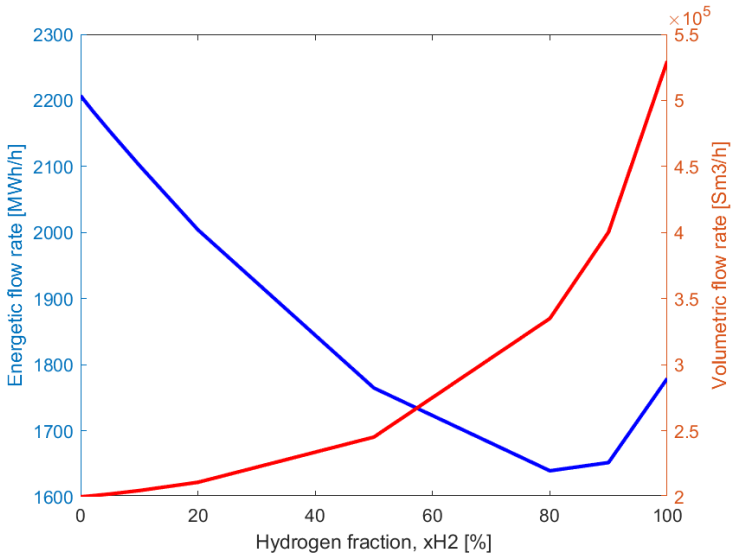

Figure 6.9 - Energy and volumetric flow rate trends as a function of H_2 fraction (Retrofit, Scenario A)

If the two extreme cases of pure NG and pure H_2 are examined, it can be seen that in the pure H_2 case there is a flow rate that is well above twice as high as in the NG case (165% more gas is transported in terms of volume). However, the dramatic increase in delivered volume does not balance the reduction in the delivered energy, which is 20% lower in the pure H_2 case.

Even more interesting is to see how the trend is not monotonic in energy flow rate, as opposed to volumetric flow rate. In fact, the volumetric flow rate is continuously increasing as the fraction of hydrogen in the gas increases, while the energy flow rate decreases until it reaches a minimum, beyond which it starts growing again.

This phenomenon is explained by referring to the formula that links the flow rate F and the energy flow $\dot{E}$:

$$\dot{E} = F \cdot HHV \tag{6.8}$$

The higher heating value HHV acts as a multiplicative factor of the volumetric flow rate and it decreases with the percentage of hydrogen in the blend, HHV_{H2} being less than HHV_{NG}. For a value close to 80% hydrogen in the blend, the increase in F has a greater contribution than the decrease in HHV on $\dot{E}$, which then increases again.

As far as the velocity trend is concerned, we have the same tendency as in the previous chapter "Constant energy": the velocity increases along the pipe and, given a certain distance, increases as the hydrogen fraction increases, as depicted in Figure 6.10.

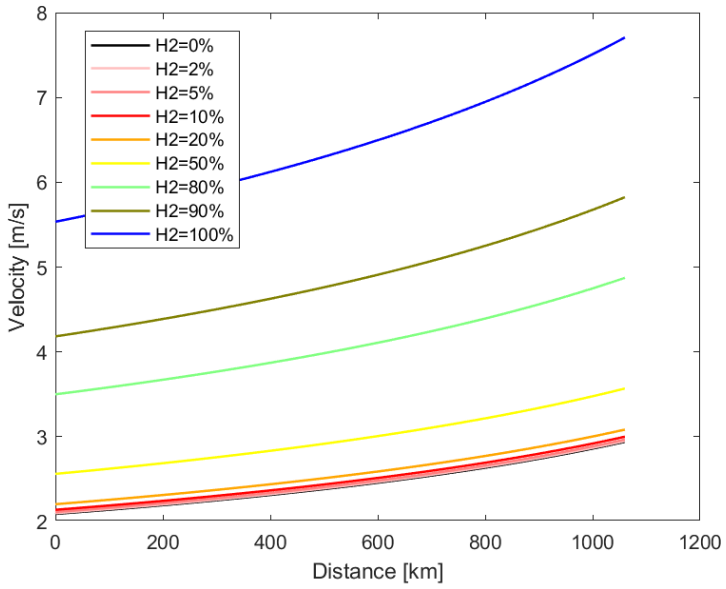

Figure 6.10 - Gas velocity as a function of the distance (Retrofit, Scenario A)

Also in this case, the gas velocity turns out to be excessive when a large amount of hydrogen is injected into the natural gas, going beyond the typical values found in a pipe of the first species (see Table 6.9). It is therefore necessary to consider possible problems arising from this and possible pipeline redesign and substitution.

Table 6.9 - Initial and final velocity of the gas along the pipe (Retrofit, Scenario A)

% H_2	**0%**	**2%**	**5%**	**10%**	**20%**	**50%**	**80%**	**90%**	**100%**
u_{in} [m/s]	2.090	2.097	2.112	2.140	2.204	2.562	3.500	4.182	5.534
u_{fin} [m/s]	2.940	2.950	2.966	3.000	3.083	3.568	4.873	5.824	7.706

6.2.2. Scenario B: p_{in} = 50 bar, p_{fin} = 30 bar

In this retrofit scenario, the compression provided by the compressor stations is fixed, as is their location, and these values are lower than in scenario A: the inlet pressure is 50 bar, the minimum pressure is 30 bar, and the distance at which compression is required, L_{fin}, is 680 km (corresponding to the pure NG case).

Table 6.10 shows that in the volumetric flow rate increases and the energy flow rate decreases as the hydrogen fraction increases.

The non-monotonic trend of $\dot{E}$ is again observed (see Figure 6.11), reaching a minimum at 80% H_2, after which a moderate growth is observed.

Taking pure NG values as a reference, at 80% H_2, F grows by approximately 71% and $\dot{E}$ decreases by about 24%; for pure H_2, F grows by around 171% and $\dot{E}$ decreases by roughly 17%.

Table 6.10 - Volume and energy flow rate as a function of H_2 fraction with compressor stations from 30 to 50 bar at 680 km from each other (Retrofit, Scenario B)

% H_2	F [Sm3/h]	Ė [MWh/h]
0%	200000	2207
2%	201120	2189
5%	202866	2161
10%	206004	2115
20%	213516	2029
50%	250919	1806
80%	342950	1678
90%	409865	1691
100%	542295	1821

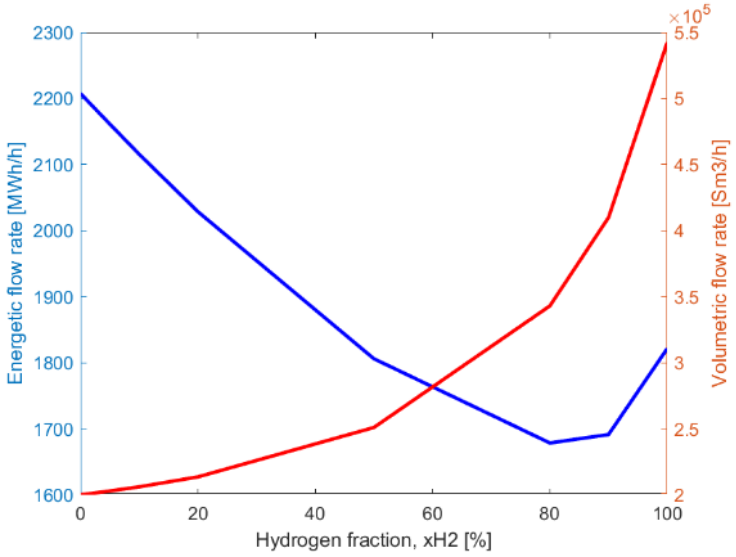

Figure 6.11 - Energy and volumetric flow rate trends as a function of H_2 fraction (Retrofit, Scenario B)

Focusing now on the values assumed by the velocity at which the gas flows, these are higher than in Scenario A, and for large percentages of hydrogen the velocity is

unreasonable, far exceeding the typical values of the transmission grid, as already discussed in the other cases (see Figure 6.12 and Figure 6.11).

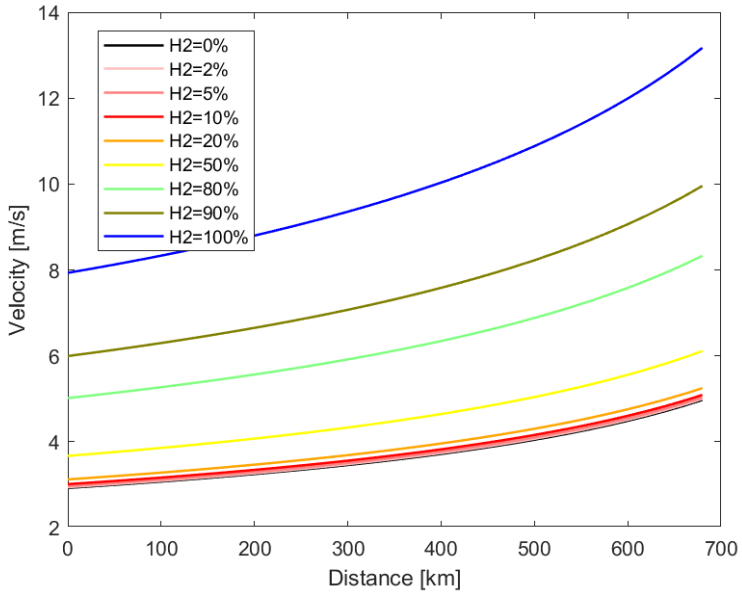

Figure 6.12 - Gas velocity as a function of the distance (Retrofit, Scenario B)

Table 6.11 - Initial and final velocity of the gas along the pipe (Retrofit, Scenario B)

% H_2	**0%**	**2%**	**5%**	**10%**	**20%**	**50%**	**80%**	**90%**	**100%**
u_{in} [m/s]	2.925	2.942	2.967	3.013	3.123	3.670	5.016	5.995	7.932
u_{fin} [m/s]	4.973	4.999	5.031	5.089	5.246	6.111	8.328	9.956	13.170

6.3. Summary of blend results

In this section, the results obtained from scenarios A and B are summarised and commented for both the "Constant energy" case, in which the different blends transport the same energy, and the "Retrofit" case, in which a retrofit of the natural gas infrastructure is simulated, with compressor stations operating at the same inlet and outlet pressures and placed at the same distance.

6.3.1. Constant energy

The same energy flow rate is imposed on the various blends, equal to that established for the case of pure natural gas. This ensures that the same energy demand is met across all blending proportions. Table 6.12 contains the boundary conditions for scenarios A and B in terms of pressures and energy flow rate.

Table 6.12 - Initial and final pressures and energy flow rate for scenarios A and B (Constant energy)

	Scenario A	**Scenario B**
p_{in} [bar]	70	50
p_{fin} [bar]	50	30
$\dot{E}$ [MWh/h]	2207.22	2207.22

Figure 6.13 shows the pressure trends and the change in pressure loss compared to natural gas for the different hydrogen fractions considered.

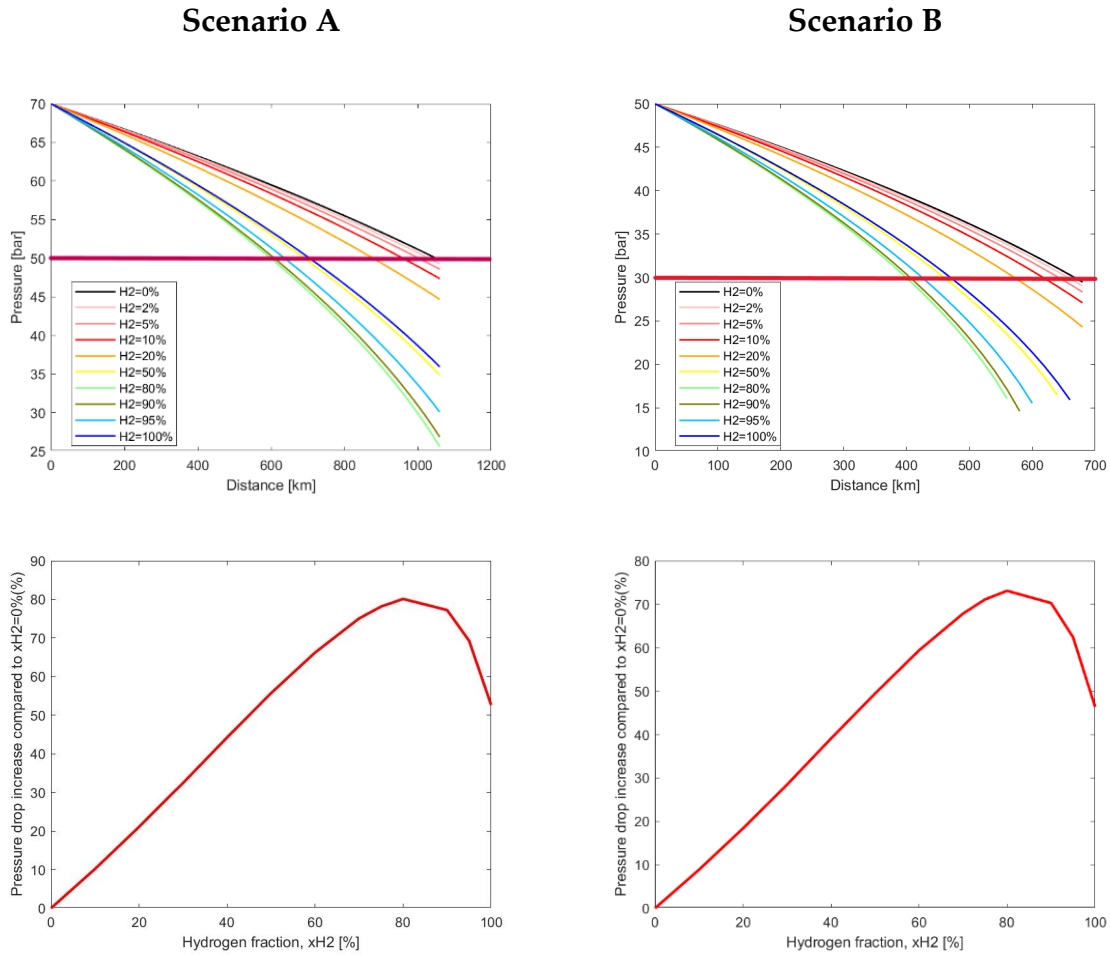

Figure 6.13 - Pressure drop (top) and pressure drop increase compared to NG (bottom) for different H_2 fractions for scenarios A and B (Constant energy)

As Table 6.13 shows, as the percentage of H_2 in the blend increases, the volumetric flow rate is larger, the pressure drop rises, and the distance L_{fin} at which the minimum pressure is reached decreases in both scenario A and scenario B. This trend holds true up to around 80% H_2 for both scenarios, beyond which there is a progressively smaller pressure loss compared to lower percentages. This is made evident in the Table 6.13, which shows the values of compressor station distances as a function of the percentage of hydrogen in the blend. It also contains the volume flow rate and the gas velocity values at the beginning and end of the pipe.

Table 6.13 - Volume flow rate, distance of compressor stations, initial and final velocity for scenarios A and B (Constant energy)

	% H_2	**0%**	**2%**	**5%**	**10%**	**20%**	**50%**	**80%**	**90%**	**100%**
	F $\cdot 10^{-5}$ [Sm^3/h]	2.000	2.028	2.072	2.150	2.323	3.067	4.510	5.349	6.572
A	**L_{fin} [km]**	1060	1040	1020	960	880	700	600	620	720
	u_{in} [m/s]	2.090	2.119	2.165	2.246	2.427	3.204	4.712	5.589	6.867
	u_{fin} [m/s]	2.940	2.981	3.057	3.146	3.402	4.514	6.601	7.895	9.713
B	**L_{fin} [km]**	680	660	660	620	580	460	400	420	480
	u_{in} [m/s]	2.925	2.967	3.031	3.144	3.398	4.486	6.597	7.825	9.613
	u_{fin} [m/s]	4.963	4.965	5.186	5.261	5.740	7.478	11.006	13.463	16.335

Comparing the two scenarios, scenario B is characterised by higher pressure drops than scenario A. In scenario B the average pressure drop per km is about 1.5 times that of Scenario A. If, for example, a blend of 50% hydrogen is considered, the former has about 0.043 bar/km, the latter instead has about 0.029 bar/km.

With a fixed percentage of hydrogen in the blend, as the distance increases and the pressure decreases, the gas velocity increases. Similarly, for a fixed distance, a larger hydrogen content in the blend results in a higher flow velocity. In general, the velocities for the blend far exceed those of pure natural gas, more than tripling them in the case of 100% H_2. Additionally, scenario B, exhibits higher velocities, approximately 1.5 times higher than those of scenario A because, for the same volume flow, pressures are lower.

While the final velocity values for scenario A should be equal to the initial velocity values for scenario B at same hydrogen fractions, considering that the volume flow rate, diameter, and pressure (50 bar) are the same, a small discrepancy is observed due to the spatial resolution adopted in the fluid dynamic model.

6.4. Retrofit

The pressure drop of the different blends is set equal to that of natural gas, simulating the case where compressor stations remain the same as those used for NG transport. Consequently, the minimum pressure point is reached at the same distance, L_{fin}.

Table 6.14 contains the boundary conditions for scenarios A and B in terms of pressures and distance of compressor stations.

Table 6.14 - Initial and final pressures and distance of compressor stations for scenarios A and B (Retrofit)

	Scenario A	**Scenario B**
p_{in} [bar]	70	50
p_{fin} [bar]	50	30
L_{fin} [km]	1060	680

To have the same distance as the compressor stations of pure natural gas, both the volume and the energy flow rate vary depending on the hydrogen content in the blend and, consequently, the gas velocities also change, as shown in Table 6.15.

Table 6.15 - Volume and energy flow rate, initial and final velocity for scenarios A and B (Retrofit)

	% H_2	**0%**	**2%**	**5%**	**10%**	**20%**	**50%**	**80%**	**90%**	**100%**
A	**F ·10^{-5} [Sm^3/h]**	2.000	2.008	2.021	2.047	2.110	2.452	3.350	4.003	5.297
	$\dot{E}$ ·10^{-3} [MWh/h]	2.207	2.185	2.153	2.102	2.004	1.765	1.639	1.652	1.779
	u_{in} [m/s]	2.090	2.097	2.112	2.140	2.204	2.562	3.500	4.182	5.534
	u_{fin} [m/s]	2.940	2.950	2.966	3.000	3.083	3.568	4.873	5.824	7.706
B	**F ·10^{-5} [Sm^3/h]**	2.000	2.011	2.029	2.060	2.135	2.509	3.430	4.099	5.423
	$\dot{E}$ ·10^{-3} [MWh/h]	2.207	2.189	2.161	2.115	2.029	1.806	1.678	1.691	1.821
	u_{in} [m/s]	2.925	2.942	2.967	3.013	3.123	3.670	5.016	5.995	7.932
	u_{fin} [m/s]	4.973	4.999	5.031	5.089	5.246	6.111	8.328	9.956	13.170

Results of the analysis show that, in order to obtain the same pressure drop of pure natural gas, hydrogen-natural gas blends require to transport a larger volume of gas. This behaviour is more marked in scenario B, due to the lower operating pressures. However, this corresponds to a lower energy flow rate. In other words, if the infrastructure is used in the same way as is used for natural gas to transport blend, the energy delivered to end users decreases.

The volume and energy flow rate trends for the different blends are shown in Figure 6.14, as well as the gas velocity along the pipe.

The decrease in the energy flow rate, as opposed to the increase in volume flow rate, is not continuous as the hydrogen fraction increases: it monotonically decreases until around 80% H_2, after which it undergoes an increment.

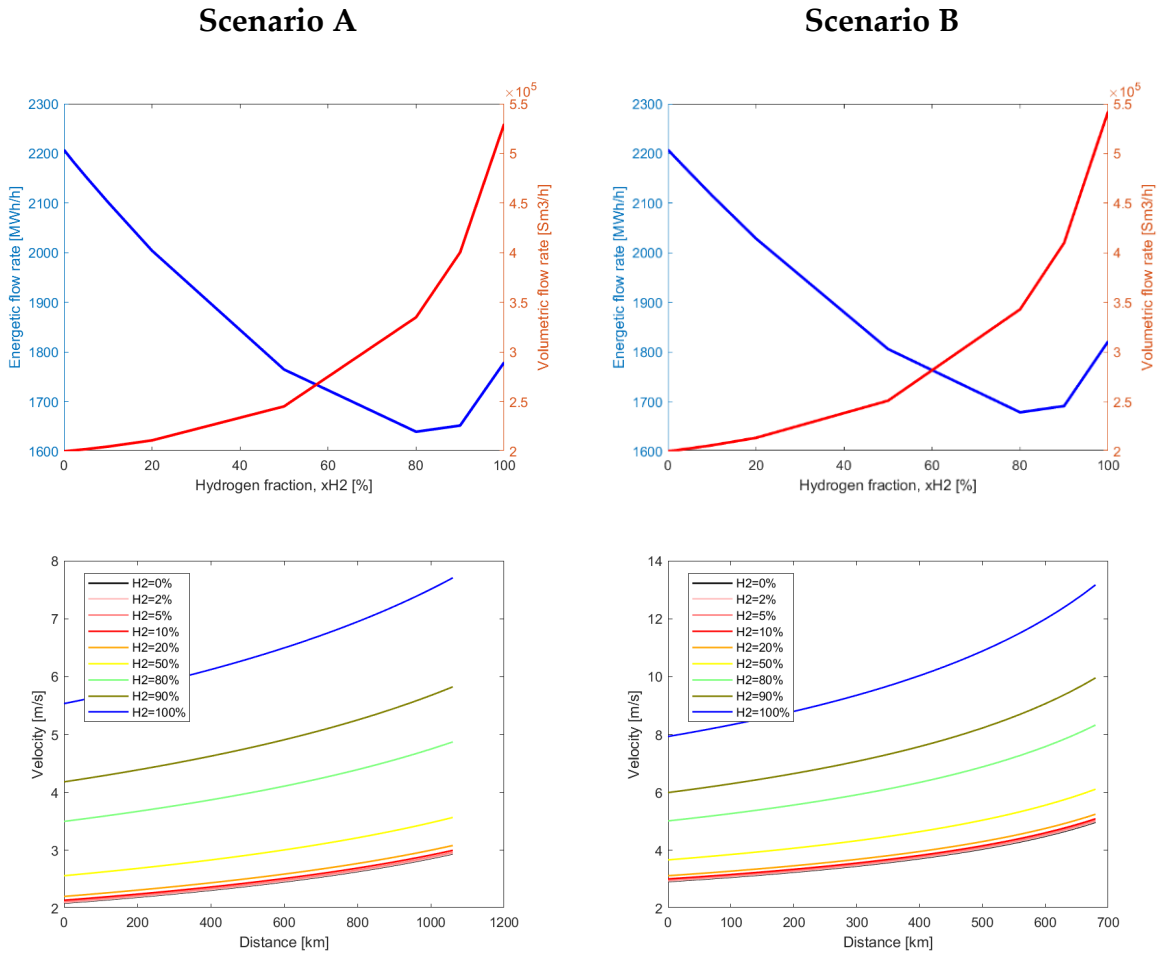

Figure 6.14 - Volume and energy flow rate (top) and gas velocity along the pipe (bottom) for different H_2 fractions for scenarios A and B (Retrofit)

In scenario A, indeed, for the 80% H_2 case, the volumetric flow rate is 67% higher compared to the natural gas case (0% H_2), and the energy flow rate is 26% lower. In the 100% H_2 case, these values become approximately 165% and 19%, respectively. In scenario B, using pure natural gas as a reference point again, for hydrogen fractions of 80% in the blend, there's a 71% higher volumetric flow and a 24% lower energy flow. For the pure hydrogen case (100% H_2), these percentages become 171% and 17%.

Referring again to Figure 6.14, the gas velocity increases along the pipe, and its value is higher the greater the hydrogen content transported in the blend. Keeping in mind that the length of the pipe is the same for different blends within the same scenario, it is generally observed that the velocity values at the beginning and end of the pipeline for the pure hydrogen case (100% H_2) are higher than the corresponding values for the pure natural gas case (0% H_2) as in the Constant energy case, summarized in Section 6.3, where they were more than tripled, whereas here they are about 2.5 times.

7 Fluid dynamic assessment: pipe-in-pipe system

The pipe-in-pipe system consists of the insertion of a smaller diameter pipe inside another larger diameter pipe (see Figure 7.1). The two can be concentric, if they share a centreline, or, otherwise, eccentric. The gas flow occurs both within the inner pipe and in the annular space between the two pipes.

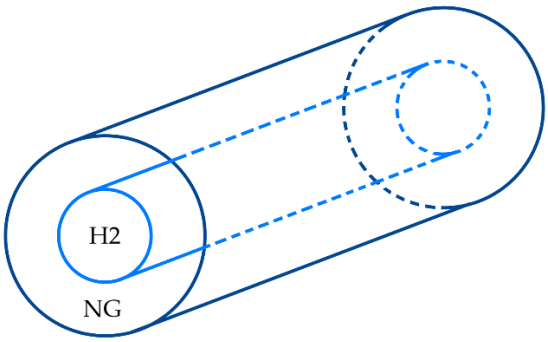

Figure 7.1 - Pipe-in-pipe concept for hydrogen and natural gas transport

Pipe-in-pipe transport is studied using the fluid dynamic model presented in Chapter 5. Being the model one-dimensional (1D), the fact that the two tubes are eccentric or concentric has no relevance, since the area wetted by the fluid is the same in the two cases. The distinction between these two configurations will instead assume considerable importance from the 2D case, in which it will not be possible to neglect turbulent motions of the fluid induced by the different configuration and by possible structural supports for the internal pipe.

In the Figure 7.2, two schematic representations are provided: one for the concentric case and the other for the fully eccentric case, where the inner pipe is attached to the bottom of the larger pipe. Among all degrees of eccentricity, this could be the most advantageous solution, as it would limit the system's complexity by not needing to account for the bending of the pipe, which would occur if the inner pipe were kept suspended instead. The latter makes also easier the positioning by gravity of the pipe itself.

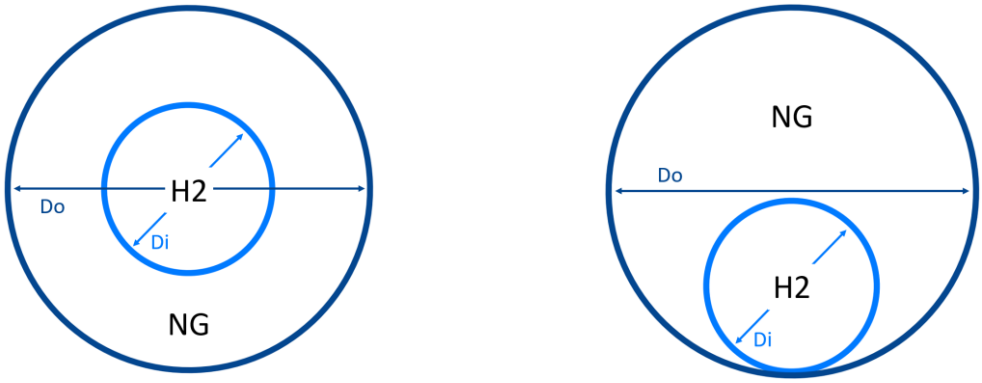

(a) Concentric (b) Completely eccentric

Figure 7.2 - Concentric (a) and completely eccentric (b) pipe-in-pipe system

This study seeks to address a specific need. The idea is to use the existing metal pipelines for natural gas transmission as an external pipe, inside which a smaller section pipe made of FRP, which is more flexible, can be inserted.

Natural gas is allowed to flow in the annulus created between the two pipes, without any damaging effect on either the metal or the composite polymer walls. Instead, hydrogen is carried in the inner tube, so that it only comes into contact with FRP, thus avoiding causing embrittlement problems resulting from the contact with metallic materials.

As opposed to blend transport, the pipe-in-pipe system enables the transport of both pure hydrogen and pure natural gas, which then can be made available for separate uses. While it is true that even in the event that a blend of hydrogen and natural gas is transported these two gases can be separated by means of the deblending techniques seen in the Section 2.2.3 (membranes, PSA, ...), in this case it would be possible to meet the demands for hydrogen and natural gas separately without having to resort to such intermediate steps, not to mention the greater ease and predictability in handling a pure gas as opposed to a gas blend.

This choice would also go along with the forecasts for future energy consumption in view of the Net Zero Emission Scenario, which envisage the continued use of natural gas and an increasing share for hydrogen, and would allow the already existing, well-established and extensive network to be exploited without incurring the problems associated with the creation of a separate structure including, for example, right-of-way restrictions, etc. In a second step, the annulus use can also be dismissed, keeping it as a safety cushion gas layer for the internal hydrogen pipe.

7.1. Model details

Pipe-in-pipe hydrogen and natural gas transport is analysed considering a system composed of an internal FRP pipe with diameter Di, and an external metallic pipe with diameter Do, which corresponds to a pipe of the existing natural gas network. Hydrogen is transported in the internal smaller pipe, while natural gas flows in the annular space between the two pipes. The annulus is modelled as an equivalent pipe with a diameter equal to the hydraulic diameter, defined as:

$$D_h = \frac{4A}{\mathcal{P}} \tag{7.1}$$

where A is the flow area and $\mathcal{P}$ is the wetted perimeter.

The wall thicknesses of the two pipes were not considered as a simplification of the calculations and are therefore zero.

The analysis assesses pipe-in-pipe transport as a retrofit solution. Accordingly, the same characteristics of the pipe that was considered in the blend case in Chapter 6 are considered for the outer pipe. In particular, it consists of a transmission network pipe of the first species, with a diameter of 0.7 m and roughness of 0.046 mm.

It is also important to consider that the two gases flow in contact with walls of different materials: hydrogen is in contact only with polymeric composite material, while natural gas is in contact also with the metallic inner wall of the larger diameter pipe. Three materials have been investigated for the inner pipe, all of which are composite polymeric materials: carbon fibre-reinforced epoxy resin (CFRE), glass fibre-reinforced epoxy resin (GFRE), and glass fibre-reinforced polypropylene (GFRPP). The roughness of the metal pipe ε_M was taken as that in the Chapter 6, while that of the FRP pipe ε_{FRP} was chosen on the basis of experimental results obtained at RWTH Aachen University in Aachen, Germany, presented in Chapter 3.

Thus, for the calculation of the friction factor for the hydrogen flow it was used ε_{H2} equal to ε_{FRP}, while for the natural gas flow ε_{NG} was taken as the weighted average of ε_M and ε_{FRP}, weighted over the areas wetted by the fluid:

$$\varepsilon_{NG} = \frac{\varepsilon_{FRP} \cdot A_{FRP} + \varepsilon_M \cdot A_M}{A_{FRP} + A_M} = \frac{\varepsilon_{FRP} \cdot D_i + \varepsilon_M \cdot D_o}{D_i + D_o} \tag{7.2}$$

More specifically ε_M is 0.046 mm and ε_{FRP} is chosen from experimental data depending on the considered material among glass fibre-reinforced epoxy (GFRE), carbon fibre-reinforced epoxy (CFRE) and glass fibre-reinforced polypropylene (GFRPP). The two terms A_{FRP} and A_M are the composite and metallic wetted surface by natural gas.

In order to make an analogy with the blend case, the flow rates of the "Retrofit" case (see Section 6.2) are considered and now split between pure hydrogen and pure natural gas based on the fraction of hydrogen in the corresponding blend. For example, the corresponding pipe-in-pipe system of the blend with 80% H_2 fraction has the same total flow rate, but 80% of it is transported as hydrogen in the smaller diameter pipe and the remaining 20% as natural gas in the annulus.

In order to deal with a consistent hydrogen flow rate, the cases where the hydrogen flow rate is 50% and 80% of the total flow rate are considered, corresponding to the blend cases with 50% and 80% hydrogen fraction. These correspond to the conditions in which pipe-in-pipe transport can be competitive, since if one were to transport relatively small quantities of hydrogen, there would not be an advantage in developing a pipe-in-pipe system, just as in the case of pure hydrogen transport.

In order to simplify the nomenclature, it is decided to refer to the various pipe-in-pipe cases still in terms of the hydrogen fraction in the overall transported gas, despite the fact that it is no longer in blend form.

The analysis of the system under investigation can be divided into distinct steps.

First of all, the effects of varying the ratio between the diameters of the two pipes on the pressure trends of hydrogen and natural gas are investigated. The diameter of the outer tube Do is kept fixed (equal to 0.7 m) and that of the inner tube Di is changed. The subsequent objective is the identification of the optimal diameter ratio, which is identified as the one that yields the minimum pressure difference between the two gases at the walls of the internal pipe along its length. Considering the resulting diameter values, the power required to compress both hydrogen and natural gas is then computed. Finally, the relationship between the thickness of the FRP pipe wall and the permeation of hydrogen is investigated.

All considerations and results were analysed again for Scenarios A and B, as presented in the previous chapter.

7.2. Influence of diameter ratio

The first step of the analysis is to study how the variation in the ratio between the diameters of the two pipes affects the pressure drop for the two gases flowing in their respective sections. The analysed diameter ratios are ¼, ½ and ¾. The value of the outer pipe diameter is kept fixed at 0.7 m, limiting the analysis to hydrogen 'fractions' (with the meaning discussed in Section 7.1) of 50% and 80%.

For different values of the ratio between the diameters, different values of the hydraulic diameter are also obtained. The hydraulic diameter is used to calculate the pressure losses of natural gas within the annular space.

According to equation (7.1), the hydraulic diameter for the annular section between two pipes is exactly equal to the difference between the two diameters:

$$D_{h,ann} = D_o - D_i \tag{7.3}$$

Table 7.1 summarises the values of the diameters considered in the investigation:

Table 7.1 - Diameter values considered in the analysis

D_i/D_o	D_o [m]	D_i [m]	$D_{h,ann}$ [m]
¼	0.7	0.175	0.525
½	0.7	0.35	0.35
¾	0.7	0.525	0.175

7.2.1. Scenario A: p_{in} = 70 bar, p_{fin} = 50 bar

In the current scenario, an inlet pressure p_{in} of 70 bar and a minimum permissible pressure p_{fin} of 50 bar were considered for both fluids, analogous to what was done in Chapter 6 for the blend.

Table 7.2 lists the volumetric and energy flow rates used in the calculations for Scenario A, which are based on those of the Retrofit case for the blend transport shown in Table 6.8.

Table 7.2 - Volumetric and energy flow rate of H_2, NG and total (Scenario A)

	H_2 = 50%	**H_2 = 80%**
F_{tot} [Sm³/h]	245189	334973
F_{H2} [Sm³/h]	122594.5	267978.4
F_{NG} [Sm³/h]	122594.5	66994.6
$\dot{E}_{tot}$ [MWh/h]	1765	1639
$\dot{E}_{H2}$ [MWh/h]	412	900
$\dot{E}_{NG}$ [MWh/h]	1353	739

Pressure drop graphs for hydrogen fractions transported equal to 50% of the total flow rate and for the previously stated diameter ratios are shown in Figure 7.3. All the three polymer composite materials analysed in Chapter 3 with their respective roughness values are considered for the inner pipe, plotting results on the same graph.

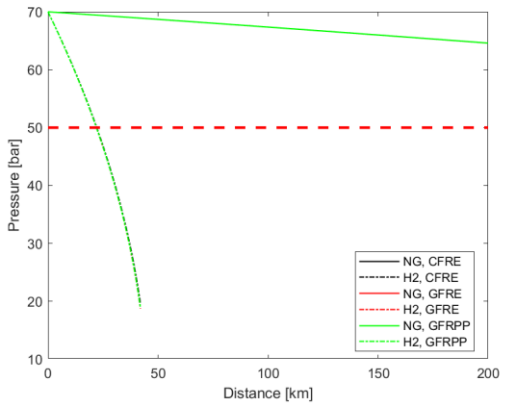

(a) Di/Do = ¼

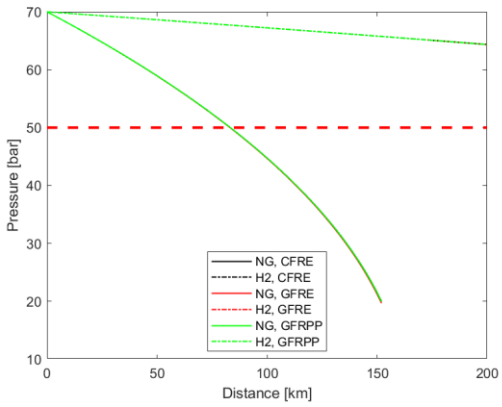

(b) Di/Do = ½

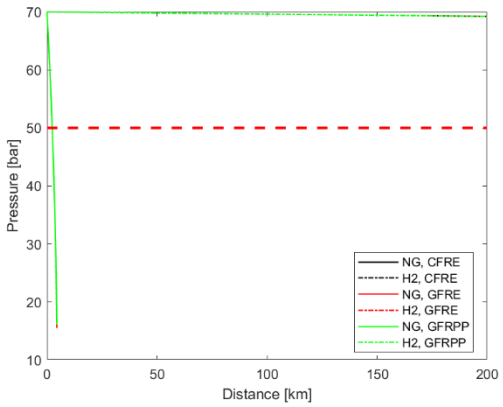

(c) Di/Do = ¾

Figure 7.3 - Pressure drop of H_2 and NG for different diameter ratios, 50% H_2 and inner tube made of CFRE, GFRE, GFRPP (Scenario A)

The curves for the three different materials are practically overlapping, making them difficult to distinguish. This suggests that, for the range of diameters considered in the analysis the varying roughness values have a negligible effect on the pressure losses.

For the same value of flow rate, if the diameter of the inner tube Di is ¼ of that of the outer tube Do, the hydrogen pressure falls much faster than that of natural gas. The opposite behaviour is observed for Di/Do equal to ¾.

Apart from the different density of the two fluids and the different roughness of the surfaces with which they are in contact, this is due to purely geometric reasons. In the first case, the hydraulic diameter $D_{h,ann}$, which characterises the section through which the natural gas flows, is greater than D_i, which is linked to the flow of hydrogen; in the second, the opposite is true.

Table 7.3 shows the distances at which a pressure of 50 bar is reached for each of the two gases for the three possible diameter pairs. Considering that the different materials yield similar performances, results for only GFRE are reported as example.

Table 7.3 - Distance at which p=50 bar for different diameter ratio and H_2=50% (Scenario A)

H_2 = 50%	**D_i/D_o = ¼**	**D_i/D_o = ½**	**D_i/D_o = ¾**
$L_{fin,H2}$ [km]	22	640	4510
$L_{fin,NG}$ [km]	650	84	2.4

If the idea being supported is to recompress the gas whenever the pressure reaches 50 bar, when Di/Do equal to ¼ (see Figure 7.3.a) natural gas is transported for 650 km before reaching this pressure and the hydrogen would have to be recompressed after 22 km only. The latter would require a very large number of compressor stations along the pipeline route. The same reasoning in reverse can be made for Di/Do equal to ¾ (see Figure 7.3.c), in which NG reaches 50 bar shortly after passing 2 km. The case where Di/Do = ½ (see Figure 7.3.b) is the one where the pressure drops for the two gases are more similar and the two distances at which the pressure goes to 50 bar are simultaneously more acceptable.

The same diagrams are also derived for hydrogen fractions equal to 80% of the total flow rate (see Figure 7.4).

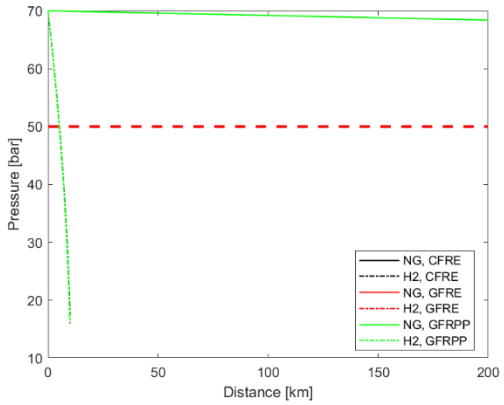

(a) Di/Do = ¼

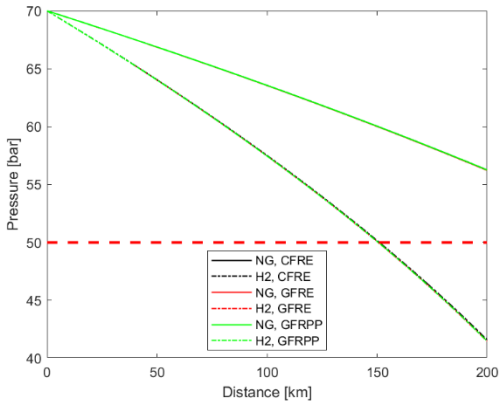

(b) Di/Do = ½

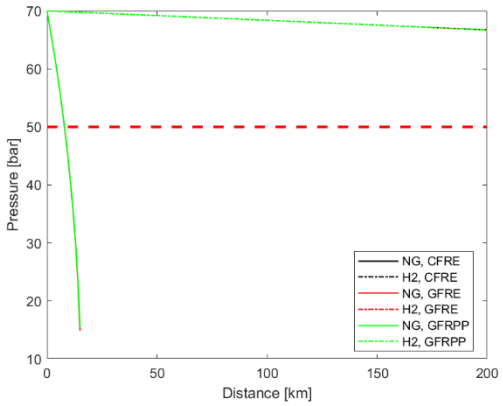

(c) Di/Do = ¾

Figure 7.4 - Pressure drop of H_2 and NG for different diameter ratios, 80% H_2 and inner tube made of CFRE, GFRE, GFRPP (Scenario A)

Even in the case of 80% H_2, the curves obtained by considering the three different material options for the smaller diameter pipe are practically overlapping and indistinguishable. The difference between the three roughness values is not significant enough to substantially impact the pressure losses.

The comments made for the case where the hydrogen flow rate is 50% of the total flow rate also apply here. For Di/Do = ¼ and Di/Do = ¾ the results are the opposite of each other: in the former the hydrogen pressure drops rapidly, in the latter the same fate befalls the natural gas. In these two situations, the large number of compressor stations required would make little sense, given the short distances at which the minimum pressure is reached (see Table 7.4).

Table 7.4 - Distance at which p=50 bar for different diameter ratio and H_2=80% (Scenario A)

H_2 = 80%	**D_i/D_o = ¼**	**D_i/D_o = ½**	**D_i/D_o = ¾**
$L_{fin,H2}$ [km]	5.2	152	1080
$L_{fin,NG}$ [km]	2120	276	8

Again, in the case where the inner tube is half the diameter of the outer tube, the two pressure drops are more similar and the distances involved are more reasonable.

By comparing the two tables Table 7.3 and Table 7.4, for the same ratio of diameters, the distance L_{fin} at which the minimum pressure p_{fin} of 50 bar is reached decreases when considering the case of carrying 80% H_2 compared to 50% H_2. The same reasoning applies to natural gas of course.

In conclusion, by increasing the Di/Do ratio, for the same percentage of hydrogen transported, the pressure drop of hydrogen decreases while that of natural gas increases.

If, on the other hand, for the same Di/Do ratio, the percentage of hydrogen (and thus its flow rate with respect to the total transported) is increased, the pressure drop of hydrogen decreases while that of natural gas increases. It is worth remembering that for 50% H_2 and 80% H_2 the flow rates are different.

In the following, only the results obtained considering a glass fibre-reinforced epoxy resin matrix (GFRE) as FRP will be reported, although calculations were also carried out for carbon fibre-reinforced epoxy resin and glass fibre-reinforced polypropylene (for which the roughness was measured at the RWTH University in Aachen, Germany).
This choice was made in order to avoid unnecessary repetition and can also be justified by the fact that the different roughness values are not excessively different and their influence on the friction factor and on the pressure drop in general is limited as shown by Figure 7.3 and Figure 7.4 , considering the large diameters being worked with.

Of all the possibilities, glass fibre-reinforced epoxy was decided upon because it will be the same material used in the subsequent search for hydrogen permeability through the inner tube. This choice was made based on the fact that the specimens tested for permeation measurement (see Chapter 4) are made of GFRE and CFRE, of which the former has better barrier properties [103] and a lower cost.

7.2.2. Scenario B: p_{in} = 50 bar, p_{fin} = 30 bar

The same procedure carried out for scenario A is repeated for scenario B. The volumetric and energy flow rates used in the calculations for Scenario B (see Table 7.5) are derived from the values in Table 6.10 for the corresponding hydrogen percentages.

Table 7.5 - Volumetric and energy flow rate of H_2, NG and total (Scenario B)

	H_2 = 50%	**H_2 = 80%**
F_{tot} [Sm³/h]	250919	342950
F_{H2} [Sm³/h]	125459.5	274360
F_{NG} [Sm³/h]	125459.5	68590
$\dot{E}_{tot}$ [MWh/h]	1806	1678
$\dot{E}_{H2}$ [MWh/h]	421	1342
$\dot{E}_{NG}$ [MWh/h]	1385	336

Results for a hydrogen share of 50% are summarised in Figure 7.5 and Table 7.6.

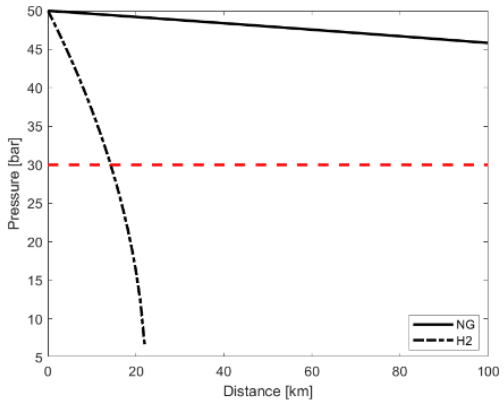

(a) Di/Do = ¼

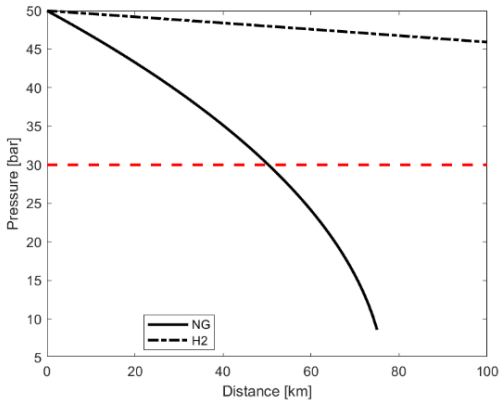

(b) Di/Do = ½

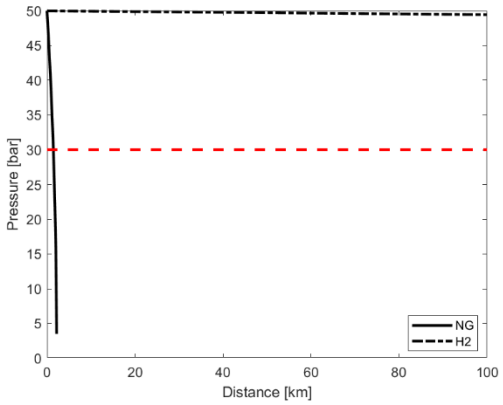

(c) Di/Do = ¾

Figure 7.5 - Pressure drop of H_2 and NG for different diameter ratios, 50% H_2 and inner tube made of GFRE (Scenario B)

Table 7.6 - Distance at which p=30 bar for different diameter ratio and H2=50% (Scenario B)

H_2 = 50%	**D_i/D_o = ¼**	**D_i/D_o = ½**	**D_i/D_o = ¾**
$L_{fin,H2}$ [km]	14.5	416	2925
$L_{fin,NG}$ [km]	395	51	1.45

Figure 7.6 and Table 7.7 describe what happens when the hydrogen fraction in the total gas transported is increased to 80%.

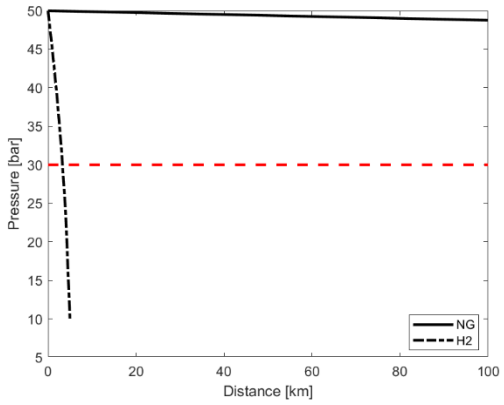

(a) Di/Do = ¼

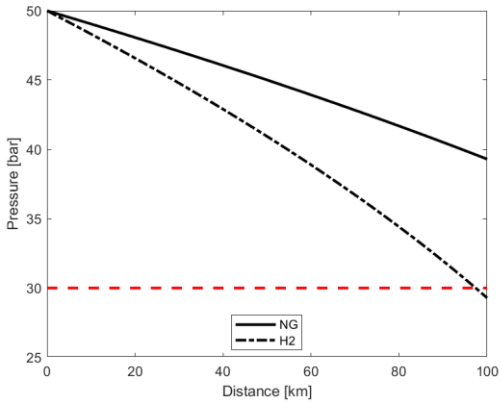

(b) Di/Do = ½

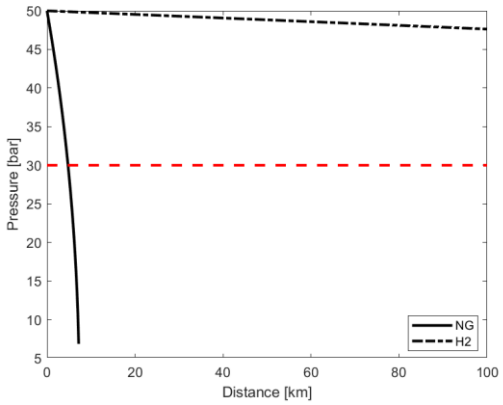

(c) Di/Do = ¾

Figure 7.6 - Pressure drop of H_2 and NG for different diameter ratios, 80% H_2 and inner tube made of GFRE (Scenario B)

Table 7.7 - Distance at which p=30 bar for different diameter ratio and H_2=80% (Scenario B)

H_2 = 80%	**D_i/D_o = ¼**	**D_i/D_o = ½**	**D_i/D_o = ¾**
$L_{fin,H2}$ [km]	3.4	100	700
$L_{fin,NG}$ [km]	1290	166	4.8

As expected, the same behaviour of scenario A is observed.

With the same diameter ratio, the higher the percentage of hydrogen, the more its pressure drops and thus $L_{fin,H2}$ decreases, as opposed to natural gas.

The same effect occurs as the ratio between the diameters of the two pipes increases, a percentage of hydrogen being fixed. The pressure drop of hydrogen increases and thus the $L_{fin,H2}$ at which it is recompressed decreases, as opposed to natural gas for which $L_{fin,NG}$ becomes larger.

7.2.3. Search for the optimum diameter ratio

From the previous analysis, it appears that an optimum ratio for diameters exists that minimize the pressure difference among the two gases. It makes it possible to recompress both gases at the same distance, and therefore at the same compressor stations, and to keep the number of compressor stations acceptable, in contrast to the Di/Do ratio of ¼ or ¾ which was exaggerated.

Furthermore, using such a value, the pressures on the two sides of the composite polymer inner tube being identical, minimizes the mechanical stress. Still remains the possibility of pressure fluctuations, caused for example by shutdown and restart of operation, changes in flow rate, etc., which are outside of the scope of this preliminary work. As far as the tightness of the external pipe is concerned, there would be no problem since it is being considered as part of the natural gas network and therefore already subject and certified to these pressure levels.

The optimum diameter ratio is determined by minimising the root mean square error (RMSE) relative to the difference between the pressures of hydrogen and natural gas on the two sides of the pipe along its length, considering zero as target value. The diameter ratio is varied in the region of ½, as it appeared from the previous step that this figure was closer to the optimum condition than ¼ and ¾, for both hydrogen percentages and in both scenarios.

The RMSE is defined as:

$$RMSE = \sqrt{\frac{\sum_{i=1}^{n}(x_i - \hat{x}_i)^2}{n}} = \sqrt{\frac{\sum_{i=1}^{n}(p_{H2,i} - p_{NG,i})^2}{n}} \tag{7.4}$$

where, in our case, x_i is the difference between the pressure of H_2 and that of NG at a given distance i along the pipe, $\hat{x}_i$ is zero (target value) and n is the number of distances at which this difference is evaluated.

A numerical search (by means of MATLAB tools) is made for the value of Di/Do such that the RMSE is closest to zero, representative of the situation in which the difference between the two pressures tends to be null.

7.2.3.1. Scenario A: p_{in} = 70 bar, p_{fin} = 50 bar

Figure 7.7 graphically represents the development of RMSE as a function of diameter ratio around ½, which is a value close to the optimum ratio as seen in Section 7.2.1.

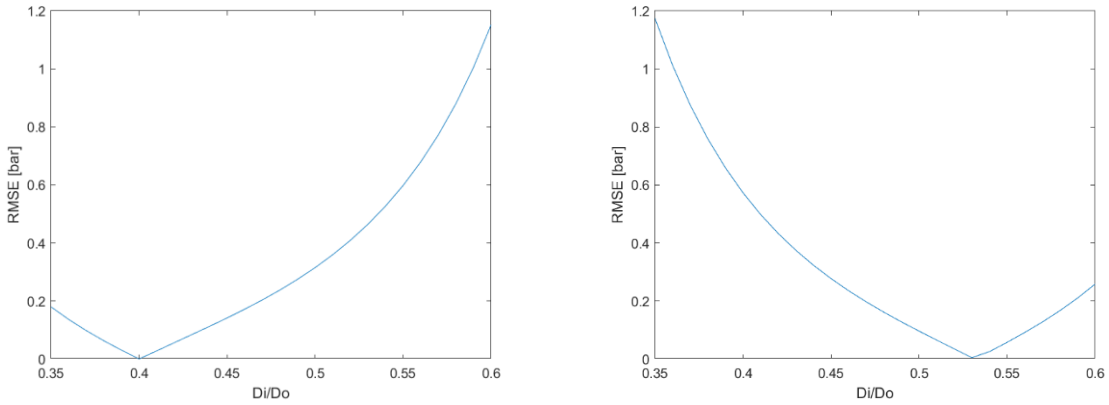

(a) H_2 = 50% (b) H_2 = 80%

Figure 7.7 - RMSE as a function of diameter ratio (Scenario A)

For the investigated cases, as Figure 7.7 and Table 7.8 show, the optimal diameter ratio that minimises the RSME results equal to 0.40 in the case where 50% of the transported gas is hydrogen and 0.53 when it constitutes 80% instead.

Table 7.8 - Optimum diameter ratio and consequent L_{fin} for 50% and 80% H_2 (Scenario A)

% H_2	$(Di/Do)_{opt}$	Do [m]	Di_{opt} [m]	L_{fin} [km]
50%	0.40	0.7	0.280	211
80%	0.53	0.7	0.371	200

7.2.3.2. Scenario B: p_{in} = 50 bar, p_{fin} = 30 bar

The results for scenario B are shown in Figure 7.8 and Table 7.9. It is observed that the optimal ratios are still 0.40 and 0.53 as in scenario A (see Figure 7.7 and Table 7.8).

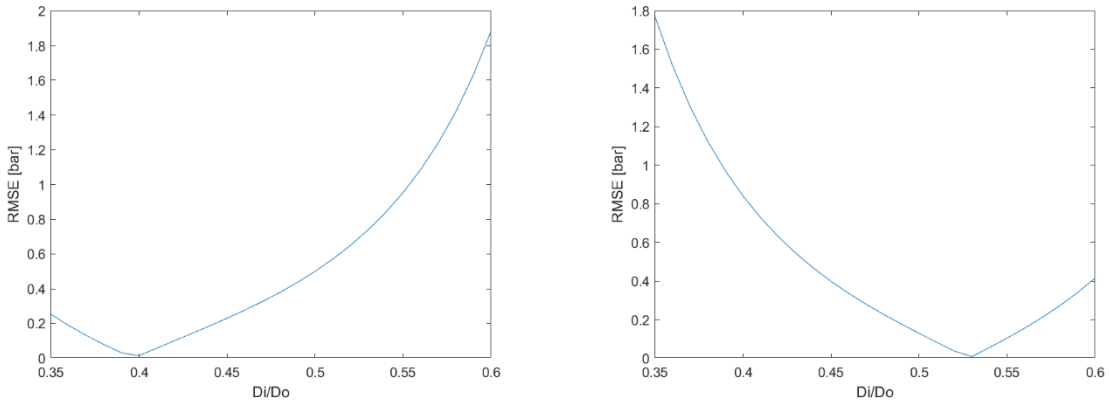

(a) H_2 = 50% (b) H_2 = 80%

Figure 7.8 - RMSE as a function of diameter ratio (Scenario B)

Table 7.9 - Optimum diameter ratio and consequent L_{fin} for 50% and 80% H_2 (Scenario B)

% H_2	**$(Di/Do)_{opt}$**	**Do [m]**	**Di_{opt} [m]**	**L_{fin} [km]**
50%	0.40	0.7	0.280	128
80%	0.53	0.7	0.371	121

Overall, results show that the optimal diameter ratio depends solely on the proportion of hydrogen to natural gas flow rate transported in the pipe-in-pipe system, since the optimal values are the same for scenarios A and B. Therefore, it is not influenced by pressure.

As expected, the optimal diameter ratio is higher as the hydrogen flow rate increases. For a hydrogen percentage of 50%, the optimum value is 0.40, while for a percentage of 80% it rises to 0.53. Since a fixed larger pipe diameter has been considered, the diameter of the FRP inner pipe is the only one which is subject to variation in accordance with this ratio. Accordingly, wanting to impose the same pressure drop for hydrogen and natural gas, as the amount of H_2 transported increases relative to that of NG, a larger diameter of the inner tube is required to accommodate the higher flow rate.

7.3. Compression power

In order to complete the analysis of gas transport through the pipe-in-pipe system from an energy point of view, the compression power required to bring the downstream pressure to the upstream values at a compressor station is computed.

As equation (7.5) states, the compressor mechanical power $P_{mecc,c}$ is calculated by multiplying the isentropic work of compression $l_{c,is}$, which is a specific work, by the volumetric flow F and finally dividing by the adiabatic efficiency of the compressor η_{ad}.

$$P_{mecc,c} = F \cdot \frac{l_{c,is}}{\eta_{ad}} \tag{7.5}$$

with:

$$l_{c,is} = \frac{R}{MM} \cdot \frac{Z_{avg} \cdot T_{in}}{\theta} \cdot \left(\left(\frac{p_{outlet}}{p_{inlet}} \right)^{\theta} - 1 \right) \tag{7.6}$$

$$\theta = \frac{\gamma - 1}{\gamma} \tag{7.7}$$

$$\gamma = \frac{C_p}{C_v} \tag{7.8}$$

where $l_{c,is}$ is the isentropic work of compression, η_{ad} the adiabatic efficiency of the compressor (usually around 70-80% for large devices), C_p and C_v the specific heat capacity at constant pressure and constant volume, respectively.

R is the gas constant, MM the molar weight of the gas and Z_{avg} the average compressibility factor.

The gas transmission network mainly relies on centrifugal compressors, which are typically characterised by an adiabatic efficiency of 80%.

The factor θ is an average of inlet and outlet conditions and it is a function of the gas we are dealing with. It depends in turn on γ (see equation (7.7)) which the ratio between specific heat at constant pressure C_p and specific heat at constant volume C_v.

The power thus calculated is mechanical. Actually, the compressors on the grid are often driven by a gas turbine that consumes part of the compressed gas (‰). Recently, the use of electrically-driven compressors has been proposed to exploit renewable electricity. Consequently, for this analysis we'll compare only the mechanical power, neglecting the actual driver. This allows anyway a comparison of energy requirements of the different solutions.

This analysis is performed considering that the ratio between the diameters is the one recognised as "optimum" in the previous chapter. Therefore, both hydrogen and natural gas have the same pressures at the inlet and outlet of the compressor, p_{inlet} and p_{outlet} respectively.

7.3.1. Scenario A: p_{in} = 70 bar, p_{fin} = 50 bar

Following the above formulas, all the values of the mechanical compression powers for the two individual gases and the overall power, given by the sum of the previous ones, are calculated, together with those of the blends with the corresponding hydrogen percentage, with inlet and outlet pressures held constant (see Table 7.10).

Given the existing conditions in this scenario, p_{inlet} = 50 bar and p_{outlet} = 70 bar.

Table 7.10 - Mechanical compression power of pipe-in-pipe and corresponding blend (Scenario A)

% H_2	**50%**	**80%**
P_{mecc,c_H2} [MW]	0.139	0.303
P_{mecc,c_NG} [MW]	0.176	0.096
P_{mecc,c_PIP} [MW]	0.315	0.399
P_{mecc,c_BLEND} [MW]	0.269	0.366
$\dot{E}_{tot}$ [MW]	1764.683	1639.322

Looking at the values for individual gases, for the same flow rate (case where H_2 = 50%) compressing natural gas is more power-intensive than compressing hydrogen. In the case of 80% H_2, the opposite holds true, and the power required to compress hydrogen is higher than that needed to compress natural gas.

As for the total power consumed by the compressor for the two gases, it is higher in the case with a higher hydrogen content. Care must be taken because the energy transported decreases when moving from 50% to 80% H_2.

In fact, the mechanical power consumed for compression goes from being 0.018% of the energy flow to 0.024%, resulting in less favourable conditions (see Table 7.11).

It can be observed that the power required to compress the blend is slightly lower compared to the pipe-in-pipe case, at the same hydrogen flow rate. This is further

supported by the data in Table 7.11. It can be seen that the difference is limited to a few thousandths of a percent. A visual representation is given in Figure 7.9.

Table 7.11 - Ratio between power consumed for compression and energy flow rate for pipe-in-pipe and blend cases (Scenario A)

% H_2	**50%**	**80%**
P_{mecc,c_PIP} / $\dot{E}_{tot}$	0.018%	0.024%
P_{mecc,c_BLEND} / $\dot{E}_{tot}$	0.015%	0.022%

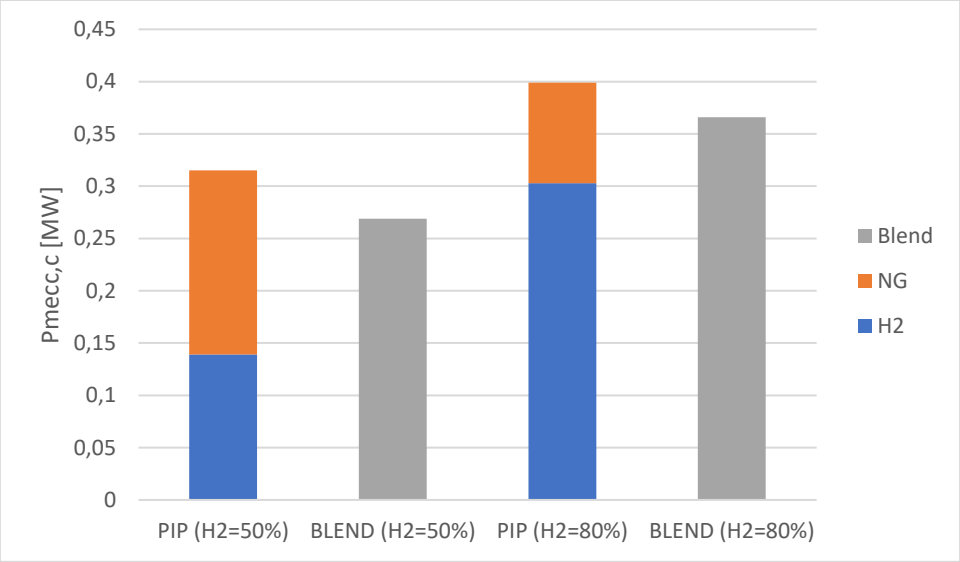

Figure 7.9 - Compression power of blend and pipe-in-pipe system for 50% and 80% H_2 (Scenario A)

7.3.2. Scenario B: p_{in} = 50 bar, p_{fin} = 30 bar

In the case of scenario B, p_{inlet} = 30 bar and p_{outlet} = 50 bar need to be considered.

The results obtained for scenario B are shown in Table 7.12, together with the values of mechanical power consumed for the compression of the natural gas-hydrogen blends having the same hydrogen percentage.

Table 7.12 - Mechanical compression power of H_2, NG and total (Scenario B)

% H_2	**50%**	**80%**
P_{mecc,c_H2} [MW]	0.217	0.474
P_{mecc,c_NG} [MW]	0.219	0.120
P_{mecc,c_PIP} [MW]	0.436	0.594
P_{mecc,c_BLEND} [MW]	0.390	0.558
$\dot{E}_{tot}$ [MW]	1805.924	1678.361

These results confirm the behaviour observed for scenario A. Indeed, considering that the flow rates vary from the case with 50% hydrogen to the one with 80% hydrogen, the total compression power is higher in the second case compared to the first one, contrary to the energy flow rate which is lower, thus resulting in an unfortunate increase in their ratio (see Table 7.13).

Comparing the pipe-in-pipe case with the blend case at the same transported hydrogen flow rate, as seen in scenario A, the power consumed by the compressor is slightly higher in the former case and the ratio with the energy flow rate is therefore larger (see Table 7.13). This can be easily visualized in Figure 7.10

Table 7.13 - Ratio between power consumed for compression and energy flow rate for pipe-in-pipe and blend cases (Scenario B)

% H_2	**50%**	**80%**
P_{mecc,c_PIP} / $\dot{E}_{tot}$	0.024%	0.035%
P_{mecc,c_BLEND} / $\dot{E}_{tot}$	0.022%	0.033%

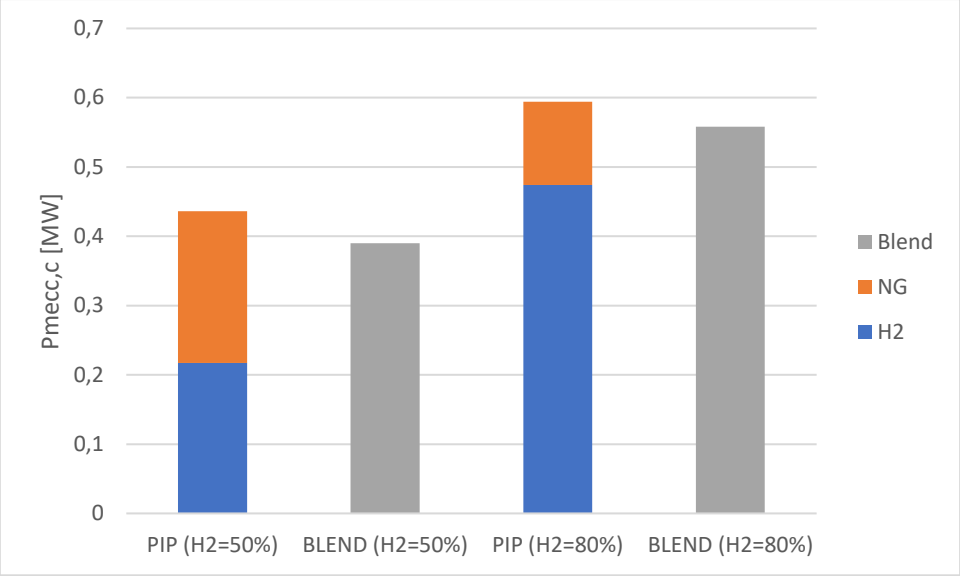

Figure 7.10 - Compression power of blend and pipe-in-pipe system for 50% and 80% H_2 (Scenario B)

If we now compare the two scenarios, for the same proportion of F_{H2} to F_{NG} (and therefore same hydrogen percentage), we see that the ratio between power consumed by the compressor and transported energy increases for scenario B, where the pressure downstream and upstream of the compressor is lower than for scenario A.

Consequently, working under the conditions set for scenario A is more energy efficient.

7.4. Hydrogen permeation through the FRP inner pipe

The addition of fibres to a polymer matrix leads to changes in hydrogen permeation and the processes in the case of polymer composite materials are more complex than in a plain polymer. Hydrogen passing through a composite material experiences fibres as an additional obstacle in its path.

The scientific literature is lacking data on hydrogen permeability in FRP materials.

One theoretical attempt to describe permeation through composite materials is that developed by Takayanaki, according to which permeation consists of two contributions in two different sub-areas. In one sub-area permeation occurs through the matrix alone, in the other it occurs through matrix and fibres (see Figure 7.11) [103].

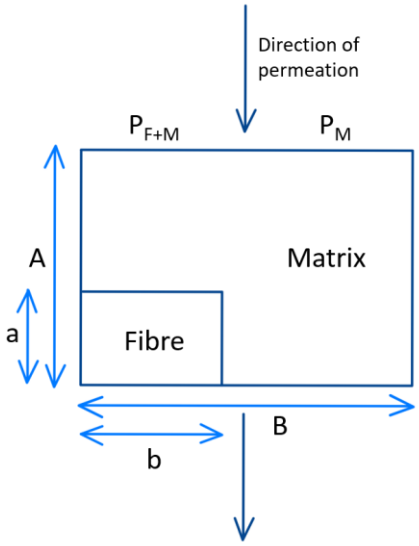

Figure 7.11 – Visual representation of Takayanaki model for permeation in FRP

The permeability of the inhomogeneous part of the material is calculated by relying on a model concerning permeation through a system consisting of two parallel layers [103]. Considering for the individual layers thicknesses d_1 and d_2 and permeabilities P_1 and P_2, and for the system an overall thickness d and permeability P, it holds that:

$$\frac{P}{d} = \left(\frac{d_1}{P_1} + \frac{d_2}{P_2}\right)^{-1} \tag{7.9}$$

According to Takayanaki model, the overall permeability can be determined using the formula (7.9) referring to the simplified structure of the composite material in Figure 7.11.

$$P = (1 - \lambda)\, P_M + \lambda \left(\frac{\phi}{P_F} + \frac{1 - \phi}{P_M}\right)^{-1} \tag{7.10}$$

where λ is the ratio between the size of the area assigned to the fibre in the direction of permeation a and that of the composite A in the same direction, while ϕ is the ratio between the size of the area assigned to the fibre b and the composite B in the direction orthogonal to that of permeation. The product between ϕ and λ corresponds to the volume fraction of fibres f_v, namely the ratio of the volume occupied by the fibres and that of the composite, and they are used as weights in this mixing rule.

However, experimental measurements have revealed an exponential dependence of the permeability on the fibre volume fraction f_v, and thus on a single parameter [103]. Therefore, plotting the natural logarithm of P as a function of the volumetric fibre fraction results in a straight line with slope s, depending on the composite structure (see Figure 7.12).

The following equation hold [103]:

$$P = P_M \, e^{-s f_v} \tag{7.11}$$

For a fibre volume fraction equal to unity, the permeability of the fibre material is:

$$lnP_F = lnP_M - s \tag{7.12}$$

By correlating equations (7.11) and (7.12), the permeation coefficient is expressed as:

$$P = {P_F}^{f_v} \, . \, {P_M}^{(1-f_v)} \tag{7.13}$$

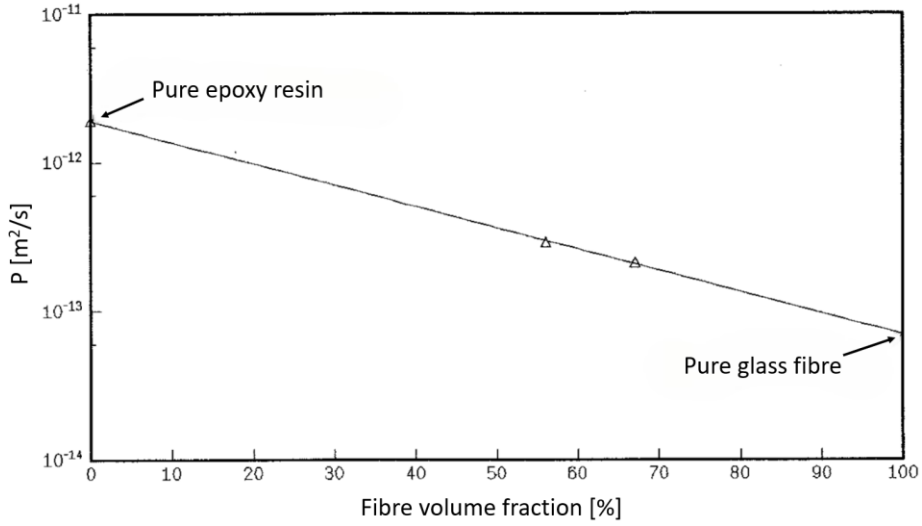

Figure 7.12 - Helium permeability of GFEP as a function of fibre volume fraction [103]

Carbon and glass fibres are two common types of fibres. Carbon fibres are characterised by a more energy-intensive production process, and they are overall more expensive. In addition, the barrier properties for gas permeation of glass fibres exceed those of carbon fibres [103].

Having made these considerations, the following analysis focuses on the use of glass fibres inside an epoxy resin matrix.

A value of 60% is selected as the volume fraction of fibres, based on values used at Institut für Textiltechnik (ITA) of the RWTH Aachen University, in Germany.

The hydrogen permeability of the selected material (fibre volume fraction $f_v = 60\%$) is determined through interpolation, knowing the hydrogen permeability coefficient of the epoxy resin (f_v = 0%) and that of a glass fibre-reinforced composite having f_v = 56% from the literature [103], and it is shown in Table 7.14.

Table 7.14 - Permeability of glass fibre, epoxy resin and glass fibre-reinforced epoxy for 60% fibre volume fraction [103]

Fibre volume fraction	**$P_{GFRE,\ 56\%}$ [mol/(m.s.MPa)]**	**P_{epoxy} [mol/(m.s.MPa)]**	**$P_{GFRE,\ 60\%}$ [mol/(m.s.MPa)]**
60%	$1.27 \cdot 10^{-10}$	$5.70 \cdot 10^{-10}$	$1.14 \cdot 10^{-10}$

For the calculation of permeation, both adsorption and diffusion must be considered.

Fick's first law enables the calculation of diffusion in the case of a stationary regime such as the one considered here. The transient in the diffusion is not taken into account but only the steady state, since the boundary conditions are constant within a pipeline.

The molar flux through a membrane can be expressed through the first Fick's law:

$$j = \frac{\dot{n}}{A} = -D\,\frac{\partial c}{\partial x} \tag{7.14}$$

where ṅ is the molar flow, A is the area through which the gas diffuses, D is the diffusion coefficient and $\frac{\partial c}{\partial x}$ is the derivative of the molar concentration along the diffusion direction x.

In the presence of concentration variation over time, Fick's second law applies:

$$\frac{\partial c}{\partial t} = D\,\frac{\partial^2 c}{\partial x^2} \tag{7.15}$$

In the case of steady state, such as the one considered here, the time derivative cancels out $\left(\frac{\partial c}{\partial t} = 0\right)$ and consequently one obtains:

$$\frac{\partial^2 c}{\partial x^2} = 0 \tag{7.16}$$

By integrating and substituting in the steady state flux equation, it is possible to express the molar flow through a membrane in this way:

$$\dot{n} = A\,D\,\frac{c_1 - c_2}{d} \tag{7.17}$$

where c_1 and c_2 are the membrane inlet and outlet concentrations respectively and d is the membrane thickness.

To derive the equation for permeation through a pipe, the volume shown in Figure 7.13 is chosen as the reference volume, the length of which is L. The surface involved in the diffusion process is $2\pi rL$.

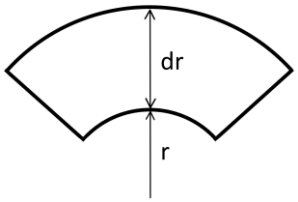

Figure 7.13 - Reference volume to derive the formula for permeation through a pipe

The molar flow through the cylinder of radius r can be expressed as:

$$\dot{n}_r = -D\ 2\pi r L\ \frac{dc}{dr} \tag{7.18}$$

and the one through the cylinder of radius $r + dr$ is:

$$\dot{n}_{r+dr} = \dot{n}_r - 2\pi L D\ \frac{d}{dr}\left(r\ \frac{dc}{dr}\right) dr \tag{7.19}$$

In the steady state equation and equation must be equal, and from this condition we obtain:

$$\frac{d^2c}{dr^2} + \frac{1}{r}\frac{dc}{dr} = 0 \tag{7.20}$$

Proceeding now with integration, placing the concentration at the inner radius r_1 equal to c_1 and the outer radius r_2 equal to c_2, and substituting into the molar flow equation, it results that:

$$\dot{n}_r = D\ 2\pi L\ \frac{c_1 - c_2}{\ln\left(\frac{r_2}{r_1}\right)} \tag{7.21}$$

The concentration of the diffusing species at the surface of the diffusion barrier is related to the pressure of that species by the solubility coefficient S [104], [105].

In the case of diffusion of a gas whose molecular form does not change due to dissolution in the material through which it moves, such as hydrogen H_2 through polymeric materials, it is valid that:

$$c = S\ p \tag{7.22}$$

Instead Sievert's law is valid, for instance, for the diffusion of molecular hydrogen through a metal film, which only occurs after its dissociation into monoatomic hydrogen:

$$c = S\ p^{\frac{1}{2}} \tag{7.23}$$

For the following calculations, equation (7.22) is considered.

The final formula for permeation in the case of a plate is:

$$\dot{n} = D\ S\ A\ \frac{p_1 - p_2}{d} \tag{7.24}$$

and in the case of pipes is:

$$\dot{n} = D\ S\ 2\ \pi\ L\ \frac{p_1 - p_2}{\ln\left(\frac{r_2}{r_1}\right)} \tag{7.25}$$

Where p_1 and p_2 are the partial pressures on the two sides of the pipe wall and r_1 and r_2 are the internal and external radii.

Writing the permeability P as:

$$P = D\ S \tag{7.26}$$

the expression of the molar flow of a gas through a pipe wall is obtained:

$$\dot{n} = P\ 2\ \pi\ L\ \frac{p_1 - p_2}{\ln\left(\frac{r_2}{r_1}\right)} \tag{7.27}$$

Hydrogen permeation through the entire length of the FRP pipe as a function of its thickness is calculated for both scenarios. Pressures along the pipe and pipe length are considered equal to those obtained for the optimal diameter ratios determined in Section 7.2.3.

7.4.1. Scenario A: p_{in} = 70 bar, p_{fin} = 50 bar

Permeation flow is calculated over a length of 211 km in the 50% hydrogen case and 200 km in the 80% case (see Table 7.8) for different values of FRP pipe thickness, considering the range 1-20 mm. The results are reported graphically in Figure 7.14.

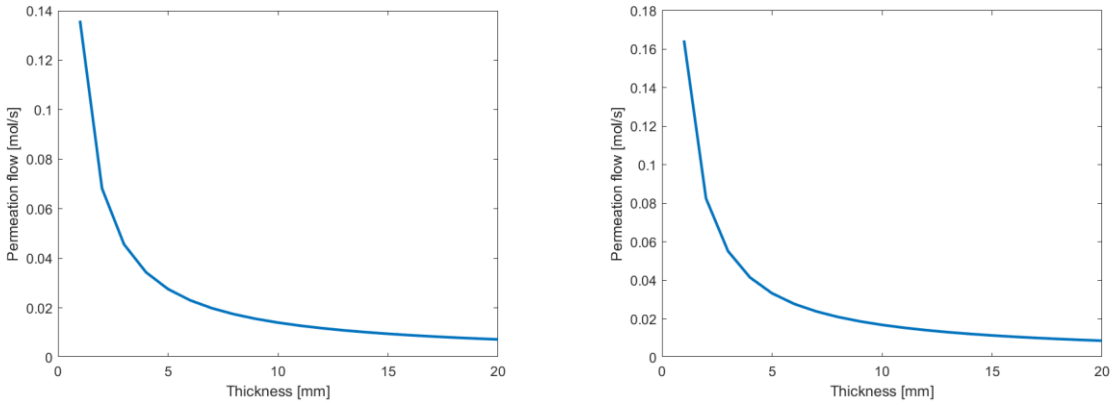

(a) H_2 = 50% (b) H_2 = 80%

Figure 7.14 - Permeation flow as a function of wall thickness (Scenario A)

The permeation flux decreases as the pipe thickness increases. For thicknesses approaching zero, permeation tends to infinity, while for increasingly larger values it drops towards zero.

Comparing the 50% H_2 and the 80% H_2 cases, the two differ in the length of the pipe and the value of the FRP pipe diameter. The overall result of these differences results in a greater amount of hydrogen permeated in the unit time for the 80% H_2 case.

In both the 50% H_2 and the 80% H_2 cases, the permeation flow reaches a plateau at a thickness of approximately 10 mm. For greater thicknesses, the decrease in permeation as the thickness itself increases becomes negligible, and thus there would be no advantage to working with thicker walls from the perspective of limiting permeation.

Higher thicknesses may still be required to meet mechanical needs. Indeed, it should be noted that the case corresponding to the optimum diameter ratio is characterised by a zero pressure difference between the two sides of the inner pipe wall.

Using the equation of state for real gases and the higher heating value of hydrogen, the permeated hydrogen moles can be converted in terms of volume and energy (see equations (7.28) and (7.29)).

$$V = \frac{zNRT}{p} \tag{7.28}$$

$$E = HHV \cdot V \tag{7.29}$$

The results of molar, volume and energy flow of hydrogen for a wall thickness of 10 mm are reported in Table 7.15.

Considering that the permeation flow that occurs with a thickness of 1 mm for the 50% H_2 case is 0.1360 $\frac{mol}{s}$ and for 80% H_2 is 0.1646 $\frac{mol}{s}$, using a thickness of 10 mm reduces the number of moles permeated per unit time by almost 90%.

Table 7.15 - Molar, volumetric and energy flow for 10 mm thickness of permeated hydrogen (Scenario A)

Thickness [mm]	**% H_2**	**Molar flow [mol/s]**	**Volume flow [m³/s]**	**Energy flow [MW]**
10	50%	0.0140	$5.0064 .10^{-6}$	0.0036
	80%	0.0169	$6.0142 .10^{-6}$	0.0044

The hydrogen permeation flow data are then used to determine the contamination of the natural gas flowing in the annular space between the two tubes.

The amount of hydrogen permeated throughout the pipe is interpreted as injection into the natural gas flowing with a flow rate equal to that used in Section 6.2. The composition of the gas at the exit of the pipe is then assessed. An illustration of the injection model is reported in Figure 7.15.

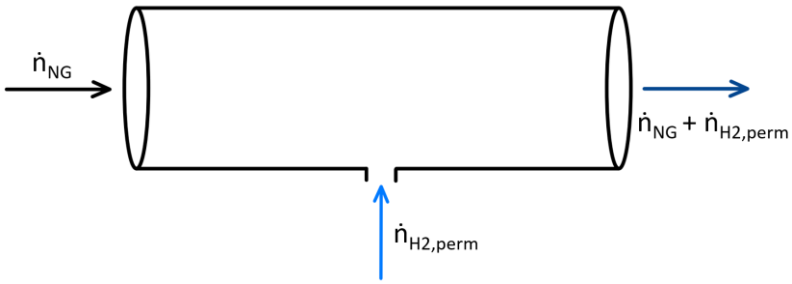

Figure 7.15 - Model of permeated hydrogen injection into the annulus

For convenience, we denote $\dot{n}_{H2}$ as the molar flow of hydrogen and $\dot{n}_{NG}$ as that of natural gas. The hydrogen fraction at the tube outlet is evaluated as:

$$ppm_{H2,out} = \frac{\dot{n}_{H2,perm}}{\dot{n}_{H2,perm} + \dot{n}_{NG}} \tag{7.30}$$

Table 7.16 - Molar flow of permeated hydrogen, of natural gas and outlet hydrogen fraction (Scenario A)

% H_2	**$\dot{n}_{H2,perm}$ [mol/s]**	**$\dot{n}_{NG}$ [mol/s]**	**$ppm_{H2,out}$**
50%	0.0140	$1.4439 \cdot 10^4$	0.970
80%	0.0169	$7.8905 \cdot 10^3$	2.142

It is immediately noticeable that the fraction of hydrogen permeate in natural gas is very small (see last column of

Table 7.16) and therefore the quality of natural gas is unaffected, remaining compliant with typical grid standards.

7.4.2. Scenario B: p_{in} = 50 bar, p_{fin} = 30 bar

For the calculation of permeated hydrogen moles in scenario B, pipelines of length 128 km and 121 km for the case with 50% and 80% hydrogen respectively, obtained with Di = Di_{opt} (see Table 7.9), and thicknesses ranging from 1 mm to 20 mm are considered. Results are reported in Figure 7.16.

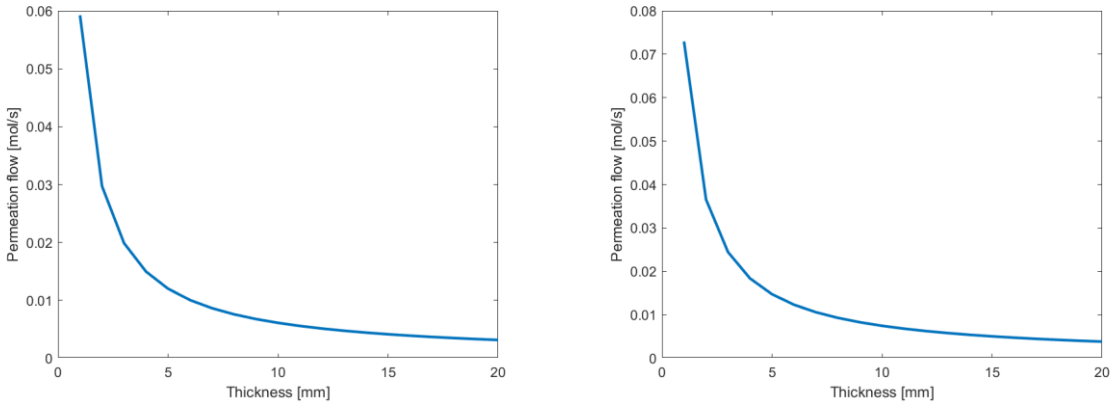

(a) H_2 = 50% (b) H_2 = 80%

Figure 7.16 - Permeation flow as a function of wall thickness (Scenario B)

As in the previous scenario, a plateau is reached at 10 mm. This behaviour is observed for both 50% hydrogen and 80% hydrogen transport.

Table 7.17 shows the molar, volume and energy flow values obtained for a wall thickness of 10 mm.

Table 7.17 - Molar, volume and energy flow of permeated hydrogen for 10 mm thickness (Scenario B)

Thickness [mm]	**% H_2**	**Molar flow [mol/s]**	**Volume flow [m^3/s]**	**Energy flow [MW]**
10	50%	0.0061	$3.0164 \cdot 10^{-6}$	0.0015
	80%	0.0075	$3.6871 \cdot 10^{-6}$	0.0018

For thickness equal to 10 mm, a hydrogen flow through the tube is obtained equal to approximately 10% both in the case of 50% H_2 and 80% H_2 with respect to the value for 1 mm (0.0592 $\frac{mol}{s}$ and 0.0729 $\frac{mol}{s}$, respectively).

For the calculation of the contamination of natural gas by hydrogen, flow rates were used, which are derived from the values in Table 6.10.

The flow rate of natural gas when the hydrogen transported is 50% of the total gas is $1.2545 \cdot 10^5$ $\frac{Sm^3}{h}$, while it is $6.8590 \cdot 10^4$ $\frac{Sm^3}{h}$ when the hydrogen rises to 80%.

Table 7.18 - Molar flow of permeated hydrogen, of natural gas and outlet hydrogen fraction (Scenario B)

% H_2	**$\dot{n}_{H2,perm}$ [mol/s]**	**$\dot{n}_{NG}$ [mol/s]**	**$ppm_{H2,out}$**
50%	0.0061	$1.4776 \cdot 10^4$	0.413
80%	0.0075	$8.0784 \cdot 10^3$	0.928

The number of moles of hydrogen that permeates is so much less than the number of moles of natural gas into which it is 'injected' that the quality of the latter can be assumed to be unaffected. The fractions of H_2 at the pipe outlet are in fact less than 1 ppm (see Table 7.18).

7.5. Summary of pipe-in-pipe results

The pipe-in-pipe case has been studied for two distinct scenarios, denoted as A and B, which differ in their maximum and minimum operational pressure values (see Table 7.19). In both scenarios, the external diameter is kept constant at 0.7 meters, and the cases with hydrogen representing 50% and 80% of the total gas flow rate are analysed.

Three materials have been investigated for the inner pipe, all of which are composite polymeric materials: carbon fibre-reinforced epoxy resin (CFRE), glass fibre-reinforced epoxy resin (GFRE), and glass fibre-reinforced polypropylene (GFRPP). The respective roughness values are those experimentally determined in Chapter 3.

Table 7.19 - Initial and final pressures and external diameter for scenarios A and B

	Scenario A	**Scenario B**
p_{in} [bar]	70	50
p_{fin} [bar]	50	30
Do [m]	0.7	0.7

The total flow rates are the same as those observed for the corresponding hydrogen percentage in the 'Retrofit' case discussed in Chapter 6. These rates have been divided into a component related to hydrogen within the inner pipe and another pertaining to natural gas within the annular section, which have been reported in Table 7.20.

Table 7.20 - Volume and energy flow rate of H_2, NG and total for scenarios A and B

	Scenario A		**Scenario B**	
% H_2	**50%**	**80%**	**50%**	**80%**
F_{tot} [Sm^3/h]	245189	334973	250919	342950
F_{H2} [Sm^3/h]	122594.5	267978.4	125459.5	274360
F_{NG} [Sm^3/h]	122594.5	66994.6	125459.5	68590
$\dot{E}_{tot}$ [MWh/h]	1765	1639	1806	1678
$\dot{E}_{H2}$ [MWh/h]	412	900	421	1342

$\dot{E}_{NG}$ [MWh/h]	1353	739	1385	336

7.5.1. Influence of diameter ratio

The influence of the ratio between the diameter of the inner pipe and the outer pipe on the pressure behaviour of hydrogen and natural gas in the two distinct sections has been investigated and the results are summarised in Table 7.21.

The reported results are exclusively for the case in which the inner pipe is made of GFRE since it has been confirmed that the varying roughness of the three materials had a negligible influence on the pressure drop and it will be considered in a subsequent analysis on permeation.

Table 7.21 - Distance of compressor stations for H_2 and NG for Di/Do = ¼, ½ and ¾ for scenarios A and B

Scenario	% H_2	D_i/D_o	$L_{fin,H2}$ [km]	$L_{fin,NG}$ [km]
A	**50%**	¼	22	650
		½	640	84
		¾	4510	2.4
	80%	¼	5.2	2120
		½	152	276
		¾	1080	8
B	**50%**	¼	14.5	395
		½	416	51
		¾	2925	1.45
	80%	¼	3.4	1290
		½	100	166
		¾	700	4.8

At a constant hydrogen percentage, as the ratio between the inner and outer diameters of the pipe increases, the pressure drops for hydrogen and natural gas exhibit opposite trends: the former decreases, while the latter increases (resulting in the corresponding increase and decrease in the distance to reach the minimum pressure). This behaviour arises from the fact that increasing this diameter ratio, with the outer pipe diameter held constant, provides more space for hydrogen flow and narrows the passage for natural gas. Focusing on hydrogen, the L_{fin} distances obtained for diameter ratios of ½ and ¾ are approximately 30 and 200 times that of Di/Do = ¼, respectively.

Keeping in mind that two different hydrogen percentages correspond to two different flow rates since they relate to different values of the "Retrofit" case seen in Chapter 6, if a fixed Di/Do ratio is considered the pressure drop for hydrogen is 4 times higher in the 50% H_2 case than in the 80% H_2 case, while that of natural gas is approximately one-third.

The "optimum" diameter ratio of the two pipes has been identified as the one at which the pressure drops on both sides of the inner pipe are equal. For both scenarios, the same value was found. This ratio equals 0.40 for 50% H_2 and 0.53 for 80% H_2, and it solely depends on the ratio between hydrogen and natural gas flow rates (see Table 7.22).

Table 7.22 - Optimum diameter ratio and corresponding compressor station distance for scenarios A and B

Scenario	% H_2	$(Di/Do)_{opt}$	Do [m]	Di_{opt} [m]	L_{fin} [km]
A	**50%**	0.40	0.7	0.280	211
	80%	0.53	0.7	0.371	200
B	**50%**	0.40	0.7	0.280	128
	80%	0.53	0.7	0.371	121

In the case of 80% H_2, the diameter of the inner pipe at which hydrogen and natural gas pressures are equal, while keeping the outer diameter constant, is larger compared to the 50% H_2 case. This is due to the higher proportion between the flow rate of H_2 and NG in the former case compared to the latter.

7.5.2. Compression power

Table 7.24 summarises the values of mechanical power required for compressing the two separate gases from p_{inlet} to p_{outlet} defined in Table 7.23, as well as the total power

obtained by summing these values. These figures are then compared with the compression power of the blend having the same hydrogen percentage as the pipe-in-pipe case and the corresponding energy flow rate.

Table 7.23 - Inlet and outlet pressures at the compressor stations for scenarios A and B

	Scenario A	**Scenario B**
p_{inlet} [bar]	50	30
p_{outlet} [bar]	70	50

Table 7.24 - Mechanical power for compression in pipe-in-pipe and blend case for scenarios A and B

	Scenario A		**Scenario B**	
% H_2	**50%**	**80%**	**50%**	**80%**
P_{mecc,c_H2} [MW]	0.139	0.303	0.217	0.474
P_{mecc,c_NG} [MW]	0.176	0.096	0.219	0.120
P_{mecc,c_PIP} [MW]	0.315	0.399	0.436	0.594
P_{mecc,c_BLEND} [MW]	0.269	0.366	0.390	0.558
$\dot{E}_{tot}$ [MW]	1764.683	1639.322	1805.924	1678.361

In the case where the transported gas consists of 50% hydrogen, the power to compress H_2 is lower than that for NG. However, in the case of 80%, the situation is reversed. The ratio between power consumed for compression and energy flow rate increases within the same scenario (characterized by the same inlet and outlet pressures) when going from 50% H_2 to 80% H_2, and it also increases when transitioning from scenario A to scenario B, where the characteristic pressures are lower. Furthermore, both for 50% H_2 and 80% H_2, the corresponding blend case requires less power for compression, as also shown in relation to the energy flow rate in Table 7.25.

Table 7.25 - Compression power of pipe-in-pipe and blend case for scenarios A and B

	Scenario A		**Scenario B**	
% H_2	**50%**	**80%**	**50%**	**80%**
P_{mecc,c_PIP} / $\dot{E}_{tot}$	0.018%	0.024%	0.024%	0.035%
P_{mecc,c_BLEND} / $\dot{E}_{tot}$	0.015%	0.022%	0.022%	0.033%

Therefore, compressing the two gases in the pipe-in-pipe case is slightly more energy-intensive compared to the corresponding blend case, but in both cases the power consumed is still far less than the amount of energy transported and the OPEX (Operational Expenditures) are not significantly influenced by the transition from transporting the blend to the pipe-in-pipe system. On the contrary, the CAPEX (Capital Expenditures) are definitely affected. When comparing the distances between compressor stations in the blend case (see Table 6.14) and the pipe-in-pipe case (see Table 7.22), it is evident that in the second case, the distances are much shorter, which leads to a higher number of compressor stations.

7.5.3. Hydrogen permeation through the FRP inner pipe

Using a theoretical model concerning permeation in composite materials and reprocessing literature data, a study on hydrogen permeation through GFRE has been conducted. A fibre volume fraction of 60% was taken into account, and the permeability $P_{GFRE,\,60\%}$ was determined as $1.14 \cdot 10^{-10}$ mol/(m.s.MPa).

As the thickness of the inner pipe wall increases, the permeation flow decreases and asymptotically tends to zero for infinite thicknesses. For both the 50% H_2 and 80% H_2 cases, the curve reaches an approximate plateau at a thickness of 10 mm (see Figure 7.17). Therefore, there would be no significant benefits in further increasing the wall thickness of the pipe in terms of permeation. However, greater thickness might be needed due to mechanical requirements, which are not taken into account when considering the ratio between the two tube diameters as optimal. This is because it assumes that the pressure difference between the two sides of the GFRE pipe is zero.

Scenario A **Scenario B**

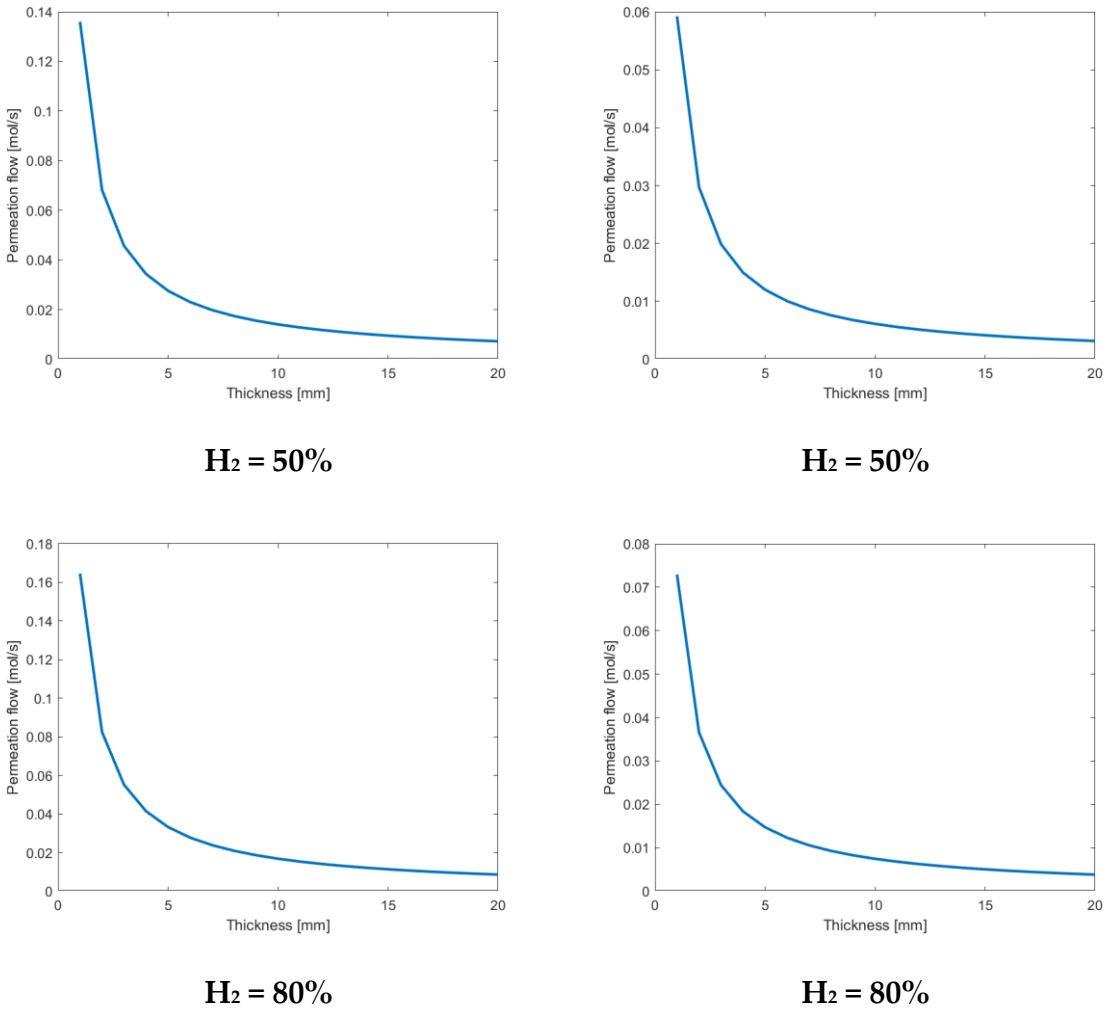

Figure 7.17 - H_2 permeation flow as a function of wall thickness for scenarios A and B

The molar flow of hydrogen permeating across the entire tube length is greater in 80% H_2 case than in 50% case, more precisely 1.2 times, as shown in Table 7.26. This difference between the two cases is the result of a different pipe length, which is longer for 50% H_2, and a different diameter of the inner tube, which is larger for 80% H_2 (see Table 7.22). This value can also be converted into terms of volume or energy.

Table 7.26 - Molar, volumetric and energy permeation flow for scenarios A and B

Scenario	Thickness [mm]	% H_2	Molar flow [mol/s]	Volume flow [m^3/s]	Energy flow [MW]
A	10	50%	0.0140	$5.0064 \cdot 10^{-6}$	0.0036
		80%	0.0169	$6.0142 \cdot 10^{-6}$	0.0044
B	10	50%	0.0061	$3.0164 \cdot 10^{-6}$	0.0015
		80%	0.0075	$3.6871 \cdot 10^{-6}$	0.0018

With a certain flow of hydrogen passing through the FRP tube and ending up in the annular section where natural gas flows, the contamination of the natural gas has been analysed. The downstream influence of the permeated hydrogen flow along the entire tube length on the natural gas flow rate has been considered and the values are contained in Table 7.27.

Table 7.27 - NG contamination by permeated H_2 in the annulus for scenarios A and B

Scenario	% H_2	$\dot{n}_{H2,perm}$ [mol/s]	$\dot{n}_{NG}$ [mol/s]	$ppm_{H2,out}$
A	**50%**	0.0140	$1.4439 \cdot 10^{4}$	0.970
	80%	0.0169	$7.8905 \cdot 10^{3}$	2.142
B	**50%**	0.0061	$1.4776 \cdot 10^{4}$	0.413
	80%	0.0075	$8.0784 \cdot 10^{3}$	0.928

In the 80% H_2 case, the hydrogen fraction inside natural gas is about 2.2 times larger compared to the 50% H_2 case in both scenarios A and B. However, in any scenario, the amount of hydrogen that ends up in the natural gas is still negligible, with the hydrogen fraction being on the order of 1-2 ppm in scenario A and 0.5-1 ppm in scenario B. As a result, the quality of the natural gas remains practically unchanged.

8 Conclusions

This thesis addressed the topic of hydrogen transportation through pipelines, focusing on the possibility of retrofitting the existing transportation infrastructure, with a particular emphasis on the pipe-in-pipe solution. An experimental analysis has been conducted to characterize fibre-reinforced polymers (FRP), which have been identified as promising materials in the context of hydrogen transport. Specifically, the roughness and hydrogen permeability have been assessed. Relying on the retrieved experimental data, the fluid dynamics behaviour of the pipe-in-pipe system has been investigated, taking the hydrogen-natural gas blend transportation case as a reference, as this option is commonly considered when contemplating pipeline retrofitting.

The experimental analysis on FRP involved three types of materials: carbon fibre-reinforced epoxy resin (CFRE), glass fibre-reinforced epoxy resin (GFRE), and glass fibre-reinforced polypropylene (GFRPP).

Surface roughness tests were conducted on specimens obtained from tubes previously manufactured using the mentioned materials through the multi-filament winding (MFW) technique. These tests aimed to characterize both the inner and outer surfaces of the samples, since in the pipe-in-pipe system these materials are considered for the inner tube, which is exposed to gas flow on both sides. Measurements were carried out using a digital microscope, which employs the "depth from focus" (DFF) method to generate a three-dimensional map of a specific area. Line profile measurements were then performed on this map in the circumferential and longitudinal directions, and the assessed length is 2 mm for each line. Among all roughness parameters, the arithmetic mean roughness was of primary interest. The values for the internal surface are 0.359 μm, 0.638 μm and 0.606 μm for CFRE, GFRE and GFRPP, respectively, while for the external surface they are 0.447 μm, 1.757 μm and 0.628 μm. Despite differences in calculated values, it was found that these discrepancies did not result in significant changes in the fluid dynamics of the pipe-in-pipe system, but still fibre-reinforced polymers show roughness values that are way lower than those typical of steel.

Permeation tests principles were mainly based on the electrochemical method established by the ISO 17081 standard, which pertains to metallic materials. Therefore, several adaptations were necessary to apply the same principle to composite polymer materials. The equipment utilized for these tests include the Automated Measurement and Control Box (AMB) from iChemAnalytics GmbH and the ElyFlow test cell from

Gaskatel, whose cost is lower compared to the apparatus for the manometric method, in addition to being safer in its application. Samples made of carbon fibre-reinforced epoxy resin (CFRE) and glass fibre-reinforced epoxy resin (GFRE) were produced for the permeation tests, composed of both 6 and 9 layers of fibres. They were cut out from FRP plates obtained from prepregs using a waterjet machine, surface-polished, and then coated with a thin layer of palladium using sputtering. It is precisely this coating that holds the key to the potential extension of the electrochemical method to non-conductive materials, as in this case. The permeated hydrogen is determined by measuring the current generated by the oxidation of hydrogen atoms at the palladium coating. This current is correlated with the flow of hydrogen atoms, which are electrolytically produced in a loading cell, passing through the sample. However, the obtained results were not satisfactory and, indeed, incorrect. Consequently, for the subsequent permeation analysis, developed for the pipe-in-pipe model, values derived from literature experimental data were employed instead. A hydrogen permeability of $1.14 \cdot 10^{-10}$ mol/(m.s.MPa) has been obtained for GFRE with a fibre volume fraction of 60%.

The fluid dynamic analysis was performed developing a steady-state, 1D, finite volume numerical model, which also accounts for the non-ideal behaviour of the transported gas. Thermo-physical properties were calculated using REFPROP, while the friction factor for pressure losses was determined using the explicit Hofer formulation of the Colebrook-White equation.

The analysis focused on the transmission level, as it presents the most critical conditions in terms of mechanical stress and potential issues related to hydrogen contact (hydrogen embrittlement for steels), and the boundary conditions were selected accordingly. Specifically, a diameter of 0.7 m was considered, corresponding to a typical value for transmission pipelines. Two scenarios were analysed, differing in operational pressure values: for “scenario A”, simulating the typical conditions of national transmission grid, initial and final pressures (at which the gas will need to be recompressed) were chosen as 70 bar and 50 bar, respectively. On the other hand, for “scenario B”, representative of the regional grid, these values are lower and become 50 bar and 30 bar, respectively.

The numerical analysis initially centred around the transportation of hydrogen blended with natural gas, representing commonly considered option for hydrogen transport based on the retrofit of the existing infrastructure. The percentages considered are 0%, 2%, 5%, 10%, 20%, 50%, 80%, 90%, and 100%. Lower values are representative of the current hydrogen fraction limits in various countries, while higher values are of interest for future developments of the infrastructure.

First, the case called “Constant energy” was studied, which aims to deliver the same amount of energy as pure natural gas via blends. The volume flow rate of blends is

higher than with natural gas, and pressure drops are also higher. These reach a maximum for hydrogen fractions close to 80%. Comparing the effect at the level of the national network with the regional network, the distances at which compressor stations must be placed are reduced by one-third in the latter case: for example, for an H_2 fraction of 50%, they are 700 km and 460 km respectively.

The second case analysed was named "Retrofit" and considered values of the distance between compressor stations and the pressures at the inlet and outlet of the compressor equal to those of pure natural gas transport. Consequently, the pressure profiles along the pipeline are set to be the same, with a pipeline length of 1060 km in scenario A and 680 km in scenario B. With blends, a larger volume of gas is transported but less energy, which reaches a minimum for a hydrogen fraction close to 80%. As far as the regional network retrofit is concerned, it leads to higher values than the national network, both in terms of volume and energy flow rate.

The study then shifted to the pipe-in-pipe system and its performance within the aforementioned context. The investigated configuration adopted FRP as material for the inner pipe, which is in contact with hydrogen. Hydrogen percentages relative to the total transported gas that were considered are 50% and 80%, chosen to have significant quantities of hydrogen transported that justify the utilization of this solution, and the total flow rate of the system was taken equal to the "Retrofit" case seen for the blend.

The analysis began by examining the effect of the ratio between the diameters of the inner and outer pipes on pressure behaviour. The aim was to identify the value of this ratio at which the pressures of the two gases on the two sides of the inner pipe are equal. This condition was evaluated as the "optimum", as it limits issues related to mechanical stress and strikes a balance between the distances at which hydrogen and natural gas reach the minimum pressure. Next, the required power to compress the two gases separately and the total power consumed, which is the sum of the two previous values, were calculated. This value was then compared with the energy flow rate being transported to assess its significance in the overall analysis. Finally, a study of hydrogen permeation through the FRP pipe, specifically glass fibre-reinforced epoxy (GFRE), was conducted. Permeability values were determined starting from literature data, and a fibre volume fraction of 60% in the composite was assumed, referring to commercially available products.

Several concluding considerations have emerged from this analysis.

The diameter ratio affects the pressure behaviour of hydrogen and natural gas differently: going from ¼ to ¾, the distance at which the minimum pressure is reached increases by about 200 times for H_2 and decreases by about 270 times for NG. The value of the "optimum" ratio corresponds to 0.4 for the case of 50% H_2 and 0.53 for 80% H_2, and it can be used to compress the gases at the same distance: the national network

requires a compressor station after more than 200 km, while the regional network requires one after approximately 120 km. However, these values are about one-fifth of those obtained for the "Retrofit" case seen for the blend transport, which is 1060 km and 680 km, respectively, leading to increased CAPEX. OPEX for compression is not significantly affected: compressing the blend requires less power compared to compressing the two gases separately with the same hydrogen fraction but, in any case, in both scenarios these values represent a small fraction of the energy flow rate.

GFRE was chosen as the material for the inner pipe due to its better barrier properties according to scientific literature compared to CFRE, despite the latter demonstrating lower roughness since it was observed that this difference has negligible consequences on fluid dynamics. This choice is also justified from an economic perspective, as the cost of glass fibres is lower than that of carbon fibres but could be reversed if mechanical properties were taken into consideration, as CFRP offer better mechanical performance compared to GFRP. However, it is relevant to note that FRP pipes are two orders of magnitude smoother than metallic ones. For wall thicknesses exceeding 10 mm, there are no advantages in terms of hydrogen permeation, and this would entail higher production costs and a greater weight of the component, along with all the associated consequences. This value is sufficient to ensure that the quality of natural gas remains largely unaffected, as the final hydrogen concentration in the annulus is in the order of ppm.

Future developments should be considered for a better understanding and implementation of hydrogen transport by pipe-in-pipe system, based on the limitations and simplifications of this work. Among these:

- Carry out permeation tests that allow for accurate experimental results in a simple and cost-effective manner. Further investigations can be conducted on the electrochemical method, but an alternative idea could be to load the sample with gaseous hydrogen (typical of the manometric method) while maintaining the same measurement principle as the electrochemical method, based on current. This way, there would be no need to coat the loading surface with palladium, and hydrogen would permeate in molecular form.
- Evaluate the mechanical requirements of the pipe-in-pipe system, mainly related to the effects of pressure fluctuations on the inner pipe, as the outer pipe has already been studied to withstand the considered pressures.
- Consider the influence of the pipe-in-pipe system configuration, whether concentric or eccentric, on the fluid dynamics of the gas inside.

Bibliography

[1] "Global Energy Crisis – Topics - IEA." https://www.iea.org/topics/global-energy-crisis (accessed Aug. 05, 2023).

[2] "A European Green Deal." https://commission.europa.eu/strategy-and-policy/priorities-2019-2024/european-green-deal_en (accessed Aug. 05, 2023).

[3] "Piano Nazionale di Ripresa e Resilienza (PNRR)."

[4] I. - International Energy Agency, "Global Hydrogen Review 2021," Accessed: Sep. 03, 2023. [Online]. Available: www.iea.org/t&c/.

[5] "Hydrogen - IEA." https://www.iea.org/energy-system/low-emission-fuels/hydrogen (accessed Aug. 05, 2023).

[6] "Hydrogen." https://energy.ec.europa.eu/topics/energy-systems-integration/hydrogen_en (accessed Aug. 08, 2023).

[7] "Communication COM/2020/301: A hydrogen strategy for a climate-neutral Europe | Knowledge for policy." https://knowledge4policy.ec.europa.eu/publication/communication-com2020301-hydrogen-strategy-climate-neutral-europe_en (accessed Aug. 08, 2023).

[8] "Executive summary – Global Hydrogen Review 2022 – Analysis - IEA." https://www.iea.org/reports/global-hydrogen-review-2022/executive-summary (accessed Aug. 02, 2023).

[9] F. Parolin, P. Colbertaldo, and S. Campanari, "Development of a multi-modality hydrogen delivery infrastructure: An optimization model for design and operation," *Energy Convers. Manag.*, vol. 266, p. 115650, Aug. 2022, doi: 10.1016/J.ENCONMAN.2022.115650.

[10] IEA, "The Future of Hydrogen - Seizing today's opportunities," 2019.

[11] A. Léon, Ed., *Hydrogen Technology: Mobile and Portable Applications*. Berlin, Heidelberg: Springer, 2008.

[12] J. Alazemi and J. Andrews, "Automotive hydrogen fuelling stations: An international review," *Renew. Sustain. Energy Rev.*, vol. 48, pp. 483–499, Aug. 2015, doi: 10.1016/J.RSER.2015.03.085.

[13] G. Kakoulaki, I. Kougias, N. Taylor, F. Dolci, J. Moya, and A. Jäger-Waldau, "Green hydrogen in Europe – A regional assessment: Substituting existing

production with electrolysis powered by renewables," *Energy Convers. Manag.*, vol. 228, p. 113649, Jan. 2021, doi: 10.1016/J.ENCONMAN.2020.113649.

[14] F. Moreno-Brieva, J. Guimón, and J. C. Salazar-Elena, "From grey to green and from west to east: The geography and innovation trajectories of hydrogen fuel technologies," *Energy Res. Soc. Sci.*, vol. 101, p. 103146, Jul. 2023, doi: 10.1016/J.ERSS.2023.103146.

[15] J. Incer-Valverde, A. Korayem, G. Tsatsaronis, and T. Morosuk, "'Colors' of hydrogen: Definitions and carbon intensity," *Energy Convers. Manag.*, vol. 291, p. 117294, Sep. 2023, doi: 10.1016/J.ENCONMAN.2023.117294.

[16] J. Chi and H. Yu, "Water electrolysis based on renewable energy for hydrogen production," *Chinese J. Catal.*, vol. 39, no. 3, pp. 390–394, Mar. 2018, doi: 10.1016/S1872-2067(17)62949-8.

[17] S. Shiva Kumar and H. Lim, "An overview of water electrolysis technologies for green hydrogen production," *Energy Reports*, vol. 8, pp. 13793–13813, Nov. 2022, doi: 10.1016/J.EGYR.2022.10.127.

[18] A. Jäger-Waldau, I. Kougias, N. Taylor, and C. Thiel, "How photovoltaics can contribute to GHG emission reductions of 55% in the EU by 2030," *Renew. Sustain. Energy Rev.*, vol. 126, p. 109836, Jul. 2020, doi: 10.1016/J.RSER.2020.109836.

[19] M. J. Chae, J. H. Kim, B. Moon, S. Park, and Y. S. Lee, "The present condition and outlook for hydrogen-natural gas blending technology," *Korean J. Chem. Eng.*, vol. 39, no. 2, pp. 251–262, Feb. 2022, doi: 10.1007/S11814-021-0960-8/METRICS.

[20] X. Wu, H. Zhang, M. Yang, W. Jia, Y. Qiu, and L. Lan, "From the perspective of new technology of blending hydrogen into natural gas pipelines transmission: Mechanism, experimental study, and suggestions for further work of hydrogen embrittlement in high-strength pipeline steels," *Int. J. Hydrogen Energy*, vol. 47, no. 12, pp. 8071–8090, Feb. 2022, doi: 10.1016/J.IJHYDENE.2021.12.108.

[21] B. C. Erdener *et al.*, "A review of technical and regulatory limits for hydrogen blending in natural gas pipelines," *Int. J. Hydrogen Energy*, vol. 48, no. 14, pp. 5595–5617, Feb. 2023, doi: 10.1016/J.IJHYDENE.2022.10.254.

[22] H. Wang *et al.*, "Research and demonstration on hydrogen compatibility of pipelines: a review of current status and challenges," *Int. J. Hydrogen Energy*, vol. 47, no. 66, pp. 28585–28604, Aug. 2022, doi: 10.1016/J.IJHYDENE.2022.06.158.

[23] C. Kim, S. H. Cho, S. M. Cho, Y. Na, S. Kim, and D. K. Kim, "Review of hydrogen infrastructure: The current status and roll-out strategy," *Int. J. Hydrogen Energy*, vol. 48, no. 5, pp. 1701–1716, Jan. 2023, doi: 10.1016/J.IJHYDENE.2022.10.053.

[24] Intralink, "The Hydrogen Economy South Korea Market Intelligence Report," 2021.

[25] "II. On some remarkable changes produced in iron and steel by the action of hydrogen and acids," *Proc. R. Soc. London*, vol. 23, no. 156–163, pp. 168–179, Dec. 1875, doi: 10.1098/RSPL.1874.0024.

[26] A. Suzuki and H. Yukawa, "A Review for Consistent Analysis of Hydrogen Permeability through Dense Metallic Membranes," *Membranes (Basel).*, vol. 10, no. 6, pp. 1–22, Jun. 2020, doi: 10.3390/MEMBRANES10060120.

[27] EIGA, "HYDROGEN PIPELINE SYSTEMS," 2014.

[28] K. Topolski *et al.*, "Hydrogen Blending into Natural Gas Pipeline Infrastructure: Review of the State of Technology." NREL, 2022.

[29] S. K. Dwivedi and M. Vishwakarma, "Hydrogen embrittlement in different materials: A review," *Int. J. Hydrogen Energy*, vol. 43, no. 46, pp. 21603–21616, Nov. 2018, doi: 10.1016/J.IJHYDENE.2018.09.201.

[30] A. Laureys, R. Depraetere, M. Cauwels, T. Depover, S. Hertelé, and K. Verbeken, "Use of existing steel pipeline infrastructure for gaseous hydrogen storage and transport: A review of factors affecting hydrogen induced degradation," *J. Nat. Gas Sci. Eng.*, vol. 101, p. 104534, May 2022, doi: 10.1016/J.JNGSE.2022.104534.

[31] N. E. Nanninga, Y. S. Levy, E. S. Drexler, R. T. Condon, A. E. Stevenson, and A. J. Slifka, "Comparison of hydrogen embrittlement in three pipeline steels in high pressure gaseous hydrogen environments," *Corros. Sci.*, vol. 59, pp. 1–9, Jun. 2012, doi: 10.1016/J.CORSCI.2012.01.028.

[32] G. Pluvinage, J. Capelle, and M. H. Meliani, "Pipe networks transporting hydrogen pure or blended with natural gas, design and maintenance," *Eng. Fail. Anal.*, vol. 106, p. 104164, Dec. 2019, doi: 10.1016/J.ENGFAILANAL.2019.104164.

[33] "What's Your Purpose? Reusing Gas Infrastructure for Hydrogen Transportation - World-Energy." https://www.world-energy.org/article/13793.html (accessed Jul. 26, 2023).

[34] M. W. Melaina, O. Antonia, and M. Penev, "Blending Hydrogen into Natural Gas Pipeline Networks: A Review of Key Issues." NREL, 2013.

[35] A. Gulienetti, "Towards hydrogen transportation in gas transmission pipelines," Politecnico di Milano.

[36] Snam, "Piano decennale di sviluppo della rete di trasporto di gas naturale 2021-2030." https://www.snam.it/export/sites/snam-rp/repository-srg/file/it/business-servizi/Processi_Online/Allacciamenti/informazioni/piano-decennale/pd_2021_2030/consultazione/SRG_Piano_Decennale_2021-2030_final.pdf (accessed Jul. 26, 2023).

[37] Snam, "Codice di rete." https://www.snam.it/it/i-nostri-business/trasporto/codice-di-rete-tariffe-area-comitato-e-consultazioni/codice-

di-rete.html (accessed Jul. 26, 2023).

[38] K. L. Simmons *et al.*, "H-Mat hydrogen compatibility of polymers and elastomers," *Int. J. Hydrogen Energy*, vol. 46, no. 23, pp. 12300–12310, Mar. 2021, doi: 10.1016/J.IJHYDENE.2020.06.218.

[39] R. R. Barth, K. L. Simmons, and C. San Marchi, "Polymers for Hydrogen Infrastructure and Vehicle Fuel Systems: Applications, Properties, and Gap Analysis." [Online]. Available: https://www.osti.gov/servlets/purl/1104755.

[40] S. Castagnet, J. C. Grandidier, M. Comyn, and G. Benoît, "Effect of long-term hydrogen exposure on the mechanical properties of polymers used for pipes and tested in pressurized hydrogen," *Int. J. Press. Vessel. Pip.*, vol. 89, pp. 203–209, Jan. 2012, doi: 10.1016/J.IJPVP.2011.11.008.

[41] H. Iskov, "Field test of hydrogen in the natural gas grid." DGC, 2010.

[42] I. A. Gondal and M. H. Sahir, "Prospects of natural gas pipeline infrastructure in hydrogen transportation," *Int. J. Energy Res.*, vol. 36, no. 15, pp. 1338–1345, Dec. 2012, doi: 10.1002/ER.1915.

[43] F. Dolci *et al.*, "Incentives and legal barriers for power-to-hydrogen pathways: An international snapshot," *Int. J. Hydrogen Energy*, vol. 44, no. 23, pp. 11394–11401, May 2019, doi: 10.1016/J.IJHYDENE.2019.03.045.

[44] D. Haeseldonckx and W. D'haeseleer, "The use of the natural-gas pipeline infrastructure for hydrogen transport in a changing market structure," *Int. J. Hydrogen Energy*, vol. 32, no. 10–11, pp. 1381–1386, Jul. 2007, doi: 10.1016/J.IJHYDENE.2006.10.018.

[45] "Preparing for the hydrogen economy by using the existing natural gas system as a catalyst (NATURALHY) | NATURALHY | Project | Fact sheet | FP6 | CORDIS | European Commission." https://cordis.europa.eu/project/id/502661 (accessed Aug. 08, 2023).

[46] J. Ogden, A. M. Jaffe, D. Scheitrum, Z. McDonald, and M. Miller, "Natural gas as a bridge to hydrogen transportation fuel: Insights from the literature," *Energy Policy*, vol. 115, pp. 317–329, Apr. 2018, doi: 10.1016/J.ENPOL.2017.12.049.

[47] D. Mahajan, K. Tan, T. Venkatesh, P. Kileti, and C. R. Clayton, "Hydrogen Blending in Gas Pipeline Networks—A Review," *Energies 2022, Vol. 15, Page 3582*, vol. 15, no. 10, p. 3582, May 2022, doi: 10.3390/EN15103582.

[48] "Snam: Europe's first supply of hydrogen and natural gas blend into transmission network to industrial users." https://www.snam.it/en/media/news-and-press-releases/comunicati-stampa/2019/snam-europe-s-first-supply-of-hydrogen-and-natural-gas-blend-into-transmission-network-to-industrial-users.html (accessed Jul. 26, 2023).

[49] "Snam, RINA and the GIVA Group: the world's first test with a 30% natural gas/hydrogen blend in steel forging." .

[50] "HyBRIDS Project | Società Gasdotti Italia." https://www.gasdottitalia.it/en/content/hybrids-project (accessed Aug. 08, 2023).

[51] "Hydrogen is vital to tackling climate change - HyDeploy." https://hydeploy.co.uk/ (accessed Aug. 08, 2023).

[52] "The GRHYD demonstration project | Gas | ENGIE." https://www.engie.com/en/businesses/gas/hydrogen/power-to-gas/the-grhyd-demonstration-project (accessed Aug. 08, 2023).

[53] "HyBlend Project To Accelerate Potential for Blending Hydrogen in Natural Gas Pipelines | News | NREL." https://www.nrel.gov/news/program/2020/hyblend-project-to-accelerate-potential-for-blending-hydrogen-in-natural-gas-pipelines.html (accessed Aug. 08, 2023).

[54] "H2 Blending | SoCalGas." https://www.socalgas.com/sustainability/hydrogen/h2-blending (accessed Aug. 08, 2023).

[55] Y. Deng *et al.*, "Hydrogen-enriched natural gas in a decarbonization perspective," *Fuel*, vol. 318, p. 123680, Jun. 2022, doi: 10.1016/J.FUEL.2022.123680.

[56] C. Sheng and J. L. T. Azevedo, "Estimating the higher heating value of biomass fuels from basic analysis data," *Biomass and Bioenergy*, vol. 28, no. 5, pp. 499–507, May 2005, doi: 10.1016/J.BIOMBIOE.2004.11.008.

[57] J. Leicher *et al.*, "The Impact of Hydrogen Admixture into Natural Gas on Residential and Commercial Gas Appliances," *Energies 2022, Vol. 15, Page 777*, vol. 15, no. 3, p. 777, Jan. 2022, doi: 10.3390/EN15030777.

[58] I. Burgers, L. Dehdari, P. Xiao, K. G. Li, E. Goetheer, and P. Webley, "Techno-economic analysis of PSA separation for hydrogen/natural gas mixtures at hydrogen refuelling stations," *Int. J. Hydrogen Energy*, vol. 47, no. 85, pp. 36163–36174, Oct. 2022, doi: 10.1016/J.IJHYDENE.2022.08.175.

[59] M. Luberti and H. Ahn, "Review of Polybed pressure swing adsorption for hydrogen purification," *Int. J. Hydrogen Energy*, vol. 47, no. 20, pp. 10911–10933, Mar. 2022, doi: 10.1016/J.IJHYDENE.2022.01.147.

[60] S. Sircar and T. C. Golden, "Purification of Hydrogen by Pressure Swing Adsorption," *http://dx.doi.org/10.1081/SS-100100183*, vol. 35, no. 5, pp. 667–687, 2006, doi: 10.1081/SS-100100183.

[61] M. Aasadnia, M. Mehrpooya, and B. Ghorbani, "A novel integrated structure for

hydrogen purification using the cryogenic method," *J. Clean. Prod.*, vol. 278, p. 123872, Jan. 2021, doi: 10.1016/J.JCLEPRO.2020.123872.

[62] N. W. Ockwig and T. M. Nenoff, "Membranes for hydrogen separation," *Chem. Rev.*, vol. 107, no. 10, pp. 4078–4110, Oct. 2007, doi: 10.1021/CR0501792/ASSET/IMAGES/MEDIUM/CR0501792E00011.GIF.

[63] W. Liemberger, M. Groß, M. Miltner, and M. Harasek, "Experimental analysis of membrane and pressure swing adsorption (PSA) for the hydrogen separation from natural gas," *J. Clean. Prod.*, vol. 167, pp. 896–907, Nov. 2017, doi: 10.1016/J.JCLEPRO.2017.08.012.

[64] M. Takht Ravanchi, T. Kaghazchi, and A. Kargari, "Application of membrane separation processes in petrochemical industry: a review," *Desalination*, vol. 235, no. 1–3, pp. 199–244, Jan. 2009, doi: 10.1016/J.DESAL.2007.10.042.

[65] H. T. Lu, W. Li, E. S. Miandoab, S. Kanehashi, and G. Hu, "The opportunity of membrane technology for hydrogen purification in the power to hydrogen (P2H) roadmap: a review," *Front. Chem. Sci. Eng.*, vol. 15, no. 3, pp. 464–482, Jun. 2021, doi: 10.1007/S11705-020-1983-0/METRICS.

[66] S. Adhikari and S. Fernando, "Hydrogen membrane separation techniques," *Ind. Eng. Chem. Res.*, vol. 45, no. 3, pp. 875–881, Feb. 2006, doi: 10.1021/IE050644L/ASSET/IMAGES/LARGE/IE050644LF00001.JPEG.

[67] J. Allden, "Hydrogen Deblending: Future and Emerging Technology Watch." NPL, 2022, doi: 10.47120/npl.ENV45.

[68] "SEPURAN® Noble I Membranes for efficient hydrogen recovery - Evonik Industries." https://www.membrane-separation.com/en/hydrogen/recovery-with-sepuran-noble (accessed Jul. 29, 2023).

[69] A. F. O., A. P. O., and O. O. O., "Mechanical Properties of a Polyester Fibre Glass Composite," *Int. J. Compos. Mater.*, vol. 2, no. 6, pp. 147–151, Jan. 2013, doi: 10.5923/J.CMATERIALS.20120206.06.

[70] D. K. Rajak, D. D. Pagar, R. Kumar, and C. I. Pruncu, "Recent progress of reinforcement materials: a comprehensive overview of composite materials," *J. Mater. Res. Technol.*, vol. 8, no. 6, pp. 6354–6374, Nov. 2019, doi: 10.1016/J.JMRT.2019.09.068.

[71] M. Z. Naser, R. A. Hawileh, and J. A. Abdalla, "Fiber-reinforced polymer composites in strengthening reinforced concrete structures: A critical review," *Eng. Struct.*, vol. 198, p. 109542, Nov. 2019, doi: 10.1016/J.ENGSTRUCT.2019.109542.

[72] M. A. Masuelli, "Introduction of Fibre-Reinforced Polymers − Polymers and Composites: Concepts, Properties and Processes," *Fiber Reinf. Polym. - Technol. Appl. Concr. Repair*, Jan. 2013, doi: 10.5772/54629.

[73] S. Erden, K. Sever, Y. Seki, and M. Sarikanat, "Enhancement of the mechanical properties of glass/polyester composites via matrix modification glass/polyester composite siloxane matrix modification," *Fibers Polym.*, vol. 11, no. 5, pp. 732–737, Sep. 2010, doi: 10.1007/S12221-010-0732-2/METRICS.

[74] F. Zejnullahu, J. Wilke, and P. Nicolaou, "Development of Composite Tubes for Rocketry Applications by Analyzing Cost-Effective and Adjustable Manufacturing Processes," RWTH Aachen University, 2022.

[75] W. Albrecht, H. Fuchs, and W. Kittelmann, Eds., *Nonwoven Fabrics: Raw Materials, Manufacture, Applications, Characteristics, Testing Processes*, 1st ed. Wiley-VCH.

[76] R. M. N. Sulochani, R. A. Jayasinghe, A. H. L. R. Nilmini, and G. Priyadarshana, "Recent Developments in Textile Reinforced Polymer Composites," *Asian J. Chem.*, vol. 34, no. 3, pp. 487–496, Mar. 2022, doi: 10.14233/AJCHEM.2022.23504.

[77] A. C. Corbin *et al.*, "Towards hemp fabrics for high-performance composites: Influence of weave pattern and features," *Compos. Part B Eng.*, vol. 181, Jan. 2020, doi: 10.1016/J.COMPOSITESB.2019.107582.

[78] K. Vallons, "The Behaviour of Carbon Fibre - Epoxy NCF Composites under Various Mechanical Loading Conditions," KU Leuven, 2009.

[79] J. Qureshi, "A Review of Fibre Reinforced Polymer Structures," *Fibers 2022, Vol. 10, Page 27*, vol. 10, no. 3, p. 27, Mar. 2022, doi: 10.3390/FIB10030027.

[80] "New Structural Materials Technologies: Opportunities for the Use of Advanced Ceramics and Composites," Washington, DC: U.S. Congress, Office of Technology Assessment, 1986.

[81] S. Prashanth, S. Km, Nithin K, and Sachhidananda S, "Fiber Reinforced Composites -A Review," *J Mater. Sci Eng*, vol. 6, p. 341, 2017, doi: 10.4172/2169-0022.1000341.

[82] A. R. Bunsell, "High-performance Fibers," *Encycl. Mater. Sci. Technol.*, pp. 1–10, Jan. 2005, doi: 10.1016/B0-08-043152-6/02100-8.

[83] A. Carolin, "Carbon Fibre Reinforced Polymers for Strengthening of Structural Elements," Lulea University of Technology, 2003.

[84] X. Huang, "Fabrication and Properties of Carbon Fibers," *Mater. 2009, Vol. 2, Pages 2369-2403*, vol. 2, no. 4, pp. 2369–2403, Dec. 2009, doi: 10.3390/MA2042369.

[85] H. Ku, H. Wang, N. Pattarachaiyakoop, and M. Trada, "A review on the tensile properties of natural fiber reinforced polymer composites," *Compos. Part B Eng.*, vol. 42, no. 4, pp. 856–873, Jun. 2011, doi: 10.1016/J.COMPOSITESB.2011.01.010.

[86] "Filament winding, reinvented | CompositesWorld." https://www.compositesworld.com/articles/filament-winding-reinvented

(accessed Aug. 12, 2023).

[87] "International Cooperation on Innovative Winding Technique - RWTH AACHEN UNIVERSITY ITA - English." https://www.ita.rwth-aachen.de/cms/ITA/Das-Institut/Aktuelle-Meldungen/~mzch/Innovative-Wickeltechnik-in-einer-intern/?lidx=1 (accessed Aug. 12, 2023).

[88] "Multiple Filament Winder | ADVANCED TECHNOLOGY | MURATEC, MURATA MACHINERY, LTD." https://www.muratec.net/at/filamentwinder.html (accessed Aug. 12, 2023).

[89] "ITA auf der JEC World 2016 in Paris - RWTH AACHEN UNIVERSITY ITA - Deutsch." https://www.ita.rwth-aachen.de/cms/ITA/Das-Institut/Aktuelle-Meldungen/~lxcl/ITA-auf-der-JEC-World-2016-in-Paris/ (accessed Aug. 12, 2023).

[90] B. Smith, C. Eberle, B. Frame, J. Blencoe, L. Anovitz, and J. Mays, "FRP Hydrogen Pipelines," 2008.

[91] J. G. Blencoe, S. L. Marshall, and M. T. Naney, "New, composite polymeric/metallic materials and designs for hydrogen pipelines."

[92] T. Rox, "Auslegung und theoretische Berechnung einer FVK-Pipeline für den Transport von Wasserstoff in Bezug auf dessen Permeationseigenschaften," RWTH Aachen University, 2022.

[93] G. Rawls, J. Ronevich, and A. Slifka, "Lowering Costs of Hydrogen Pipelines through Use of Fiber Reinforced Polymers and Modern Steels." 2017.

[94] G. Rawls and T. Adams, "Fiber Reinforced Composite Pipelines." SRNL, 2014.

[95] B. Smith, B. Frame, C. Eberle, L. Anovitz, and T. Armstrong, "Fiber Reinforced Polymer Pipelines for Hydrogen Delivery." 2007.

[96] *ISO 21920-2:2021 - Geometrical product specifications (GPS) — Surface texture: Profile — Part 2: Terms, definitions and surface texture parameters*. .

[97] E. S. Gadelmawla, M. M. Koura, T. M. A. Maksoud, I. M. Elewa, and H. H. Soliman, "Roughness parameters," *J. Mater. Process. Technol.*, vol. 123, no. 1, pp. 133–145, Apr. 2002, doi: 10.1016/S0924-0136(02)00060-2.

[98] "KEYENCE INTERNATIONAL (BELGIUM) NV/SA." https://www.keyence.eu/ (accessed Aug. 14, 2023).

[99] F. White, *Fluid Mechanics*, 4th ed. McGraw-Hill, 1999.

[100] Z. Zhan *et al.*, "Effect of the surface roughness of epoxy resin on its creeping flashover characteristics in C4F7N-CO2 gas mixtures," *AIP Adv.*, vol. 9, no. 4, p. 45129, Apr. 2019, doi: 10.1063/1.5095720/1076386.

[101] V. Siracusa, "Food packaging permeability behaviour: A report," *Int. J. Polym.*

Sci., vol. 2012, 2012, doi: 10.1155/2012/302029.

[102] A. Szczurek *et al.*, "Sol-gel multilayered coatings for reduction of H2 permeation," *Appl. Surf. Sci.*, vol. 497, p. 143691, Dec. 2019, doi: 10.1016/J.APSUSC.2019.143691.

[103] J. Humpenöder, "Gaspermeation von Faserverbunden mit Polymermatrices," Universität Karlsruhe (TH), 1997.

[104] David V. Ragone, *Termodinamica dei materiali, Volume 2*. Casa Editrice Ambrosiana, 2011.

[105] N. A. Al-Mufachi, N. V. Rees, and R. Steinberger-Wilkens, "Hydrogen selective membranes: A review of palladium-based dense metal membranes," *Renew. Sustain. Energy Rev.*, vol. 47, pp. 540–551, Jul. 2015, doi: 10.1016/J.RSER.2015.03.026.

[106] *ISO 15105-1:2007 - Plastics — Film and sheeting — Determination of gas-transmission rate — Part 1: Differential-pressure methods*. .

[107] *ISO 15105-2:2003 - Plastics — Film and sheeting — Determination of gas-transmission rate — Part 2: Equal-pressure method*. .

[108] *ISO 17081:2014 - Method of measurement of hydrogen permeation and determination of hydrogen uptake and transport in metals by an electrochemical technique*. .

[109] E. Van den Eeckhout, K. Verbeken, and T. Depover, "Methodology of the electrochemical hydrogen permeation test: A parametric evaluation," *Int. J. Hydrogen Energy*, vol. 48, no. 78, pp. 30585–30607, Sep. 2023, doi: 10.1016/J.IJHYDENE.2023.04.211.

[110] V. Lipp, R. Krauß, M. Dr Zöllinger, H.-J. Dr Kohnke, and J. U. Dr Riedel, "Verfahren und Vorrichtung zur elektrochemischen Messung von Wasserstoffpermeation," EP 3 553 210 A1, 2019.

[111] "iChemAnalytics GmbH." https://www.ichemanalytics.de/ (accessed Aug. 14, 2023).

[112] "Startseite - Gaskatel." https://gaskatel.de/ (accessed Aug. 14, 2023).

[113] "Diaphragm Pumps & Systems | KNF." https://knf.com/en/it (accessed Aug. 14, 2023).

[114] A. Zafra, Z. Harris, C. Sun, and E. Martínez-Pañeda, "Comparison of hydrogen diffusivities measured by electrochemical permeation and temperature-programmed desorption in cold-rolled pure iron," *J. Nat. Gas Sci. Eng.*, vol. 98, p. 104365, Feb. 2022, doi: 10.1016/J.JNGSE.2021.104365.

[115] H. Ooka, J. Huang, and K. S. Exner, "The Sabatier Principle in Electrocatalysis: Basics, Limitations, and Extensions," *Front. Energy Res.*, vol. 9, p. 654460, May 2021, doi: 10.3389/FENRG.2021.654460/BIBTEX.

[116] A. J. Medford *et al.*, "From the Sabatier principle to a predictive theory of transition-metal heterogeneous catalysis," *J. Catal.*, vol. 328, pp. 36–42, Aug. 2015, doi: 10.1016/J.JCAT.2014.12.033.

[117] A. R. Zeradjanin, J. P. Grote, G. Polymeros, and K. J. J. Mayrhofer, "A Critical Review on Hydrogen Evolution Electrocatalysis: Re-exploring the Volcano-relationship," *Electroanalysis*, vol. 28, no. 10, pp. 2256–2269, Oct. 2016, doi: 10.1002/ELAN.201600270.

[118] P. Quaino, F. Juarez, E. Santos, and W. Schmickler, "Volcano plots in hydrogen electrocatalysis-uses and abuses," *Beilstein J. Nanotechnol.*, vol. 5, no. 1, pp. 846–854, 2014, doi: 10.3762/BJNANO.5.96.

[119] J. Durst *et al.*, "Hydrogen Oxidation and Evolution Reaction (HOR/HER) on Pt Electrodes in Acid vs. Alkaline Electrolytes: Mechanism, Activity and Particle Size Effects," *ECS Trans.*, vol. 64, no. 3, pp. 1069–1080, Aug. 2014, doi: 10.1149/06403.1069ECST.

[120] B. D. Adams and A. Chen, "The role of palladium in a hydrogen economy," *Mater. Today*, vol. 14, no. 6, pp. 282–289, Jun. 2011, doi: 10.1016/S1369-7021(11)70143-2.

[121] M. Shao, "Palladium-based electrocatalysts for hydrogen oxidation and oxygen reduction reactions," *J. Power Sources*, vol. 196, no. 5, pp. 2433–2444, Mar. 2011, doi: 10.1016/J.JPOWSOUR.2010.10.093.

[122] "Maiko Fertigungstechnik." http://www.maiko-saegen.de/en/index-engl.htm (accessed Aug. 14, 2023).

[123] "ProtoMAX Abrasive Waterjet - OMAX Waterjet." https://www.omax.com/en/us/protomax-waterjet (accessed Aug. 14, 2023).

[124] "AutoMet 250, Membrane Keypad | Buehler." https://shop.buehler.com/automet-250-grinder-polisher (accessed Aug. 14, 2023).

[125] "Grain size table | Zische Schleifwerkzeuge GmbH." https://zische.de/en/grain-size-table/ (accessed Aug. 14, 2023).

[126] Marcel Pourbaix, *Atlas of Electrochemical Equilibria in Aqueous Solutions*, II. NACE, 1974.

[127] L. P. Bernini, "Dynamic operations of the gas distribution network: modelling decentralized biomethane injections," Politecnico di Milano.

[128] *ISO 12213-3:2006 - Natural gas — Calculation of compression factor — Part 3: Calculation using physical properties*. .

[129] K. Kazda and X. Li, "Approximating Nonlinear Relationships for Optimal Operation of Natural Gas Transport Networks," *Process. 2018, Vol. 6, Page 198*,

vol. 6, no. 10, p. 198, Oct. 2018, doi: 10.3390/PR6100198.

[130] "National Institute of Standards and Technology." https://www.nist.gov/ (accessed Aug. 22, 2023).

[131] N. Lamoureux and C. E. Paillard, "Natural gas ignition delay times behind reflected shock waves: Application to modelling and safety," *Shock Waves*, vol. 13, no. 1, pp. 57–68, Jul. 2003, doi: 10.1007/S00193-003-0188-Z/METRICS.

[132] *D. Interm. 16 aprile 2008, "Regola tecnica per la progettazione, costruzione, collaudo, esercizio e sorveglianza delle opere e dei sistemi di distribuzione e di linee dirette del gas naturale con densita'' non superiore a 0,8."* .

[133] G. Guandalini, P. Colbertaldo, and S. Campanari, "Dynamic modeling of natural gas quality within transport pipelines in presence of hydrogen injections," *Appl. Energy*, vol. 185, pp. 1712–1723, Jan. 2017, doi: 10.1016/J.APENERGY.2016.03.006.

List of Figures

List of Tables

List of symbols

Variable	Description	SI unit
T	Temperature	K
p	Pressure	Pa
T_0	Standard temperature	K
p_0	Standard pressure	Pa
ρ	Density	kg/m^3
μ	Dynamic viscosity	Pa.s
Z	Compressibility factor	-
MM	Molecular mass	kg/mol
P	Permeability	mol/(m.s.Pa)
T_r	Pseudo-critical reduced temperature	-
p_r	Pseudo-critical reduced pressure	-
HHV	Higher heating value	J/m^3
T_{pc}	Pseudo-critical temperature	K
p_{pc}	Pseudo-critical pressure	Pa
x_i	Molar fraction	%
u	Gas velocity	m/s
t	Time	s
R	Universal gas costant	J/(mol.K)
D	Diameter	m
ε	Roughness	m
Re	Reynolds number	-
f	Friction factor	-
F	Standard volumetric flow rate	Sm^3/h
$\dot{E}$	Energy flow rate	W
$\dot{n}$	Molar flow rate	mol/s
E	Energy	J
J	Flux	mol/(m^2.s)
I	Current	A
Q	Charge	C
p_{in}	Initial pressure	Pa
p_{fin}	Final pressure	Pa
L_{fin}	Compressor station distance	m

p_{inlet}	Inlet pressure at compressor station	Pa
p_{outlet}	Outlet pressure at compressor station	Pa
$P_{mecc,c}$	Mechanical compression power	W
A	Area	m^2
V	Volume	m^3
$\mathcal{P}$	Perimeter	m
$RMSE$	Root mean square error	-
f_v	Fibre volume fraction	%

List of acronyms

Acronym	Description
NG	Natural gas
FRP	Fibre-reinforced polymer
CFRE	Carbon fibre-reinforced epoxy resin
GFRE	Glass fibre-reinforced epoxy resin
GFRPP	Glass fibre-reinforced polypropylene
HE	Hydrogen embrittlement
MFW	Multi-filament winding
HOR	Hydrogen oxidation reaction
IQR	Interquartile range
GDE	Gas diffusion electrode
MOP	Maximum operating pressure
CAPEX	Capital expenditures
OPEX	Operational expenditures

Acknowledgements

Vorrei riservare queste prime righe ai Professori Giulio Guandalini e Paolo Colbertaldo per avermi dato la possibilità di svolgere questa tesi, che è stata un'occasione per me di approfondire i miei interessi e toccare con mano l'evidenza della sinergia che esiste e deve esistere tra i diversi settori, ingegneristici e non, e tra le persone. Vi sono grato soprattutto per aver dato spazio al mio spirito di iniziativa e alla mia voglia di mettermi in gioco. Grazie anche a Federico per gli utili consigli e per aver spesso ridimensionato le mie preoccupazioni, dimostrando sempre grande disponibilità nei miei confronti.

Un "vielen Dank" è dovuto anche al mio Tutor Niels Grigat, per avermi accolto all'istituto ITA della RWTH Aachen University al mio arrivo in Germania e per il prezioso aiuto nello svolgimento della parte sperimentale di questa tesi.

Ci tengo poi a fare un ringraziamento ai miei compagni di studio, con cui ho avuto il piacere di condividere lezioni, esami e non solo.

Questi anni sono stati per me molto intensi, dentro e fuori l'Ateneo, e l'impegno da parte mia è stato tanto. Dedico quindi queste ultime righe a tutti quelli che hanno anche solo provato a comprendere me e la ragione delle mie azioni, senza dover necessariamente condividere le mie scelte, in particolare ai miei fratelli, Marta e Giovanni, su cui so di poter sempre contare. Per me ha significato molto.